Alma Mater Studiorum – Università di Bologna

DOTTORATO DI RICERCA IN

SCIENZE DELLA TERRA

Ciclo XXVI

Settore Concorsuale di afferenza: 04/A1

Settore Scientifico disciplinare: GEO/06

NANOSCALE SURFACE PROPERTIES AND INTERACTION WITH
FUNDAMENTAL BIOMOLECULES OF CHLORITE AND PHLOGOPITE

Presentata da: **Daniele Moro**

Coordinatore Dottorato   **Relatore**

Prof. Vincenzo Picotti   **Prof. Giovanni Valdrè**

Esame finale anno 2014

TABLE OF CONTENTS

1. ABSTRACT

The surface properties of minerals have important implications in geology, environment, industry and biotechnology and for certain aspects in the research on the origin of life. In particular, the peculiar structure of phyllosilicates gives rise to specific physico-chemical surface properties that continuously attract the interest of scientists in basic, applicative and industrial research. This research project aims to widen the knowledge on the surface properties of selected phyllosilicates at the nano-scale. Here, I focused my research on chlorite and phlogopite surface properties investigated by advanced nanoscale methodologies, and then I investigated the interaction of fundamental biomolecules, such as nucleotides, RNA, DNA and amino acid glycine with the surface of the selected phyllosilicates.

Multiple advanced and complex experimental approaches based on scanning probe microscopy and spatially resolved spectroscopy were used and in some cases specifically developed to investigate the surface nanostructure, electric potential, surface modifications and the interaction with the above mentioned fundamental biomolecules.

The results demonstrate that chlorite exposes at the surface atomically flat terraces with 0.5 nm steps typically generated by the fragmentation of the octahedral sheet of the interlayer (brucitic-type). This fragmentation at the nanoscale generates a high anisotropy and inhomogeneity with surface type and isomorphous cationic substitutions determining variations of the effective surface potential difference, ranging between 50-100 mV and 400-500 mV, when measured in air, between the TOT surface and the interlayer brucitic sheet. The surface potential was ascribed to be the driving force of the observed high affinity of the surface with the fundamental biomolecules, like single molecules of nucleotides, DNA, RNA and amino acids. Single layer (brucitic-type) removal was demonstrated together with the design of specific substrates useful for bionanopatterning and biotech applications.

Phlogopite was also observed to present an extended atomically flat surface, featuring negative surface potential values of some hundreds of millivolts and no significant local variations. Single layer (i.e. TOT) removal was also demonstrated. Phlogopite surface was sometimes observed to present curvature features that may be ascribed to local substitutions of the interlayer cations or the presence of a crystal lattice mismatch or structural defects,

such as stacking faults or dislocation loops. Surface chemistry was found similar to the bulk. The study of the interaction with nucleotides and glycine revealed a lower affinity with respect to the brucite-like surface of chlorite.

The findings of this research can give a contribution for a better understanding of phyllosilicates behaviour in geological and industrial processes and to the development of the theories on prebiotic synthesis of biomolecules and the origin of life on earth.

2. RIASSUNTO

Le proprietà di superficie dei minerali hanno importanti ricadute nelle scienze geologiche e ambientali, nell'industria e nella biotecnologia, e per certi aspetti nelle ricerca sull'origine della vita. In particolare, la peculiare struttura dei fillosilicati genera specifiche proprietà fisico-chimiche di superficie che continuano ad attrarre l'interesse degli scienziati nel campo della ricerca di base, applicata ed industriale. Questo progetto di ricerca mira ad ampliare la conoscenza sulle proprietà di superficie alla nanoscala di particolari fillosilicati. In specifico, ho concentrato la mia ricerca sull'investigazione delle proprietà di superficie della clorite e della flogopite, utilizzando metodologie avanzate alla nanoscala, ed ho quindi studiato le interazioni di biomolecole fondamentali, come nucleotidi, RNA, DNA e l'amminoacido glicina, con la superficie dei fillosilicati selezionati.

Approcci sperimentali avanzati e complessi basati sulla microscopia a scansione di sonda e sulla spettroscopia spazialmente risolta sono stati utilizzati ed in alcuni casi specificamente sviluppati per investigare la nanostruttura di superficie, il potenziale elettrico, le modifiche della superficie e l'interazione con le biomolecole fondamentali sopra citate.

I risultati dimostrano che la clorite espone alla superficie terrazze atomicamente piane con gradini di 0.5 nm generati tipicamente dalla frammentazione del foglietto ottaedrico dell'interstrato (di tipo brucitico). Questa frammentazione alla nanoscala genera una forte anisotropia e disomogeneità dove il tipo di superficie e sostituzioni cationiche isomorfe determinano variazioni della differenza di potenziale efficace alla superficie. Quest'ultima varia tra 50-100 mV e 400-500 mV quando misurata in aria tra la superficie del TOT e quella del foglietto brucitico di interstrato. Il potenziale di superficie è stato considerato la forza guida dell'alta affinità della superficie con le biomolecole fondamentali, come singole molecole di nucleotidi, DNA, RNA e amminoacidi. È stata dimostrata la possibilità di rimuovere un singolo foglietto brucitico e la costruzione di specifici substrati utili per il bionanopatterning e applicazioni biotecnologiche.

Si è osservato che anche la flogopite presenta superfici estese atomicamente piane, con un potenziale di superficie negativo di alcune centinaia di millivolt e nessuna variazione locale significativa. È stata anche dimostrata la possibilità di rimuovere un singolo strato TOT.

Inoltre, sono state occasionalmente osservate caratteristiche curvature locali della superficie della flogopite che possono essere attribuite a sostituzioni dei cationi di interstrato o alla presenza di disadattamento del reticolo cristallino, o a difetti strutturali come difetti di impilamento o anelli di dislocazione. La chimica di superficie è stata trovata confrontabile con quella massiva. Gli studi di interazione con nucleotidi e glicina hanno rivelato una minore affinità rispetto alla superficie brucitica della clorite.

I risultati di questa ricerca possono contribuire a una migliore comprensione del ruolo dei fillosilicati nei processi geologici ed industriali e allo sviluppo delle teorie sulla sintesi prebiotica delle biomolecole e sull'origine della vita sulla terra.

3. INTRODUCTION

3.1. Research aims

This research project focuses on the investigation of chlorite and phlogopite surface properties down to the nanometre scale by exploiting advanced experimental approaches and, furthermore, to investigate the effect of the sub-nm physico-chemical properties of chlorite and phlogopite surfaces on the interaction with fundamental biomolecules. The affinity of both surfaces with single molecules of nucleotides and amino acids (glycine), and of chlorite with single molecules of RNA and DNA were compared.

Chlorite has a 2:1 layer structure (about 1 nm thick) plus an octahedral sheet in the interlayer (about 0.5 nm thick); phlogopite has a 2:1 layer structure (about 1 nm thick) with an interlayer cation.

Nowadays it is still not straightforward to address materials properties with nanometre scale resolution. A new field of investigation is rapidly grown in the last decades concerning advancement in materials knowledge and technology. In the context of this research, in order to access the nanoscale surface properties multiple spatially resolved approaches were exploited and in some cases developed, comprising atomic force microscopy, electric force microscopy, Kelvin probe force microscopy, nanolithography, micro-Raman spectroscopy and X-ray photoelectron spectroscopy.

Surface structure, surface sites (sites in the top molecular levels are often the critical ones in reaction or adsorption), adsorption, surface modification greatly affect the interaction of mineral particles with the surrounding environment.

The single molecule interaction of nucleotides and amino acids (glycine) with chlorite and phlogopite surfaces, and RNA and DNA with chlorite was here assessed.

It is also expected that the results of this research will help in addressing future researches on the subject in terms of methodological approach.

3.2. Outline of the research project

The physico-chemical surface properties of phyllosilicates and mineral oxides can drive mineral-environment surface interactions. A great variety of phenomena with important geological, environmental, (bio-)technological and economical spin-offs are influenced by the effects of the local surface properties, at the micro and nanometric scale.

Generally speaking, phyllosilicates have an extremely wide range of applications from ceramics, plastics, paints, paper, rubber, cosmetics and drugs to the potential applications as nanofillers in composite materials (Bergaya *et al.* 2006).

Mineral surface properties may control important interaction processes, such as coagulation, aggregation, sedimentation, filtration, catalysis, and ionic transport in porous media. Mineral floatability is strongly connected with particles surface charge, as well as mineral structure and composition. This charge can be permanent or constant, resulting, for instance, from isomorphous substitutions, or variable, due, for instance, to protonation and deprotonation of functional groups (Montes *et al.* 2007; Alvarez-Silva *et al.* 2010).

In addition, the electrical properties of mineral surfaces affect reactions with charged species such as metal ions, biomolecules and cells.

Mineral oxide particles have applications, for example, in many paint and paper formulations as pigments and fillers. Their stability is of importance for the processing properties and the quality of the final products, and the knowledge of the interactions between such particles is necessary to prevent them from flocculating or, at least, to control their flocculation.

Phyllosilicates typically present a characteristic surface nanomorphology. Processes of nucleation, growth and alteration of the nanostructures occur when minerals are exposed to humid air and the environment. Nanomorphology and nanostructures often have physico-chemical properties that are very different from those of the underlying mineral substrates. The overall effective reactivity can be greatly affected, regulating the rate of particle solubility as well as the surface sorption of inorganic and organic components. For instance, cell adhesion and subsequent biofilm formation can be directed by the nanostructure properties rather than by those of the primary particle (Kendall *et al.* 2008).

The structure and properties of water adsorbed onto clay surfaces are significantly influenced by the mineral surface. The differences in the structural charge, cation occupancies and distributions affect the dynamics and structure of surface water.

In geochemistry and environmental science, water–mineral interactions are important factors controlling processes such as surface ion adsorption and ion exchange, which are crucial for the mobility of contaminants in surface and groundwater systems, weathering, soil development, soil moisture behaviour, water composition and quality, and removal and sequestration of atmospheric carbon-dioxide.

The chemical behaviour of mineral-water interfaces is central to aqueous reactivity in natural waters, soil evolution, and atmospheric chemistry and is of direct relevance for maintaining the integrity of waste repositories and remediating environmental pollutants (Yanina and Rosso 2008).

Furthermore, phyllosilicates has been implicated in prebiotic synthesis of biomolecules and possibly the origin of life on earth (Hazen 2006; Hazen *et al.* 2008). Clay minerals are potentially catalytic surfaces for mineral-mediated biomolecules interactions, such as RNA polymerization and vesicles formation. These interactions can be driven by particle size, shape, composition, charge and surface area (Hanczyc *et al.* 2006; Kwon *et al.* 2006; Valdrè 2007).

Therefore, summarising, phyllosilicates surface properties depend on many factors such as, chemical composition, nature of the surface atoms, type and extension of defective sites, layer charge and, eventually, the nature of exchangeable cations. The interaction with other entities is also driven by the thermodynamic conditions (temperature and pressure) and the acid-base character (pH and ionic strength) of the surrounding environment. The interacting surfaces can be planar, terraces, or edge surfaces usually associated with defect sites and pH-dependent charges.

Techniques with a high spatial resolution are needed to analyse in details these physico-chemical properties and the local interactions at the mineral surfaces. In these terms, one of the most powerful and promising technique is Scanning Probe Microscopy (SPM). Recent developments of SPM have widened the spectrum of possible investigations that can be performed at a nanometric level on the surface of minerals. They range from physical

properties such as surface potential and electric field topological determination to spectroscopic analysis, either in air, in liquid or in a gaseous environment. Furthermore, new technological solutions give the possibility to probe single-molecule interactions at the mineral surfaces with previously unattainable force sensitivity (< pN). These features also promote SPM as a unique tool for bionanopatterning.

The search and characterization of new nanomaterials, and their application to nano-manipulate biomolecules are modern challenges of nanoscience and nanotechnology, and both synthetic and natural materials are widely investigated. The rapid growth in nanotechnology is increasing the request of engineered materials presenting at the surface nanostructures with features ranging from a few nanometres to hundreds of nanometres. For instance, biotechnology and microelectronics require the deposition of a large variety of materials such as polymers, nanoparticles, biomolecules and inorganics on either metal or insulting substrate surfaces with extremely high spatial precision (Xie *et al.* 2006, Zheng *et al.* 2008, Rosa and Liang 2009).

Biomolecular nanostructures show applications in molecular electronics, biomolecular arrays, biosensors such as for the organization of functional materials, to create nanoelectronic or nano-optical devices. DNA molecules can be employed as building blocks for superstructure construction and thus are being extensively investigated for application to biosensors, nanoscale electronic and quantum devices. Recently DNA molecules were also used as template for the formation of gold nanowires (Lin *et al.* 2007, Kim *et al.* 2010). Other studies referred to patterning of DNA on both nanolithographied or electrically charged surfaces (Chi *et al.* 2006, Kershner *et al.* 2009, Erdmann et al. 2010, Lin et al. 2005).

In addition, the research of nanomaterials with properties, such as shape, size, roughness and surface chemistry, suitable for a reliable biomolecular adsorption, self-assembly and patterning at a nanometre level is in general important for the fabrication of substrates.

Preliminary adsorption experiments on phyllosilicates showed different affinity of their basal surfaces when interacting with DNA molecules. Furthermore chlorite was preliminarily observed to adsorb also nucleotides.

8

Hence, it is evident a lack and a need of a better comprehension of phyllosilicates surface properties and interaction with biomolecules. This subject will be addressed in the present research project, focusing on the surface properties of chlorite and phlogopite.

These two minerals were selected because chlorite presents an interesting electrostatic behaviour due to its crystal structure made up of a negatively charged tetrahedral-octahedral-tetrahedral (TOT) layer plus a positively charged octahedral (brucite-like) sheet in the interlayer, and phlogopite is a mineral of the mica group whose tetrahedral-octahedral-octahedral structure is negatively charged and similar to the TOT of chlorite, but with cations balancing the TOT charge in the interlayer.

Chlorite is an important primary and common rock-forming mineral (Laird 1988) whose anisotropic surface properties greatly affect and control, for instance, industrial processes for the separation of mixtures and an amount of environmental processes involving interactions of the mineral surface with ions and biomolecules.

Phlogopite is one of the most common mica species (Deer *et al.* 2013), that is expected to have an important role in mass transport and metasomatism, and also in melting processes (Comodi 2004). This mineral has important applications as reinforcing filler in polymer technology (Verbeek 2002).

In the context of this research project the interaction of fundamental biomolecules (nucleotides and glycine) with chlorite and phlogopite surfaces was also studied; furthermore, the interaction of RNA and DNA with the surface of chlorite was investigated, since preliminary data revealed an anisotropy of the interactions that can drive the adsorption process.

In the following a brief view of the chapters content will be given.

The chapter "Materials and methods" firstly reports some basic notions on the occurrence, structure, crystal-chemistry and physico-chemical properties of chlorite and phlogopite. Then, the methods specifically developed in this research to deposit the biomolecules onto the mineral surfaces are described. Finally, the experimental techniques are introduced and analysed in terms of basic principles, technical solutions and probing limits. The experimental set-ups used in this research are described together with the experimental methodologies specifically developed and optimized in the context of this work, that are based on atomic

force microscopy, electric force microscopy, Kelvin probe force microscopy and nanolithography.

The four sub-chapters of "Results and discussion" deals with: (i) chlorite nanomorphology investigations, electric surface potential measurements and single or multiple layer removal by mechanical and voltage nanolithography; (ii) studies on the interaction of nucleotides, RNA, DNA and amino acids with chlorite surface and the application of the findings of these works to the creation of bio-nanopatterned surfaces; (iii) phlogopite nanomorphology and surface potential investigations, single and multiple layer removal and analytical surface measurements; (iv) studies on the interaction of nucleotides and amino acids with phlogopite surface.

4. *MATERIALS AND METHODS*

4.1. Phyllosilicates

According to the recommendations of the Association Internationale Pour l'Etude des Argiles (AIPEA) Nomenclature Committee relevant to clay mineralogy (Guggenheim *et al.* 2006) the terms "planes", "sheet" and "layer" refer to: a plane of one or more types of atoms; a tetrahedral or octahedral sheet composed of continuous 2D corner-sharing tetrahedra involving three corners and the fourth pointing in any direction, or edge-sharing octahedra, respectively; a layer containing one or more tetrahedral sheets and an octahedral sheet. There are two types of layer: "1:1 layer" with one tetrahedral and one octahedral sheet; "2:1 layer" with one octahedral sheet between opposing tetrahedral sheets. "Interlayer material" separates the layers. A "unit structure" is the total assembly and includes the layer and interlayer material. The smallest structural unit contains three octahedra: if one site is vacant the sheet is considered "dioctahedral", "brucite-like", whereas if all three sites are occupied the sheet is considered "trioctahedral", "gibbsite-like".

Other structural terms are: "lattice", a collection of equivalent points periodically distributed in space (it commonly refers to Bravais lattices); "Structure", which refers to the accepted atomic, ionic and molecular arrangement of atoms of a material (e.g., layer structure); "Polytypism", the existence of an element or compound in two or more layer-like crystal structures that differ in layer-stacking sequences. Polytypism permits differences in chemical composition between structures, not exceeding 0.25 atoms per formula unit of any constituent element. Otherwise the word "polytypoids" have to be used. *X*, *Y*, *Z*, or [100], [010], [001] are used for directions of crystallographic axes and *a*, *b*, *c* for the repeat distances along these axes.

A general classification scheme for phyllosilicates is presented in table 4.1.1. The charge per formula unit, *x*, that is calculated with averaging bulk techniques, is the net negative charge per layer, expressed as a positive number.

Table 4.1.1. Classification of planar phyllosilicates[a]

Layer type	Interlayer material[b]	Group	Octahedral character	Species
1:1	None or H_2O only ($x \approx 0$)	Serpentine-kaolin	Trioctahedral	Lizardite, berthierine, amesite, cronstedtite
			Dioctahedral	Kaolinite, dickite, nacrite, halloysite (planar)
			Di,trioctahedral	Odinite
2:1	None ($x \approx 0$)	Talc-pyrophyllite	Trioctahedral	Talc, willemseite, kerolite, pimelite
			Dioctahedral	Pyrophyllite, ferripyrophyllite
	Hydrated exchangeable cations ($x \approx 0.2\text{-}0.6$)	Smectite	Trioctahedral	Saponite, hectorite, sauconite, stevensite, swinefordite
			Dioctahedral	Montmorillonite, beidellite, nontronite, volkonskoite
	Hydrated exchangeable cations ($x \approx 0.6\text{-}0.9$)	Vermiculite	Trioctahedral	Trioctahedral vermiculite
			Dioctahedral	Dioctahedral vermiculite
	Non-hydrated mono- or divalent cations ($x \approx 0.6\text{-}0.85$)	Interlayer-deficient mica	Trioctahedral	Wonesite
			Dioctahedral	none
	Non-hydrated monovalent cations ($\geq 50\%$ monovalent, $x \approx 0.85\text{-}1.0$ for dioctahedral)	True (flexible) mica	Trioctahedral	Phlogopite, siderophyllite, aspidolite
			Dioctahedral	Muscovite, celadonite, paragonite
	Non-hydrated divalent cations ($\geq 50\%$ divalent, $x \approx 1.8\text{-}2.0$)	Brittle mica	Trioctahedral	Clintonite, kinoshitalite, bityite, anandite
			Dioctahedral	Margarite, chernykhite
	Hydroxide sheet (x = variable)	Chlorite	Trioctahedral	Clinochlore, chamosite, pennantite, nimite, baileychlore
			Dioctahedral	Donbassite
			Di,trioctahedral	Cookeite, sudoite
			Tri,dioctahedral	none
2:1	Regularly interstratified (x = variable)	Variable	Trioctahedral	Corrensite, aliettite, hydrobiotite, kulkeite
			Dioctahedral	Rectorite, tosudite, brinrobertsite
1:1, 2:1			Trioctahedral	Dozyite

[a] modified from Guggenheim *et al.* 2006
[b] x is the net layer charge per formula unit, given as a positive number

The negative charge is balanced by the positively charged interlayer material. The chlorite group has two octahedral sheets, thus fourth subgroups can be defined: fully dioctahedral chlorite; fully trioctahedral (the common form of chlorite); di,trioctahedral chlorite with a dioctahedral 2:1 layer and a trioctahedral interlayer; tri,dioctahedral structures are not known. Trioctahedral chlorite subgroup nomenclature is based on the dominant divalent octahedral

cation. Adjectival modifiers are used to clarify variations in chemical composition (e.g., Fe^{2+}-rich clinochlore).

Phyllosilicates polytypes are designated by Ramsdell-style notation (Guinier *et al.* 1984) where the number of layers is given as the first part of a structural symbol suffix, followed by an italics capital letter indicating the crystal system: *C* (cubic), *H* (hexagonal), *T* (trigonal with hexagonal Bravais lattice), *R* (trigonal with rhombohedral Bravais lattice), *Q* (quadratic or tetragonal), *O* (orthorhombic), *M* (monoclinic), and *A* (anorthic or triclinic).
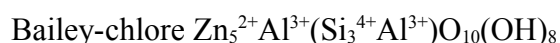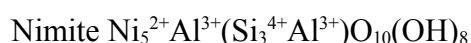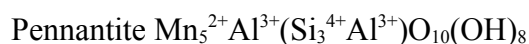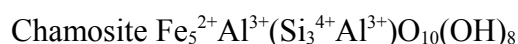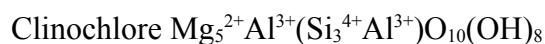
These recommendations will be used along the text.

4.1.1.   Chlorite group

The phyllosilicates are important rock-forming minerals comprising, for instance, biotite, muscovite, phlogopite and chlorite (Kodama 2011). Chlorite is a primary and common rock-forming mineral found in a great variety of rocks and geological environments including diagenetic, low- to medium-grade metamorphic and hydrothermally altered rocks (Laird 1988). It can replace pre-existing, typically ferro-magnesian, minerals or precipitate directly from solution (De Caritat *et al.* 1993). In a theory of mineral evolution (Hazen *et al.* 2008) the first appearance of chlorite is estimated when planetesimal accretion progressed and chondrite parent bodies became larger from 4.56 to 4.55 Ga, as low-temperature (typically < 100 °C) aqueous alteration product of olivine and pyroxene. Chlorite presents a wide range of non-stoichiometric compositional variations which depend on bulk-rock composition and the physico-chemical formation conditions, such as temperature, pressure, pH, activities of the metal cations dissolved in fluid, and of S_2, O_2, CO_2. The compositional variation is a source of information on the physico-chemical conditions of formation, and its use in estimating the temperature of formation is referred to as "chemical chlorite geothermometry" (Inoue *et al.* 2009). Chlorite is among the hydrous phases that may have an important role in upper mantle mass transport and melting processes (Zanazzi *et al.* 2006, 2007). H_2O can be stored in chlorite if enough aluminium is present in descending material, such as the pelitic oceanic sediment (Poli and Schmidt 2002). Consequently, the breakdown of this mineral phase will

determine the actual slab dehydration. Chlorite contains around 13 wt% of water. The most thermally stable chlorite composition is clinochlore.

Bayliss (1975) introduced a nomenclature for trioctahedral chlorites based on five end-members:

Clinochlore $Mg_5^{2+}Al^{3+}(Si_3^{4+}Al^{3+})O_{10}(OH)_8$

Chamosite $Fe_5^{2+}Al^{3+}(Si_3^{4+}Al^{3+})O_{10}(OH)_8$

Pennantite $Mn_5^{2+}Al^{3+}(Si_3^{4+}Al^{3+})O_{10}(OH)_8$

Nimite $Ni_5^{2+}Al^{3+}(Si_3^{4+}Al^{3+})O_{10}(OH)_8$

Bailey-chlore $Zn_5^{2+}Al^{3+}(Si_3^{4+}Al^{3+})O_{10}(OH)_8$

Other classification schemes for chlorites were recently proposed by Wiewióra and Weiss (1990), using an unified system of composition projection, and by Zane and Weiss (1996), using electron microprobe data evaluation.

Chlorite was selected in this research project because it presents an interesting electrostatic behaviour due to its crystal structure made up of a negatively charge tetrahedral-octahedral-tetrahedral (TOT) layer plus a positively charged octahedral (brucite-like) sheet in the interlayer.

The layer structure of chlorite, shown in figure 4.1.1, can be described as regularly stacked negatively charged 2:1 (tetrahedra-octahedra-tetrahedra, TOT) layers sandwiching a positively charged brucite-like, $Mg_3(OH)_6$ octahedral sheet (O_b) in the interlayer (Evans and Guggenheim 1988). This material contains several percent of Al both in the tetrahedral sites of the TOT substituting silicon and in the brucite-like sheet O_b substituting Mg. This double substitution of Al confers a positive charge to the brucite-like sheet and a negative one to the TOT surface. Chemically the octahedral sheet O_b is an Mg-Al-hydroxide. The TOT layer and O_b sheet are bonded to each other by a weak electrostatic and van der Waals force. The O_b sheet is 0.4-0.5 nm thick, whereas the TOT layer is 1 nm thick.

Because of the weak forces between the O_b sheet and the TOT layer, chlorite presents a unique surface characteristic: once cleaved it can expose simultaneously regions of the TOT (negative) and regions of hydroxyl groups belonging to the O_b sheet (positive), so that surface
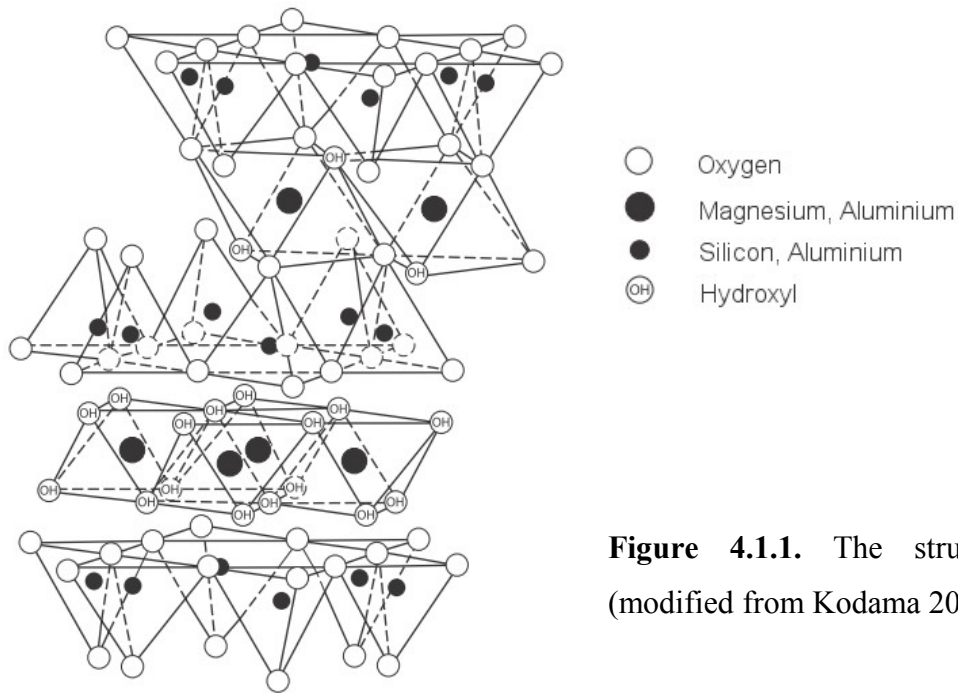
Figure 4.1.1. The structure of chlorite (modified from Kodama 2011).
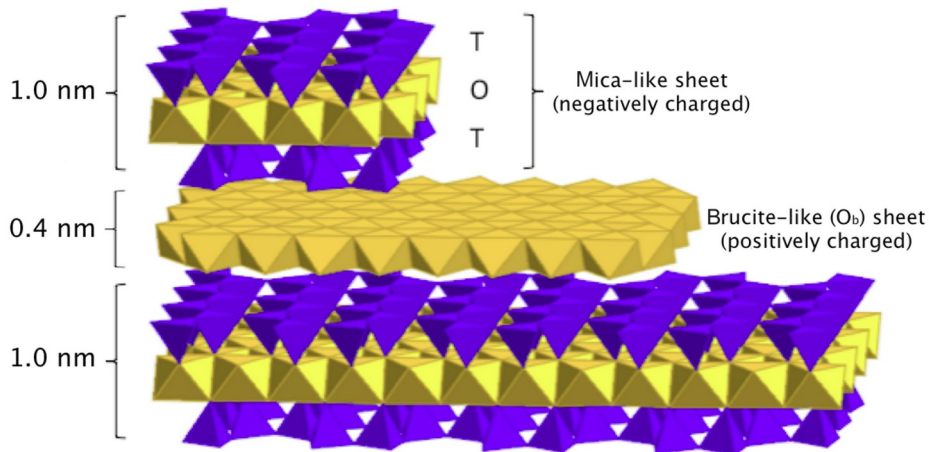
Figure 4.1.2. Structure of chlorite. A single positively charged brucite-like, $Mg_3(OH)_6$ octahedral sheet (O_b), is sandwiched between two negatively charged TOT layers by a weak electrostatic force. The simplest structural unit therefore consists of the repetition of a TOT layer and an octahedral sheet O_b in the interlayer (*i.e.*, $TOTO_b$ –$TOTO_b$-etc) with a periodicity along *c* of about 1.4 nm. The O_b sheet is 0.4 nm thick and made up of $Mg_3(OH)_6$, with some Al substituting Mg, whereas the TOT layer is 1 nm thick made up of $Mg_3(Si_3Al)O_{10}(OH)_2$, with some Al substituting Si.

15

steps of 1 or 0.4 nm in height with opposite charge can be observed by SPM as shown in this thesis and schematically in figure 4.1.2.

Electrostatic and van der Waals interactions between the TOT layer and the brucite-like sheet contribute to the stability of the structure. Different ways of positioning the TOT layer on the interlayer sheet create a large number of regular-stacking polytypes (Bailey 1988). The triclinic II*b*-4 polytype, with symmetry $C\bar{1}$, and the monoclinic II*b*-2 polytype, with symmetry *C*2/*m*, are the most abundant regular-stacking one-layer chlorites occurring in nature.

It is noteworthy to mention that the bridging oxygen, Si-O-Al, is similar to the bridging oxygen in zeolites (Sauer 1989), and recently Kelvin probe force microscopy and quantum mechanical simulations revealed the existence of Brønsted-Lowry catalytic sites at chlorite surface (Valdrè *et al.* 2011).

Fornasiero and Ralston (2005) investigated the electrokinetic properties of chlorite. The immersion of a mineral particle in an aqueous solution produces an electrically inhomogeneous region at the solid-solution interface. The mineral surface charge is balanced by a diffuse region of equal and opposite charge (counter ions) and is called electrical double layer (figure 4.1.3). Since in many cases adsorption processes at mineral-water interfaces can be controlled by the electrical double layer, it is of paramount importance to study mineral surface charge, potential and the behaviour of ions adsorbing as counter ions to maintain electroneutrality (Fuerstenau and Pradip 2005). Ions which interact with surface sites and adsorb lie at the inner Helmholtz plane; the closest distance of approach to the surface of hydrated counter ions is called outer Helmholtz plane (figure 4.1.3). Phyllosilicates are electrokinetically anisotropic as the isoelectric point (see Appendix) may be controlled by the measurement plane (i.e., face or edge). Fornasiero and Ralston (2005) determined the mean zeta potential (see Appendix) of chlorite by conducting electrophoretic mobility experiments in the pH range 4 to 10, measuring an isoelectric point at approximately pH 5.5, and a zeta potential from about 25 mV (pH 4) to about – 50 mV (pH 10). More recently, Alvarez-Silva and coworkers (2010) determined the point of zero charge (see Appendix) of chlorite using the Mular-Roberts tritation technique, comparing it with isoelectric point measurements by electrophoretic mobility in the pH range 3 to 10. Fresh and aged chlorite showed similar zeta

potential values, with the isoelectric point at pH < 3. The point of zero charge for 24-h aged chlorite was found at pH 4.7 regardless of the range in ionic strength used.
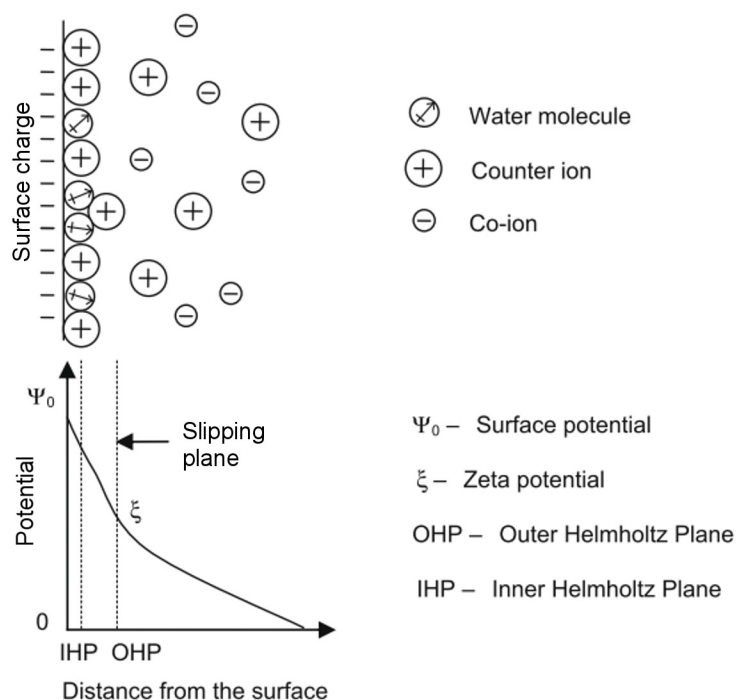
Figure 4.1.3. Scheme of the double layer structure and potential drop through the double layer (modified from Alvarez-Silva *et al.* 2010).

These discordant data, that were obtained by bulk measurements averaging on the whole surface, are not surprising, since the surface of chlorite can cleave as shown in the scheme of figure 4.1.2. Hence, positive and negative layers are present at the surface in a variable amount, depending on the cleavage mechanism. It is therefore important to study the surface properties of phyllosilicates at the nanometre scale.

4.1.2.   Phlogopite

Phlogopite is a common constituent of impure marbles. It occurs in metamorphosed magnesium limestones, dolomites and ultrabasic rocks (Deer *et al.* 2013). Phlogopite single crystals result from the contact and regional metamorphism of dolomite carbonates and the

crystallization and subsolids metasomatism of alkaline ultrabasic and carbonatitic magma. It is also suggested that phlogopite can occur as a result of mantle metasomatism (Fleet 2003). Phlogopite is stable up to temperatures of about 900°C at low water pressure and at about 1100°C at water pressures of 4–5 kbar. The limit of stability of phlogopite is close to the temperature of crystallization of basalt (Demange *et al.* 2012). This mineral is expected to have an important role in mass transport and metasomatism both along subducting slabs and within mantle wedges, and also in melting processes, contributing to the production of K-rich magma in the Earth's mantle. Geological evidence and experimental data indicates the stability of phlogopite in upper mantle conditions (Comodi *et al.* 2004). Russell and Guggenheim (1999) followed the structural evolution of phlogopite upon heating. Tutti and co-workers (2000) measured the thermal expansion of phlogopite. Pavese and coworkers (2003) investigated the elastic properties of a natural phlogopite by in-situ high-pressure X-ray powder diffraction (static compression up to 12 GPa).

The importance of phlogopite as a strategic mineral in the electrical industry during the World War II because of the high dielectric strength, thin laminae, high resistance to heat, flexibility and low unit cost promoted interest to develop methods for the commercial synthesis. For instance, Na-phlogopite, NH_4-phlogopite, Rb-phlogopite and Cs-phlogopite were synthesized (Fleet 2003). Phlogopite is together with muscovite a primary type of mica used as reinforcing filler in polymer technology (Verbeek 2002).
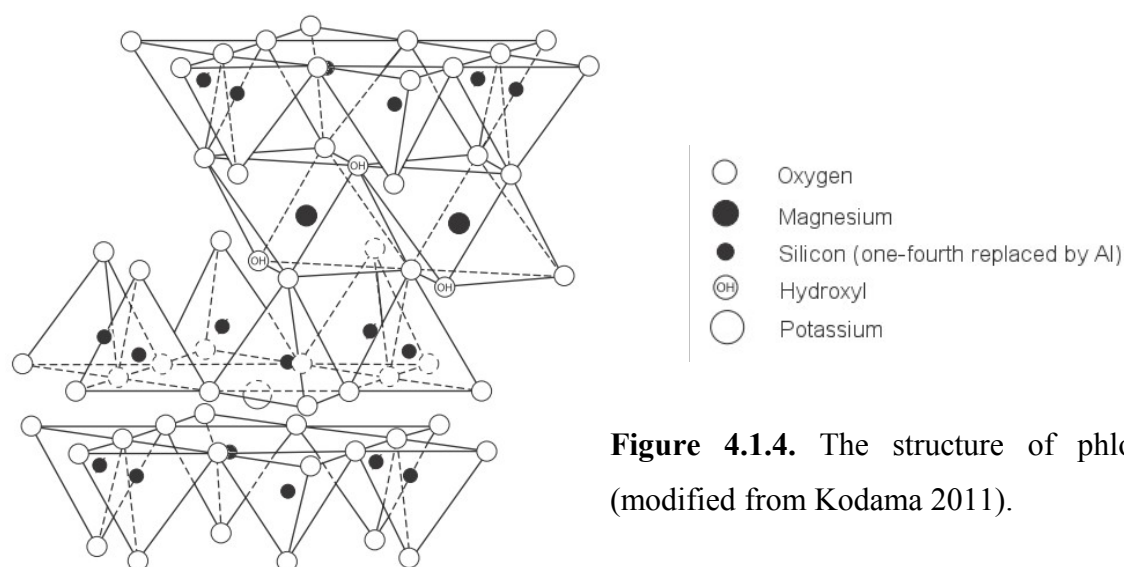

○ Oxygen
● Magnesium
• Silicon (one-fourth replaced by Al)
(OH) Hydroxyl
○ Potassium

Figure 4.1.4. The structure of phlogopite (modified from Kodama 2011).

18

Phlogopite was selected in this project because it is a mineral of the mica group whose tetrahedral-octahedral-octahedral structure is negatively charged and similar to the TOT of chlorite, but with cations balancing the TOT charge in the interlayer.

The crystal chemistry and structure of dioctahedral and trioctahedral micas were recently reviewed by Brigatti and Guggenheim (2002). Phlogopite is one of the most common mica species. It is a trioctahedral Mg-rich member of the mica group made up of negatively charged tetrahedral-octahedral-tetrahedral (TOT) layers, where Al substitutes for Si in a ratio near 1:3, and with K^+ cations in the interlayer zone (see figure 4.1.4). The TOT layers are held together by van der Waals and weak electrostatic forces. Phlogopite has an ideal chemical formula $KMg_3(AlSi_3)_4O_{10}(OH)_2$.

4.2. Fundamental biomolecules

The analysis of the interaction of biomolecules with substrates is of fundamental importance in a variety of scientific fields such as, for example, the research on prebiotic chemistry and the origin of life, environmental sciences, biosensors, tissue engineering, catalysis and biomaterials. Fundamental biomolecules, such as nucleotides, RNA, DNA and amino acids are extensively studied in medicine, molecular biology and biochemistry for their implications with human health. To deeply understand processes basically involving single biomolecules suitable approaches are envisaged.

Mineral surfaces are supposed to be critically implicated in the process of selection, concentration and organization of prebiotic organic molecules into the essential macromolecules of life (Hazen 2006). Theories and experiments point, for instance, to the role of mineral surfaces in the self-assembly of lipids, in polymerization of amino acids and nucleic acids, and the selective adsorption of organic species. In an hypothesis of chemical evolution, the origin of life was a geochemical event, approximately four billion years ago, dependent on reactions among the Archean ocean, a primitive atmosphere, and rocks and minerals (Hazen 2006). The emergence of life requires the emergence of biomolecules, the emergence of macromolecular systems, the emergence of self-replicating cycles of molecules and the emergence of molecular evolution by natural selection. The second emergent step by

which life's subset of biomolecules was selected and then concentrated from the dilute, diverse suite of prebiotic molecular species accumulated in the primitive oceans, could be mediated by the potential of mineral surfaces to select, concentrate and organize organic molecules.

Many of life's essential macromolecules, including nucleic acids and proteins, are chain-like polymers forming from water-soluble monomers (nucleotides and amino acids, respectively). The production of such biological macromolecules requires at least two steps: the correct molecules first must be concentrated and then assembled into the desired structure. One promising way to concentrate and assemble organic molecules is first to concentrate them on a surface. About the matter, rocks and minerals are studied for the ability of their surfaces to promote molecular concentration, adsorption, assembly and organic reactions.

Phyllosilicates presents atomically flat extended surfaces that are good candidates as substrates for the analyses on a single biomolecule level. In particular, chlorite has interesting anisotropic properties that could be exploited. In this sense, atomic force microscopy is a unique methodology since it can probe single molecules at the interaction with a mineral surface both in air and in a liquid environment.

In the following sections the deposition methods developed for the mineral surface – biomolecule studies will be presented.

4.2.1.   Nucleotides

The nucleotides used were homogeneous mixtures of deoxyadenosine triphosphate, deoxythymidine triphosphate, deoxyguanosine triphosphate, deoxycytidine triphosphate nucleotides (Invitrogen, USA). The mixtures were prepared in aqueous solution (Gibco, USA; Ultrapure water DNAse, RNAse free) to a final concentration of 10 µM at pH 7.5. Drops (each of 30 µl) were deposited onto (001) cleaved chlorite surfaces after its sterilization by means of a quartz sterilizer and nano-morphologically characterization by SPM. The sample was incubated for 10 minutes in a water vapour saturated environment, then rinsed with ultrapure water and dried in a flow of pure nitrogen.

The same procedure was adopted with phlogopite: drops (each < 0.2 µl) were deposited onto (001) cleaved phlogopite surfaces after its sterilization by means of a quartz sterilizer. The sample was incubated for 10 minutes in a water vapour saturated environment, then rinsed with ultrapure water and dried in a flow of pure nitrogen.

4.2.2.   RNA

The ribonucleic acid, RNA, used for the experiments was a single-stranded RNA from the bacteriophage MS2. It has an approximate molecular weight of 1200 kD, 3569 nucleotides, and is stored in a buffer solution with 10 mM Tris-HCl, 1 mM EDTA and a pH of 7.0 (Roche Diagnostics GmbH, Germany).

Before deposition all the surfaces were sterilized by means of a quartz sterilizer and nano-morphologically characterized by SPM. The RNA was diluted with an ultrapure aqueous solution (Gibco, USA; Ultrapure water DNAse, RNAse free) to concentrations of 1 nM and 0.1 nM. 20 µl aliquot drops were deposited onto freshly cleaved (001) chlorite surfaces. The sample was incubated for 10 minutes in a water vapour saturated environment, then rinsed with ultrapure water and dried in a flow of pure nitrogen.

4.2.3.   DNA

The deoxyribonucleic acid was a 48502 bp length linear double-stranded λ-DNA, diluted into a K-glutamate buffer, with 10 mM Tris HCl, and 1 mM EDTA, as commonly used for type III restriction endonuclease (Fermentas Life Sciences, USA). The final DNA concentration was 1 nM in an ultrapure aqueous solution (Gibco, USA; Ultrapure water DNAse, RNAse free) with a pH of 7.6. 20 µl aliquot drops were deposited onto the mineral surfaces after its sterilization by means of a quartz sterilizer and nano-morphologically characterization by SPM. The sample was incubated for 10 minutes in a water vapour saturated environment, then rinsed with ultrapure water and dried in a flow of pure nitrogen.

4.2.4.   Amino acids

Glycine molecules were provided as powders (Sigma-Aldrich Chemie Gmbh, Steinheim, Germany).

Before deposition all surfaces were sterilized by means of a quartz sterilizer and nano-morphologically characterized by SPM. Glycine powder was diluted with an ultrapure aqueous solution (Gibco, USA; Ultrapure water DNAse, RNAse free) with pH 7.6 to a final concentration of 150 μM. Drops of about 10 μl were deposited onto freshly cleaved (001) chlorite surfaces. The sample was incubated for 10 minutes in a water vapour saturated environment, then rinsed with ultrapure water and dried in a flow of pure nitrogen.

The same procedure was adopted with phlogopite: drops, each < 0.2 μl, were deposited onto freshly cleaved (001) phlogopite surfaces; the sample was incubated for 10 minutes in a water vapour saturated environment, then rinsed with ultrapure water and dried in a flow of pure nitrogen.

4.3. Atomic Force Microscopy

Atomic Force Microscopy (AFM) – based methods were used in this thesis. These methods are variable and different in function of the quantity to be measured. Some of these methods (EFM-type, Kelvin probe – type and nanolithography) were suitably developed in the context of this research project.
In the section "Fundamentals" the working principles of the AFM-based methods will be introduced. Nowadays, AFM cantilevers are supplied by the manufacturers without an accurate value of the force constant, therefore the section "Calibration of AFM cantilevers" deals with the method used for the calibration of the force constant whereas the probe-to-sample force had to be accurately measured. Finally, the section "AFM equipment" will report the specific experimental configuration used during this project.

4.3.1.   Fundamentals

Scanning Probe Microscopy (SPM) is a type of microscopy that forms images of surfaces by means of a scanning physical probe. The first type of SPM was the scanning tunnelling microscopy invented by Binnig and Rohrer in 1981. Atomic Force Microscopy (AFM) was the second type of SPM, invented by Binnig, Quate and Gerber in 1985. SPM techniques rapidly gained a great importance in a variety of scientific and technological research fields. The rapid development of this type of microscopy has brought a very large and continuously increasing number of SPM-based methodologies (Friedbacher and Fuchs 1999, Poggi *et al.* 2004).

In AFM (see figure 4.3.1) a probing tip is mounted on the free end of a microlever (cantilever), and in the more general case it is brought into contact with the sample surface in a continuous or intermittent contact mode. The length of the microcantilever is typically of the order of hundreds of micrometers, whereas the tip height is of the order of some micrometres with an apical radius of curvature ranging from some nanometres to tens of nanometres.
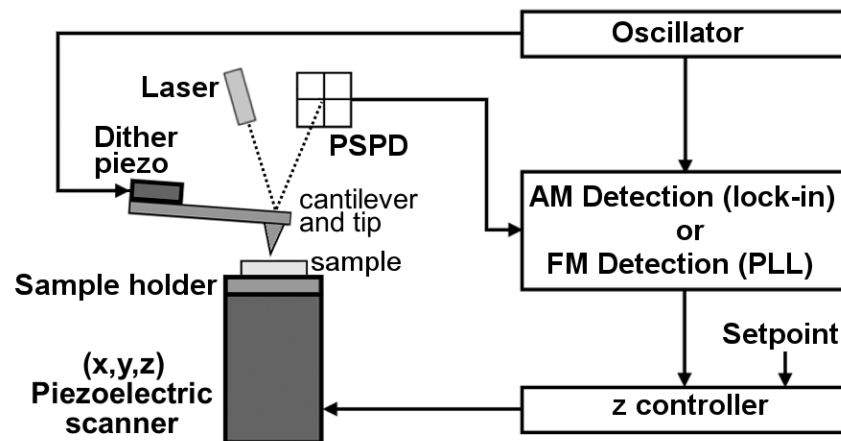

Figure 4.3.1. Schematic diagram showing the main components of the Atomic Force Microscope (AFM) used in the context of this research project. AM = amplitude modulation; FM = frequency modulation; lock-in = lock-in amplifier; PLL = phase-locked loop; PSPD = position sensitive photodetector.

When the tip is approaching to the sample different forces are encountered. Generally speaking, for a small tip-sample distance z, the force is repulsive ($z < 1$ nm) and its intensity is about 1 nN; for larger distances the force is attractive and weaker, about 1 pN. Long range attractive or repulsive forces (up to 100 nm) are, for instance, the electrical and magnetic ones. Under about 10 nm attractive interactions are attributed to van der Waals forces, i.e., dipolar interaction between the atoms or molecules of both the tip and the surface materials (Saint Jean *et al.* 1999). When the tip is in contact with the sample surface (in the ideal case a single atom contact) repulsion occurs due to the overlapping electronic shells of tip and sample atoms. These interatomic repulsive forces can be utilized to trace the surface topography with atomic resolution, since they are short-range forces, confined to an extremely small area. The long range forces interact across larger surface areas and are therefore not atomic resolving. In ambient conditions, meniscus forces formed by water adhesion layers can also be present.

The interactive forces measured by AFM can be explained in term of potential energy. The potential energy of two atoms, at a distance r from each other, can be approximated by the Lennard-Jones potential (Mironov 2004):

$$U_{LD}(r) = U_0 \left\{ -2 \left(\frac{r_0}{r} \right)^6 + \left(\frac{r_0}{r} \right)^{12} \right\} \qquad (4.3.1)$$

where the first term of the sum takes into account long distance attraction caused by dipole-dipole interaction and the second term describes the short range repulsion due to the Pauli exclusion principle. r_0 is the equilibrium distance between atoms, where the potential energy has a minimum, U_0 (figure 4.3.2).
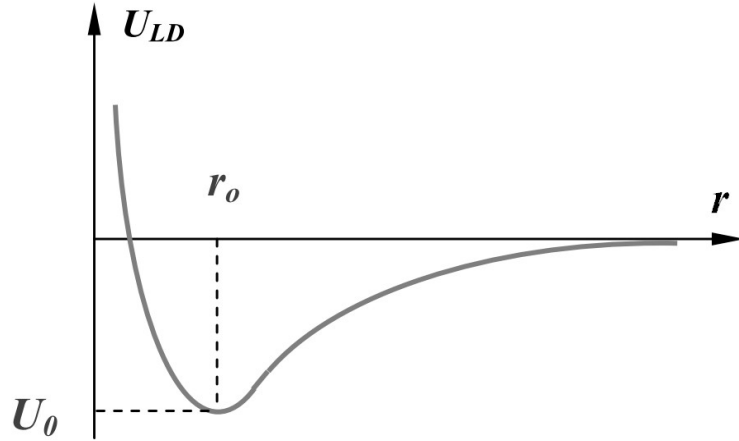
Figure 4.3.2. Qualitative trend of the Lennard-Jones potential.

The tip-sample interaction energy can be derived adding elementary interactions for all the atoms of the tip and of the sample (Mironov 2004):

$$W_{PS} = \iint\limits_{V_P V_S} U_{LD}(r - r')\, n_P(r')\, n_S(r)\, dV\, dV' \qquad (4.3.2)$$

where $n_S(r)$ and $n_P(r')$ are the atoms densities in the tip and the sample.

The interaction force of a tip with a sample can be consequently calculated (Mironov 2004):

$$\vec{F}_{PS} = -grad\,(W_{PS}) \qquad (4.3.3)$$

Atomic force microscopy can be effectively used to image mineral surfaces at the nanoscale. In AFM there are two main modes of operation: amplitude modulation (AM-AFM) and frequency modulation (FM-AFM). In amplitude modulation the AFM probe is mechanically excited at the cantilever fundamental frequency by a piezoelectric element and the oscillatory motion is detected by the optical system (Lee and Jhe, 2006). AM-AFM uses a large amplitude of oscillation (dozens of nm) to probe the sample surface. The oscillation amplitude is used as the feedback parameter to image the sample topography. This can be achieved by means of a feedback loop using a lock-in amplifier. The AM operational mode was implemented for the AFM measurement performed in this thesis.

By mapping the phase shift between the excitation signal and the response of the cantilever during the scan, phase imaging may provide further information beyond simple topographical mapping to detect, for instance, variations in composition, adhesion, friction and viscoelasticity. Applications include qualitative differentiation among regions of high and low surface adhesion or hardness, identification of contaminants and mapping of different components in composite materials.

In frequency modulation mode (FM-AFM), an increase in sensitivity is achieved over AM-AFM (Giessibl, 2003). The signal used to produce the image comes from direct measurement of the resonant frequency of the cantilever, which is modified by the tip–surface interaction. In FM-AFM the cantilever is kept oscillating at its current resonant frequency, achieved by means of a phase-locked loop (PLL). The spatial dependence of the frequency shift induced in the cantilever motion by the tip–sample interaction is used as the source of topographical contrast.

Sub-atomic resolution has been achieved by FM-AFM (Giessibl et al., 2000). It is also a promising technique in the imaging of organic systems, for example single- and double-stranded DNA. Recently, high resolution was also achieved in liquid both of minerals (e.g., muscovite) and biomolecules (Fukuma 2009).

By detecting and precisely measuring the short-range chemical forces between the tip and surface atoms using FM-AFM, Sugimoto et al. (2007) achieved the chemical identification of individual surface atoms in ultrahigh vacuum at room temperature.

4.3.2.   Calibration of AFM cantilevers

The present section introduces the problem of the calibration of cantilevers for atomic force microscopy and describes the methodology adopted in the context of this research project for the calibration of cantilevers used for quantitative force measurements. In this research project, in order to estimate the spring constant the method of Sader and co-workers (1999) was used.

The use of the atomic force microscope for the measurement of nano-scale forces in a quantitative manner (such as, for instance, electrostatic, van der Waals, inter/intramolecular

26

forces of single biomolecules) has rosen the issue of precise and accurate methods for calibrating the spring constant of the cantilever since its invention in 1986. As spring constant calibration methods have proliferated, attempts have been made to compare techniques and to develop a standard traceable method (Gates *et al.* 2011).

Many techniques have been developed for *in situ* spring constant measurement, such as to allow the user to routinely and independently perform calibrations while operating the AFM. Dimensional approaches, methods probing the cantilever static deflection induced by a calibrated load, and approaches monitoring the dynamic vibrational response of the cantilever have been devised (Sader *et al.* 2012, Frentrup and Allen 2011).

Common spring constant calibration methods often neglect the tip mass and any non-uniformity in the thickness of the probe along its length. In this research project, in order to estimate the spring constant the method of Sader and co-workers (1999) was used. When the first dynamic mode of the AFM cantilever is used, the error in the estimation of the spring constant is between 4% and 9% for a cantilever with about 30% of linear thickness variation along its length (Frentrup and Allen 2011).

In the Sader method (Sader *et al.* 1999) the spring constant, k, of a rectangular cantilever is calculated from its plan view dimensions, the measurement of its quality factor (see Appendix) in fluid and the resonant frequency:

$$k = 0.1906 \rho_f b^2 L Q_f \Gamma_i(\omega_f) \omega_f^2 \qquad (4.3.4)$$

where ρ_f is the density of the fluid, b the cantilever width, L the length of the cantilever, Q_f the quality factor of the fundamental mode of the cantilever in fluid, ω_f the resonant frequency in fluid, and Γ_i the imaginary component of the hydrodynamic function (see the work of Sader, 1998, for the analytical expression) that only depends on the Reynolds number $Re = \rho_f \omega b^2/(4\eta)$, being η the viscosity of the surrounding fluid. This expression is valid provided the quality factor $Q_f \gg 1$.

To obtain the resonant frequency, ω_f, and the quality factor, Q_f, the thermal noise spectra of the cantilever was measured using a digital spectrum analyser. The resonance peak of the fundamental mode was fitted to the power response function of a simple harmonic oscillator:

$$P(\omega) = A_{\text{white}} + \frac{B\,\omega_f^4}{(\omega^2 - \omega_f^2)^2 + \dfrac{\omega^2 \omega_f^2}{Q_f^2}} \qquad (4.3.5)$$

where ω is the frequency, B is the dc power response ($V^2 \cdot Hz^{-1}$) of the cantilever measured from the photodetector, and A_{white} is a white-noise floor ($V^2 \cdot Hz^{-1}$). The fitting parameters were A_{white}, B, ω_f, and Q_f.

When a large spring constant precluded the thermal noise spectrum measurement because of a low vibration amplitude, the cantilever was driven at a frequency near its fundamental mode resonance peak by a drive amplitude not large enough to invoke non-linearities.

4.3.3.   AFM equipment

The SPM analysis was performed by using a Multimode atomic force microscope (Digital Instruments, Santa Barbara, California) with Nanoscope IIIa controller. The same analyses were performed by using also a Nanonis SPM control system (Nanonis – SPECS Zurich GmbH, Zurich, Switzerland) equipped with two oscillation controller modules (with digitally integrated PLL/lock-in). The precise control of the relative tip-sample position was achieved by an nPoint closed loop MultiMode scanner (nPoint, Inc., Madison, WI, USA) with a C-300 DSP closed-loop controller.

Bruker (Bruker Co., Camarillo, CA, USA) MPP-11100 rectangular probes (nominal force constant, k, 40 N·m^{-1}, nominal resonant frequency 300 kHz) working in intermittent contact mode and NP-type triangular probes (nominal force constant, k, 0.06 - 058 N·m^{-1}) working in contact mode were used for the morphological characterization. Furthermore, Nanoworld (Nanoworld AG, Neuchâtel, Switzerland) EFM-type (nominal k = 2.8 N/m, nominal resonant frequency of 70 kHz) and NCHPt-type (nominal k = 42 N/m, nominal resonant frequency of 320 kHz) rectangular probes were used.

NP-type AFM probe is made of silicon nitride. A single chip brings four triangular shaped cantilevers with different force constants, from 0.58 N/m to 0.06 N/m. The tip shape is pyramidal with a square base. The tip has a radius of curvature of about 20 nm, heigth of 2 μm, and front/back/side angles of 35°. MPP-11100 probe has an anisotropic tip geometry with a tip height of about 17 μm, front, back and side angles of about 15°, 25° and 17.5° and a nominal radius of curvature of about 10 nm. The cantilever is of rectangular type made of uncoated phosphorous (n) doped Si. Nominal working frequency 300 kHz, k=40 $N \cdot m^{-1}$, cantilever length 125 μm, width 35 μm. EFM and NCHPt-type of probes have an anisotropic tip geometry with a tip height of about 12 μm, front, back and side angles of about 25°, 15° and 22.5° and a nominal radius of curvature of about 25 nm. The cantilever is of rectangular type made of antimony (n) doped Si, plus a Pt-Ir coating. EFM-type probe has a nominal working frequency 75 kHz, k = 2.8 $N \cdot m^{-1}$, cantilever length 225 μm, width 28 μm. NCHPt-type probe has a nominal working frequency 320 kHz, k = 42 $N \cdot m^{-1}$, cantilever length 125 μm, width 30 μm.

All the SPM observations were conducted in air, at atmospheric pressure, RT (~25° C) and RH of about 50 %.

4.4. Electric force microscopy and Kelvin probe

In SPM the surface potential can be measured by using three main methods: static electric force microscopy (EFM), dynamic EFM and Kelvin probe force microscopy (KPFM). The three methods differ each other in terms of type of signal detected, sensitivity and operating easiness.

A methodology recently developed to study the electric force sensitivity and resolution of conductive EFM cantilevers (Valdrè and Moro 2008a, 2008b) was here applied to the characterization of minerals surface potential by means of a static EFM method. In static EFM the cantilever deflection caused by the electrostatic force acting between the probe and the specimen surface is measured. The effective electrostatic force depends on the voltage difference between the probe and the specimen and also on both tip and cantilever geometry

(shape and size). For this reason, the effect of both tip and cantilever on the total force gradient must be taken into account for a thorough understanding of the experimental data.

The electrostatic interaction between a conductive tip and sample is given by

$$F = \frac{1}{2} \frac{\partial C(z)}{\partial z} V^2 \qquad (4.4.1)$$

where $C(z)$ is the system capacitance, z is the tip–sample distance, and V the tip–sample electric potential difference. At equilibrium, the electrostatic force is balanced by the reacting elastic force of the cantilever, and its measured deflection is directly related to the electrostatic force acting on the cantilever system.

In static EFM, by means of a Force Volume experiment, a bi-dimensional matrix of force curves can be acquired, reconstructing the force field above the sample. The probe is brought in contact with the sample in a controlled way by means of the piezoelectric scanner and then retracted to a chosen height. The cantilever deflection, ΔL, measured point by point during the approach-withdrawal cycle is related to the electrostatic force, F, by means of the elastic constant of the cantilever, k_{L}:

$$F = k_L \Delta L \qquad (4.4.2)$$

A numerical simulation of the same experiment can relate the probe deflection to the mineral surface potential. The real geometry of cantilever and tip can be reconstructed by computer-aided design (CAD). The electro-mechanical interaction between the probe and the mineral surface can be studied by 3D finite element analysis (FEA). The coupling between the probe and the mineral sample is modelled with the numerical formulation of the Maxwell stress tensor. The Maxwell stress tensor, neglecting electrostriction, is given by:

$$\vec{\vec{T}} = \varepsilon \vec{E} \vec{E} - \frac{1}{2} \varepsilon \vec{E} \cdot \vec{E} \delta \qquad (4.4.3)$$

30

where $\vec{E}$ is the electric field, ε the dielectric tensor and δ the Kroneker delta.

The finite element analysis allows to determine the mineral surface potential and further to discriminate the contribution of the various probe areas (tip-apex, tip sides, cantilever) to the measured force, to calculate the spatial resolution of the probe and the force sensitivity.

Dynamic mode EFM was also applied to the investigation of minerals surface potential. In dynamic EFM, a piezo-mechanically driven conductive cantilever is oscillating above the sample surface. In this case, frequency, amplitude and phase detection are used to study the tip–surface interactions. By using the small amplitude approximation, the interactions can be mapped point by point, eliminating the ambiguities which occur if large amplitude techniques are used. At small amplitudes the resonance frequency ω_0 is directly related to the interaction stiffness k_{ts}, which is the negative value of the force gradient:

$$k_{ts} = k_L \left(\frac{\omega_0^2}{\omega_{0f}^2} - 1 \right) \qquad (4.4.4)$$

where ω_{0f} is the cantilever free resonance frequency and k_L the elastic constant.

Measuring the frequency shift we can obtain ω_0 and then the force gradient. The electrostatic force can be associated to the sample surface potential by a numerical simulation of the probe-sample interaction.

In the configuration of a material with fixed charges at its surface, sandwiched between a conductive plane substrate and the EFM tip, the total electrostatic force can be expressed as:

$$F = \frac{1}{2} \frac{dC(z)}{dz} V^2 + \frac{Q_S Q_t}{4\pi \varepsilon_r \varepsilon_0 z^2} \qquad (4.4.5)$$

where $C(z)$ is the tip-substrate capacitance, V is the tip to substrate voltage, Q_S is the static charge, Q_t is the total charge induced in the tip, ε_0 is the permittivity of free space and ε_r

describes the dielectric constant of the materials between the conductive plane substrate and the EFM tip.

In Kelvin probe force microscopy (KPFM) the tip is biased directly by $V_{tip} = V_{dc} + V_{ac} \sin(\omega t)$ to a metallic sample or substrate (Nonnenmacher *et al.*, 1991). In this case, the capacitive force F between the tip and the surface is

$$F(z) = \frac{1}{2} \frac{\partial C(z)}{\partial z} (V_{tip} - V_S)^2 \qquad (4.4.6)$$

where V_s is the surface potential or contact potential difference (between tip and sample), and $C(z)$ is the tip–surface capacitance, which is dependent on the tip size and geometry, surface topography and tip–surface separation z. The first harmonic of the force F_ω is related to the difference between the constant component of the tip bias V_{dc} and the surface potential V_s by

$$F_\omega(z) = \frac{\partial C(z)}{\partial z} (V_{dc} - V_S) V_{ac} \sin(\omega t) \qquad (4.4.7)$$

By adjusting V_{dc} to nullify the force, we obtain point by point a surface potential map of V_s.

If static charges Q_s are present at the surface, a supplementary Coulomb force arises between the static charges Q_s and the ac charge induced on the tip, which is $C \cdot V_{ac}$ (Nyffenegger *et al.*, 1997; Girard, 2001). In this case, F_ω can be written as:

$$F_\omega(z) = \left[\frac{\partial C(z)}{\partial z} (V_{dc} - V_S) - \frac{Q_S C(z)}{4 \pi \varepsilon_r \varepsilon_0 z^2} \right] V_{ac} \sin(\omega t) \qquad (4.4.8)$$

The sign and position of charge Q_S can be in principle obtained, but the measurement strongly depends on the particular tip to sample configuration and is not as simple as for voltages, however an indication of the related surface potential can be obtained.

Typically, Kelvin Probe measurements are achieved by a dual-pass procedure. First, the topographic profile is recorded, then the tip is kept at an arbitrary chosen height above the sample and moved following the topographic profile, such as to minimize the interferences of the sample morphology on the electric potential signal.

To improve the surface potential measurements of the mineral samples in term of sensitivity and spatial resolution, this research project involved the development of recently presented single-pass procedures (Ziegler *et al.*, 2007). In this innovative method the probe measures simultaneously the morphology and the surface potential with shortening of the scanning times. The tip to sample distance is minimized, thus maximizing the spatial resolution. To avoid the coupling of the topographical to the surface potential signal the Kelvin feedback works at a higher flexural mode.

To be cited, the multifrequency electric force microscopy (MF-EFM) is another single-pass method by which qualitative information on the surface potential of the sample can be obtained (Stark *et al.,* 2007).

KPFM surface potential measurements were performed with a typical spatial resolution of tens of nm and a sensitivity of the order of mV. Pt-Ir coated Nanoworld (Nanoworld AG, Neuchâtel, Switzerland) EFM-type (nominal k = 2.8 N/m, nominal resonant frequency of 70 kHz) and NCHPt-type (nominal k = 42 N/m, nominal resonant frequency of 320 kHz) rectangular probes were used. In the dual-pass mode the tip was kept at a constant height of about 10 nm above the surface. Au coated Bruker (Bruker Co., Camarillo, CA, USA) NP-type triangular probes (nominal force constant, k, 0.06 - 058 $N \cdot m^{-1}$) were also used. All the SPM observations were conducted in air, at atmospheric pressure, RT (~25° C) and RH of about 50 %.

4.5. Nanolithography

Lithography is presently produced by various methods, among which scanning probe microscopy (SPM), electron beam lithography, nano-imprint lithography (Vershuuren *et al.* 2012), optical lithography (Megouda *et al.* 2012) and micro-contact printing (Hnilova *et al.* 2012).

Scanning probe microscopy is widely used for writing, by etching or depositing, nanoscale patterns on flat surfaces (Wang *et al.* 2009, Fenwick *et al.* 2009, Huo *et al.* 2010, Tang *et al.* 2006, Dinelli *et al.* 2010, Pires *et al.* 2010, Gozen *et al.* 2010, Saavedra *et al.* 2010, Ramsier *et al.* 2001, Inoue *et al.* 2003, Lyuksyutov *et al.* 2003). These patterning methods have been so far performed on homogeneous inorganic substrates, in particular silicon, silicon nitride, thin metal films and zirconium (Avouris *et al.* 1997, Lemeshko *et al.* 2001, Onuki *et al.* 2002, Chien *et al.* 2001, Farkas *et al.* 2003, Zheng *et al.* 2008). The depth resolution of the nano-pattern in these cases is of the order of 1 nm. Most of these substrates is not atomically flat, requires time-consuming preparation procedures and is chemically uniform across the surface (Garcia *et al.* 2006, Rosa and Liang 2009, Ogaki *et al.* 2010).

A nanolithographic method was developed in this thesis to remove single TOT layers or brucite-like sheets in a controlled way. Nanolithography allows to evaluate the adhesion forces between the structural layers of chlorite and phlogopite, that are weak electrostatic and van der Waals forces. Furthermore, by means of nanolithography it is also possible to made topographical markers useful to recognise the surface areas to be investigated with subsequent chemical analysis.

The research conducted in this thesis demonstrates that, by taking into account the crystal-chemistry and surface potential properties of chlorite, it is possible to perform well-controlled etching of the substrate with sub-nanometre depth resolution and tens of nm in lateral resolution (see section 5.1.3).

The findings of this research were successfully used to construct atomically flat charged patterns, designed to guide DNA deposition along predetermined directions without need of any chemical functionalization of the surface (see section 5.2.5).

4.5.1. Experimental set-up

For SPM measurements (topography and Kelvin probe analysis) and nanolithography it was used a Nanonis SPM control system (Nanonis – SPECS Zurich GmbH, Zurich, Switzerland) equipped with two oscillation controller modules (with digitally integrated PLL/lock-in) and a software lock-in detector module. The precise control of the relative tip-sample position was achieved by an nPoint closed loop MultiMode scanner (nPoint, Inc., Madison, WI, USA) with a C-300 DSP closed-loop controller; z position noise of 0.1 nm.

A Veeco DI Nanoman II AFM and a Multimode with the low noise electronics of the Nanoscope IVa controller (Veeco Instruments Inc., Santa Barbara, CA, USA) were also used. The electronics and (X;Y;Z) closed-loop control enabled high-resolution and reproducibility of imaging with Z sensor noise less than 0.06 nm rms. MPP-11100 (Bruker Co., Camarillo, CA, USA) silicon cantilevers were used for mechanical lithography, and MESP (Bruker, USA) cantilevers for voltage lithography and surface potential measurements. For all the experiments the chlorite and phlogopite samples were mounted on a properly grounded conductive AFM support.

MESP probes have an anisotropic tip geometry with a tip height of about 10 μm, front, back and side angles of about 25°, 15° and 22.5° respectively and a nominal radius of curvature of about 25 nm. The cantilever is of rectangular type made of Antimony doped Si, covered on the front side by a bottom layer of 1-10 nm of Cr and a top layer of 10-150 nm of Co/Cr. Nominal working frequency 75 kHz, k=2.8 N m^{-1}, cantilever length 225 μm, width 28 μm.

MPP-11100 probes have an anisotropic tip geometry with a tip height of about 15 μm, front, back and side angles of about 15°, 25° and 17.5° and a nominal radius of curvature of about 10 nm. The cantilever is of rectangular type made of uncoated phosphorous (n) doped Si. Nominal working frequency 300 kHz, k=40 N m^{-1}, cantilever length 125 μm, width 35 μm.

4.6. Micro-Raman spectroscopy

Some crystals of phlogopite were analysed with micro-Raman spectroscopy. In the following, the theoretical and experimental fundamentals of the method used in this project will be described.

4.6.1.   Theory of Raman scattering

Raman scattering is a physical phenomenon used to obtain information about the structure and properties of molecules from their vibrational transitions (molecular spectroscopy). It is a two-photon event in which the property of the molecule involved is the change in the polarizability of the molecule with respect to its vibrational motion. The interaction of the incoming radiation with the polarizability creates an induced dipole moment in the molecule. The induced dipole moment emits radiation containing the observed Raman scattering. The light scattered by the dipole contains both Rayleigh and Raman scattering. The first one is the light scattered at the frequency of the incident radiation, the second one is shifted in frequency (energy), with respect to the incident radiation, by the vibrational energy that is gained or lost in the molecule. The polarizability tensor has a first Cartesian component associated with the incident photon and a second component associated with the scattered photon. The two photons are linked by a single quantum mechanical process (coherent event). If the molecule gains vibrational energy, the process is known as Stokes Raman scattering, whereas if the molecule loses vibrational energy the scattering is called anti-Stokes Raman.

The Raman signal was discovered by the Indian physicist C. V. Raman in 1928. Raman spectroscopy mainly developed starting from the sixties thanks to the advent of the laser.

4.6.2.   The Raman tensor

In the Raman scattering of light by molecules changes in the polarization state of the light has effect on the nature and information content of the scattered light. The light scattering intensity is described by the following relation (Lewis and Edwards 2001):

36

$$I(\tilde{e}^d, \tilde{e}^i) = 90\, K \langle |\tilde{e}_\alpha^{d\,*}\, \tilde{\alpha}_{\alpha\beta}\, \tilde{e}_\beta^i|^2 \rangle \qquad\qquad K = \frac{1}{90} \left(\frac{\omega^2 \mu_0 \tilde{E}^{(0)}}{4\pi R} \right)^2 \qquad\qquad (4.6.1)$$

where $\tilde{\alpha}_{\alpha\beta}$ is the polarizability (scattering tensor), $\tilde{e}_\alpha^i$ and $\tilde{e}_\alpha^d$ the polarization vectors for the incident and scattered radiation, respectively. An average on all the molecule orientation angles to the laboratory frame of reference is performed. In general, nine terms (xx, xy, xz, yx, yy, yz, zx, zy, zz) are present within the vertical brackets. The tilde indicates that a quantity can be complex, the asterisk superscript the complex conjugation. ω is the angular frequency of the scattered light, μ_0 the magnetic permeability, $\tilde{E}^{(0)}$ the electric field strength of the incident laser, R the distance from the scattering origin to the detector.

The Raman polarizability tensor is (Lewis and Edwards 2001):

$$\tilde{\alpha}_{\alpha\beta} = \frac{1}{\hbar} \sum_{j \neq m,n} \left(\frac{\langle m|\hat{\mu}_\alpha|j\rangle \langle j|\hat{\mu}_\beta|n\rangle}{\omega_{jn} - \omega_0 + i\Gamma_j} + \frac{\langle m|\hat{\mu}_\beta|j\rangle \langle j|\hat{\mu}_\alpha|n\rangle}{\omega_{jm} - \omega_0 + i\Gamma_j} \right) \qquad \hat{\mu}_\alpha = \sum_k e_k r_{k\alpha} \qquad (4.6.2)$$

where $\hbar$ is Planck's constant divided by 2π, and the summation takes place over all the excited electronic states, j, of the molecule, n and m differing by a vibrational quantum of energy. ω_{jn} is the angular frequency difference between the states j and n, $i\Gamma_j$ are imaginary terms proportional to the width of the vibronic state j. The first term within the summation is called the resonance term as the difference between the jn transition frequency and the laser frequency vanishes at the resonance condition. Quantum mechanical matrix elements are given within the angular brackets, with $\hat{\mu}_\alpha$ the electric dipole moment operator being the summation in the αth direction over the charge and position of all the electrons k of the molecule. The matrix element with the operator $\hat{\mu}_\alpha$ describes the scattered radiation interaction, whereas that with $\hat{\mu}_\beta$ the incident radiation interaction. From right to left the resonance term describes the laser photon – molecule interaction and the creation of a scattered photon, the nonresonance term inverts the order of the two events.

If the sample molecules are randomly oriented with respect to the laboratory axes, special linear combinations of polarizability tensor, called invariants, has to be taken into account.

The invariants are independent of the molecule orientation and allow to write the polarizability tensor expressions independently of the molecule orientation. All Raman intensities from samples with randomly oriented molecules are described by three invariants: the isotropic invariant, the symmetric anisotropy, the antisymmetric anisotropy. Three scattering geometries can be defined for laser radiation incident along the laboratory positive z-axis: forward scattering (0°) along the positive z-axis, right-angle scattering (90°) along the y-axis, and backscattering (180°) along the negative z-axis.

4.6.3.   Experimental set-up

Micro-Raman measurements were performed with a Dilor (Horiba Jobin Yvon S.A.S., Longjumeau Cedex, France) Raman spectrometer, model LabRAM 010 (figure 4.6.1). The spectrometer has a focal length of 300 mm and is equipped with an integrated Olympus optical microscope, a set of 10X, 50X and 100X objectives, and a CCD camera (1024 X 128 pixels; pixel = 27 nm, 16 bit dynamic range) as photodetector with a Peltier system cooling under 210 K.
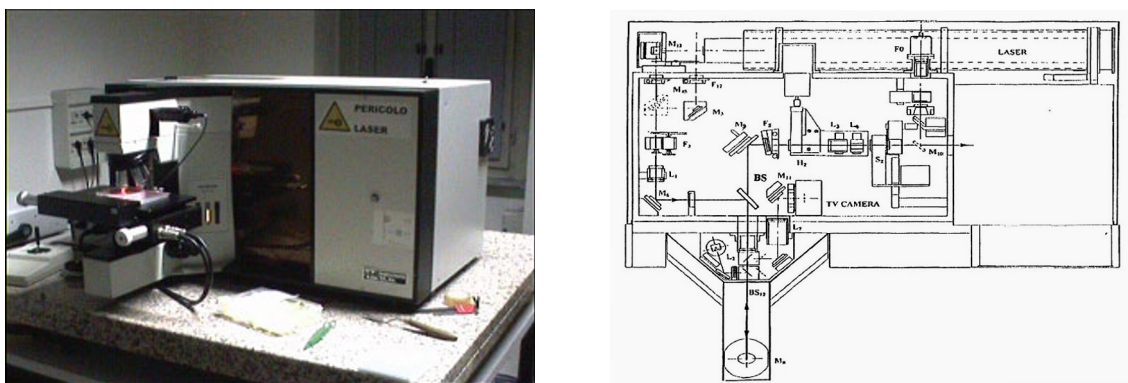

Figure 4.6.1. Left: photograph of the micro-Raman spectrometer; Right: scheme of the optical components.

The excitation radiation was provided by a He-Ne laser source (λ = 632.8 nm; 20 mW). The lateral spatial resolution is given by the beam diameter at the focal plane: spot diameter

between 10 μm and 1μm depending on the objective. The depth resolution was approximately 2 μm. Micro-Raman spectra were acquired with integration times of 30 s and 3 accumulations to enhance the signal-to-noise ratio, and all measurements were made at room temperature. The sample was mounted on the motorized x, y translation stage of the microscope, and the scattered light was measured using a backscattering geometry.

4.7. X-ray Photoelectron Spectroscopy

Some crystals of phlogopite were analysed with X-ray photoelectron spectroscopy. In the following, the theoretical and experimental fundamentals of the method used in this project will be described.

4.7.1.   Theoretical and technological considerations

Molecules and solids can be characterized by their vibrational (elastic) and electronic properties. Vibrations in molecules and solids are mostly studied by means of optical spectroscopy, that can also determine the electronic excitations. The phonon and electron excitations in solids depend on an additional quantum number, the wave vector, **k**, originating from the periodicity of the crystal solid. To perform wave-vector-dependent measurements exciting particles that can absorb or transmit, wave vectors of the same magnitude as those present in solids have to be used. Hence optical spectroscopy is not sufficient to scan the electron or phonon distributions over the whole Brillouin zone.

The phenomenon of photoemission was detected by Hertz in 1887 and explained by Einstein in 1905 invoking the quantum nature of light. Kai Siegbahn research group discovered a shift in photoelectron spectra in the late 1950s, which interpretation led to the invention of X-ray photoelectron spectroscopy (or electron spectroscopy for chemical analysis) in the early 1960s (Siegbahn 1981, Fadley 2010).

In X-ray Photoelectron Spectroscopy (XPS) a photon of energy $\hbar\omega$ liberates an electron from the sample. The energy of a core level is wave-vector-independent because of its wave function localization. The resulting spectrum will be a Lorentzian of width given by the

convolution of the lifetime width of core-hole state and the instrumental width. The interaction of the remaining photoionized system with the potential generated by the core hole will affect the charge in the valence band. The core hole potential can excite the discrete energy levels of the valence band, which appear in core-level spectrum as so-called satellites at lower kinetic energy (higher binding energy). All the photoelectron spectroscopy theories embrace the so-called sudden approximation i.e., the system response to the photohole creation is assumed instantaneous and no interaction take place between the escaping photoelectron and the remaining system.

In X-ray Photoelectron Spectroscopy the light source is an X-ray tube. The light (vector potential **A**) hits the sample and the kinetic energy, E_{kin}, and momentum **p** (wave vector **p**/$\hbar$) of the electrons excited by the photoelectric effect are measured with an electrostatic analyser (see figure 4.7.1).
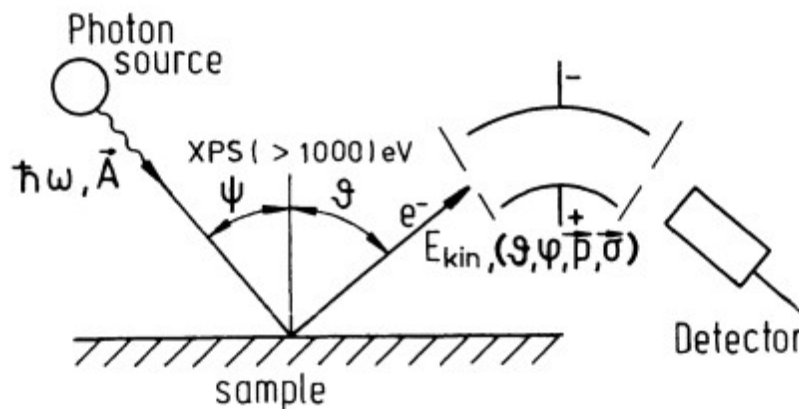

Figure 4.7.1. Scheme of a XPS experiment (modified from Hüfner 2003).

Light polarization is a useful property in angle-resolved experiments, where the kinetic energy of the photoemitted electron and its angle with the incident light ($\psi+\vartheta$) and the surface (ϑ,φ) have to be measured. ϑ and φ are the polar and azimuth angles of the electrons leaving the surface. The binding energy, E_B, of the electrons can be determined knowing the X-ray energy and the work function from the expression (Hüfner 2003):

$$E_{kin} = \hbar\omega - \phi - |E_B| \qquad (4.7.1)$$

where ω is the angular frequency of the light and ϕ the work function of the metal under study. The binding energy of an energy level in solids is generally referred to the Fermi level, whereas in free molecules or atoms to the vacuum level. The measured binding energy is not a single-particle energy, but contains many-body relaxation contributions.

The electron momentum **p** is calculated from its kinetic energy (Hüfner 2003):

$$p = \sqrt{2mE_{kin}} \qquad (4.7.2)$$

The direction of the wave vector is obtained from ϑ and φ.

Solid samples have core levels and a valence band. In metals the Fermi energy, E_F, is at the top of the valence band and has a separation ϕ from the vacuum level, E_{vac}. When a core level with binding energy E_B ($E_B=0$ at E_F) experiences photoabsorption, the photoelectrons can be detected in the vacuum with kinetic energy $E_{kin}=\hbar\omega-\phi-|E_B|$.

XPS needs Ultra-High Vacuum (UHV) conditions. The mean free path for electrons with kinetic energy between about 10 and 200 eV is of the order of a few Å, thus any solid surface spectroscopy samples only electrons from a thin surface layer. For a lot of materials the sticking coefficient, which relates to the atoms or molecules which adsorb to the surface, is much smaller than one, thus a vacuum of 10^{-10} torr is enough to perform experiments over an extended period of time. Generally speaking, the mean free path of the electrons is largely determined by electron-electron collisions, whereas electron-phonon interaction is negligible. The cross-section, σ, is given by (Hüfner 2003):

$$\frac{d^2\sigma}{d\Omega\,d\omega} = \frac{\hbar^2}{(\pi e a_0)^2} \frac{1}{q^2} \Im\left\{-\frac{1}{\varepsilon(q,\omega)}\right\} \qquad (4.7.3)$$

where ω is the energy transfer and $\hbar\mathbf{q}$ is the momentum transfer in the scattering process, $a_0=0.529$ Å (Bohr radius), Ω the solid angle into which the electrons are scattered, and $\varepsilon(\mathbf{q},\omega)$ the dielectric function. Integrating the last expression over all energy and momentum transfers, the inverse of the mean free path is obtained (Hüfner 2003):

$$\lambda^{-1} \simeq \sqrt{3} \frac{a_0 R}{E_{kin}} r_s^{3/2} \ln\left[\left(\frac{4}{9\pi}\right)^{2/3} \frac{E_{kin}}{R} r_s^2\right] \qquad (4.7.4)$$

where R=13.6 eV and r_s, the mean electron-electron distance, is measured in units of the Bohr radius a_0.

The energy of the incoming photon is higher of 1000 eV. In solids mainly wave vector-conserving transitions are excited. From energy and momentum distribution of electrons the electronic dispersion curves E(**k**) and photoionization of core levels, which energies depend on the sample chemical state, can be observed.
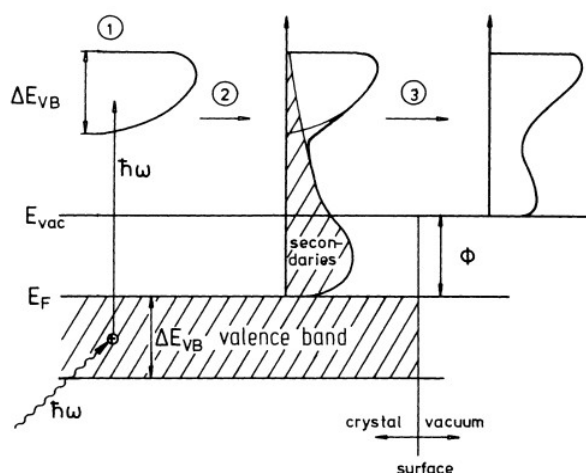

Figure 4.7.2. Three-step model: (1) photoexcitation of electrons; (2) transport to the surface with secondaries production; (3) penetration through the surface and escape into the vacuum (modified from Hüfner 2003).

A simple three-step model is used for the interpretation of XPS experiments (figure 4.7.2): (i) photoionization with the local adsorption of a photon and excitation of an electron; (ii) electrons travel through the sample to the surface with concomitant production of secondaries; (iii) electrons escape through the surface into the vacuum.

XPS is a surface-specific non-destructive analytical technique very useful to assess the chemical composition of mineral surfaces. All elements, other than H and He, can be detected when their concentrations exceed 0.1% - 1%, together with information on chemical bonding

(Seyama *et al.* 2006). This analysis can reveal differences between the surface and the bulk, and changes in composition and chemical bonding due to surface interactions.

XPS for some elements can measure both photoelectron and Auger electrons. The spectrum background arises from inelastically scattered electrons that escape to the surface from deep zones. Usually, measured photoelectron and Auger electrons have kinetic energy less than 1500 eV and an inelastic free-path of the order of nanometres.

XPS equipment comprises turbomolecular pumps, ion pumps, sublimation pumps and diffusion pumps to achieve ultra-high vacuum ($<10^{-8}$ Torr), an X-ray source with a monochromator, electron optics, an energy analyser and an electron detector.

Common X-ray sources are Al K_α (1486.6 eV) and Mg K_α (1253.6 eV). Photoelectrons energy resolution is improved by means of a monochromator that eliminates satellite spectra excited by $K_{\alpha3,4}$ and K_β. Two methods are available to analyse the electron energy: the electron deceleration by a retarding electric field, and the change of the electron orbit by an electric or magnetic field. Electric analysers employing the orbit change are the most used (e.g., the spherical deflection analyser which consists of two concentric hemispheres held at selected potentials). Often a pre-retardation stage is used prior to the energy analyser, enhancing the effective resolution of a factor of about 100 for valence band electrons. The electron energy while entering the analyser is called pass energy. After the energy analysis, the photoelectron are detected by electron multipliers.

The C $1s$ or Au $4f_{7/2}$ lines are commonly used as standard for the calibration of electron energies. However C $1s$ line of hydrocarbons, which often arises from accidental contamination by vacuum pump oil, may not be an accurate standard depending on the nature of carbon source.

Assuming that an element is homogeneously distributed in the analysed volume, XPS can perform quantitative analysis. The concentration of an element is directly proportional to the area under the corresponding peak in the photoelectron spectrum, however the peak intensity increases together with the effective sample surface area. Thus the concentration is in practice derived relatively to that of a reference element, by using relative atomic sensitivity factors that include the mean free-paths of electrons, detection efficiency of the spectrometer, anisotropy of photoelectron emission and photoionization cross-section.

As for some clay and related silicate minerals, Seyama and Soma (1985, 1988) found relative abundances of major cations (Si, Al, Mg, Fe, K, Na, etc.) of freshly prepared mineral surfaces usually corresponding to their bulk chemical compositions. However, the oxygen surface concentration exceeded the bulk value and was attributed to the presence of surface OH^- ions and/or water molecules at the surface.

XPS is capable of characterizing the bonding state of elements (chemical information) by the analysis of peak position (i.e., electron kinetic or binding energy), satellite structures and multiplet splitting. In this case, the photoelectrons binding energy and/or Auger electron kinetic energy of an element of the sample is compared with that of a reference compound. The chemical shift, that is the shift in peak (photoelectron binding energy) position, depends on the state (chemical environment) of the atom, and in particular its electron density (oxidation number), where the binding energy increases for decreasing electron density (Lindgren 2004). The shift is of the order of 0.1 eV – 10 eV and occurs from changes in the electrostatic screening felt by the core electrons as a result of the valence electron position. For instance, generally speaking, in silicate minerals spectra the Fe $2p_{3/2}$ binding energy of Fe^{3+}, about 712 eV, is higher than that of Fe^{2+}, 710 eV - 711 eV, and Fe $2p$ has satellite peaks characteristic characteristic of iron oxidation state (Seyama and Soma 1987).

In an extremely recent work, Schingaro and co-workers (2013) used electron probe microanalysys, single-crystal X-ray diffraction, micro-Fourier transform infrared spectroscopy and XPS in a multi-technique approach to study a $3T$ phlogopite polytype. XPS revealed the principal mica components (Si, Al, Mg, O and K) and their binding energies. Furthermore, the Fe oxidation state and the O^{2-}/OH^- ratio were determined, providing Fe^{3+}/Fe^{2+} equal to about 0.75 and O^{2-}/OH^- equal to 7.14.

An interesting study was conducted by Evans and Hiorns (1996) on a clinochlore and a penninite sample using angle-resolved XPS. The clinochlore composition was found to be especially non-uniform. After cleavage, the brucite-like sheet of the interlayer divided evenly between the two new complementary surfaces in the case of clinochlore, but was partitioned unequally in the penninite. The apparent composition differences between the complementary surfaces were interpreted to show a marked preference of octahedral A1 for the brucite-like sheet. In both chlorites, the layer charge was reduced in regions of easy cleavage, and a higher

presence of Si and less tetrahedral A1 than bulk chlorite was observed. X-ray photoelectron diffraction patterns revealed the low percentage of Al occupying tetrahedra sites and the absence of tetrahedral Si and Al ordering.

4.7.2.   Experimental set-up

X-ray photoelectron spectroscopy analysis were performed with a Theta Probe X-ray photoelectron spectrometer (Thermo Electron Corporation, Waltham, MA, USA) with parallel angle-resolved capability, that can work both in conventional mode, or in angular or spatial resolution. The spectrometer delivers quantitative surface and thin film analysis, small area analysis, non-destructive analysis of ultra-thin films (< 10 nm), sputter depth profiles and maps of elemental distribution, chemical state distribution, film thickness and film uniformity.

The apparatus comprises a computerized control unit for the automatic management of the main instrumental parameters, insertion procedures, samples manipulation and treatment in the analysis chamber (figure 4.7.3). A high resolution optical microscope is used for a direct monitoring of the sample. The X-ray photoelectron spectrometer is equipped with a microspot monochromatized Al K_α X-ray source (1486.6 eV). The photoelectrons are collected by an electrostatic lens which can be operated in two modes: conventional and angle-resolved mode.

Figure 4.7.3. X-ray photoelectron spectroscopy system: XPS spectrometer and control unit.

A 180° spherical sector analyser, fitted with a detector in the output plane, separates the electrons by narrow bands of kinetic energy.

The analysis were performed with a spot size of 200 μm and 50 μm, under ultra-high vacuum conditions of $5 \cdot 10^{-7}$ Pa in the analytical chamber and room temperature. Neutralization of sample charging was achieved by means of a flood gun using Ar^+ ions. Before the measurement, the investigated crystals were prepared and stored inside the pre-vacuum chamber of the XPS spectrometer for several hours for sample degassing. All spectra were acquired in Constant Analyser Energy (CAE) mode and with a take-off angle of 53°. A pass energy of 200 eV was selected for survey spectra, whereas 100 eV for high-resolution narrow spectra. The acquired spectra were energy referenced to the aliphatic component of C 1*s* signal having a binding energy of 284.8 eV.

5. *RESULTS AND DISCUSSION*

5.1. Chlorite surface properties investigations

5.1.1. Nanomorphology and crystal-chemistry

The chlorite sample was prepared and characterized at the Interdisciplinary Research Centre of Biomineralogy, Crystallography and Biomaterials of the University of Bologna (Italy). Large flat areas (10 mm x 10 mm) have been prepared by simple cleavage of the mineral. The composition was previously determined via Electron Microprobe analysis in the wavelength-dispersive mode (Valdrè *et al.* 2009), the crystal structure was also determined by using a Bruker X8-Apex fully automated four-circle diffractometer (Valdrè *et al.* 2009). The chlorite sample has an average chemical composition, determined by electron microprobe, of (wt%): MgO 33.41, TiO_2 0.06, Cr_2O_3 0.70, FeO 3.10, Fe_2O_3 0.64, Al_2O_3 18.10, SiO_2 31.13, F 0.29, H_2O 12.50. The chemical formula, normalized to a chlorite general one resulted: $(Mg_{1.701}$ $Fe^{2+}_{0.245}$ $Ti_{0.004}$ $Al_{0.998}$ $Cr^{3+}_{0.052})^{VI'}$ Mg_3^{VI} $(Si_{2.939}Al_{1.015}$ $Fe^{3+}_{0.046})^{IV}$ O_{10} $(OH_{7.913}F_{0.087})$. The sample is a clinochlore (Bayliss 1975). The VI', VI, IV refer to six-fold coordination of the octahedral interlayer cation, six-fold coordination of the 2:1 layer octahedral cation and the four-fold coordination of the tetrahedral cation, respectively. The crystal is triclinic, with the following cell parameters: a = 0.53301, b = 0.92511, c = 1.4348 nm, α = 90.420°, β = 97.509°, γ = 89.996°.

Table 5.1.1. Details on the studied clinochlore.

Chemical composition (wt%)
MgO 33.41, TiO_2 0.06, Cr_2O_3 0.70, FeO 3.10, Fe_2O_3 0.64, Al_2O_3 18.10, SiO_2 31.13, F 0.29, H_2O 12.50
Chemical formula
$(Mg_{1.701}$ $Fe^{2+}_{0.245}$ $Ti_{0.004}$ $Al_{0.998}$ $Cr^{3+}_{0.052})^{VI'}$ Mg_3^{VI} $(Si_{2.939}Al_{1.015}$ $Fe^{3+}_{0.046})^{IV}$ O_{10} $(OH_{7.913}F_{0.087})$
Unit cell parameters
a = 0.53301 nm, b = 0.92511 nm, c = 1.4348 nm, α = 90.420°, β = 97.509°, γ = 89.996°

The cleavage of chlorite gives rise to nanomorphological features which reflect the anisotropy of the physico-chemical properties of the surface.

The surface nanomorphological features were mainly of two types: (1) the stripe type (0.4-0.5 nm in height, up to several micrometers long and ranging from some nanometres to a few microns in lateral size), see figure 5.1.1a; and (2) triangular type islands or edges (0.4-0.5 nm in height), see figure 5.1.1c. These features are interpreted as a result of weak interlayer bonding along specific crystal directions and of interlayer most stable configurations, respectively. Type 1 was the most observed morphology.
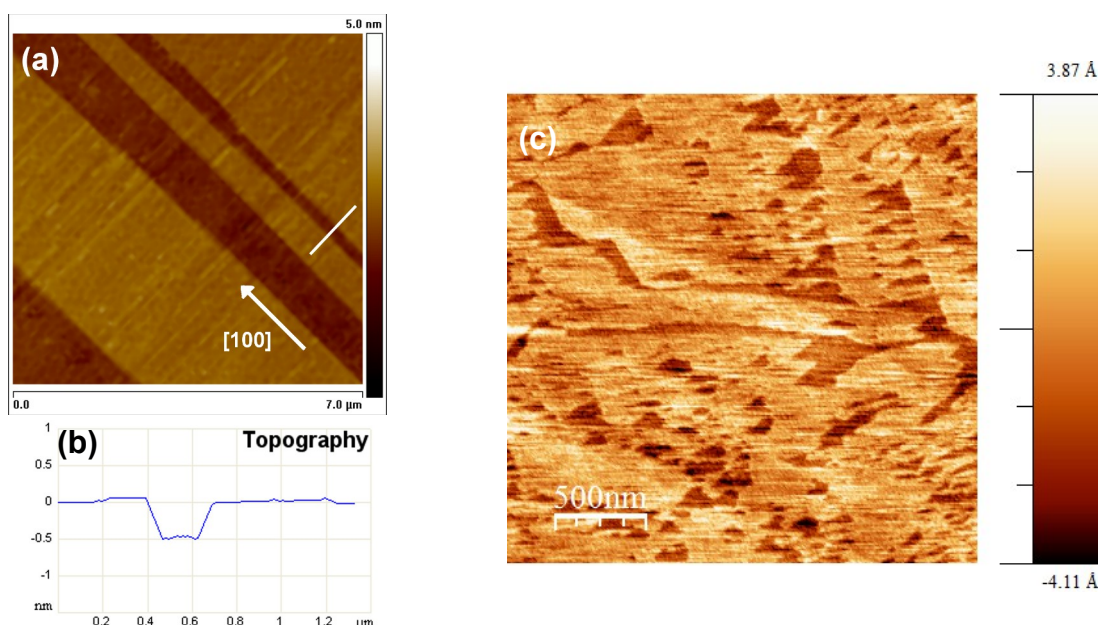

Figure 5.1.1. Typical cleavage features of chlorite resolved by AFM. (a) Stripe type morphology. (b) The topographic profile, along the white line in figure 5.1.1a, identifies two brucite-like sheets forming a channel about 0.5 nm in height and 200 nm wide. (c) Triangular type edges.

This typical morphology of near-parallel stripes, several micrometers long in the [100] crystal direction is shown in figure 5.1.1a. The figure shows bright bands, about 0.5 nm thick, of variable width corresponding to the brucite-like $Mg(OH)_2$ sheet. The darker areas of the figure correspond to the surface of the underneath TOT layer. Figure 5.1.1b reports the typical

topography profile measured across two adjacent brucite-like bands (see white segment on the right of the image). The stripe-like cleavage pattern may be explained in terms of the maximum bond density for the O-HO bonds between the octahedral interlayer and the TOT basal oxygen plane. The greatest density of TOT basal oxygen atoms occurs along the [100] direction, which in turn implies more O-HO bonds holding the interlayer sheet in place along [100]. The triangular type cleavage pattern may originate from a higher stability of triangular features due to the intrinsic octahedral structure. In details, the brucite-like sheet of the interlayer can expose to a pit octahedra presenting an exposed edge and octahedra presenting an exposed corner. Assuming one configuration to be the most stable, any pit of arbitrary shape will evolve towards a triangular shape.

The stripe-like cleavage pattern of chlorite presented also non linear edges profiles (see figure 5.1.2). Clinochlore is a layered silicate where a brucite-like positively charged octahedral sheet about 0.5 nm thick is sandwiched between two negatively charged, 1 nm thick tetrahedral-octahedral-tetrahedral (TOT) layers, by means of weak electrostatic and van der Waals forces. Figure 5.1.2 shows an example of an AFM observation of the surface of a freshly-cleaved clinochlore surface where the brucite-like sheets, B, and siloxane surface, S, of the TOT layers are visible together with the unit structure.
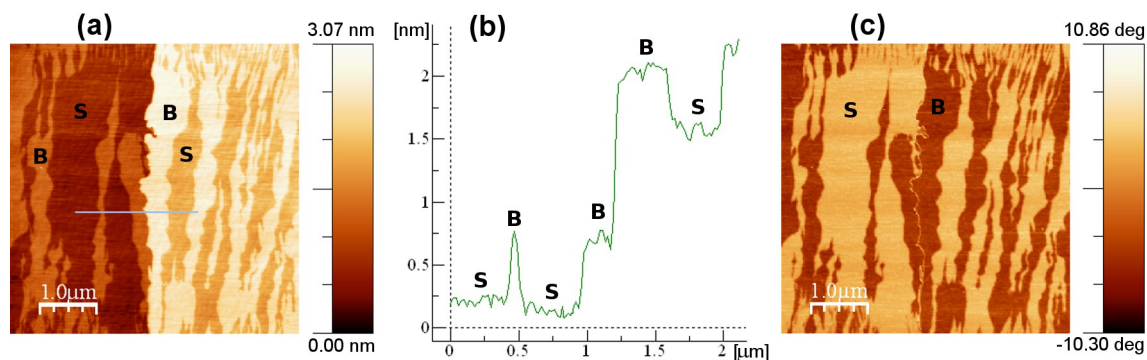

Figure 5.1.2. a) AM-AFM image of the surface nanomorphology of as-cleaved clinochlore. Brucite-like sheets (B), 0.5 nm thick, extending in width from a few nanometres to micrometres are resolved above the siloxane surface (S) of the TOT layer. b) Profile of the section along the horizontal line in the image (a). Both brucite-like and TOT layers are identified by thickness measurements. c) Phase image of the same area revealing the presence of two different materials.

The surface was imaged in air by AM-AFM (figure 5.1.2a). The section profile, figure 5.1.2b, reveals the typical surface steps related to the mineral structure. The map of the phase shift signal, ϕ, is shown in figure 5.1.2c and clearly shows the presence of the two different materials (a brucite-like sheet, B, and a siloxane surface, S).

5.1.2. Surface potential investigation

This section deals with investigations of the electric surface potential of chlorite and the correlation to the crystal structure. After a preliminary effort to develop and optimize innovative and spatially resolved methodologies based on scanning probe microscopy for the reproducible measurement of the surface potential of mineral particles (see section 4.4 for an extensive description of these methodologies), electric surface potential mapping and quantification was achieved by exploiting their high resolving capability.

Figure 5.1.3a and b show, as an example, the surface potential distribution measured by dual-pass AM-KPFM on the cleaved surface of a clorite. The crystal surface exhibits both zones with continuous and micrometrically extended remaining parts of the octahedral sheet of the interlayer, and areas where a higher fragmentation lower the local average surface potential with features not resolvable by the KPFM tip.
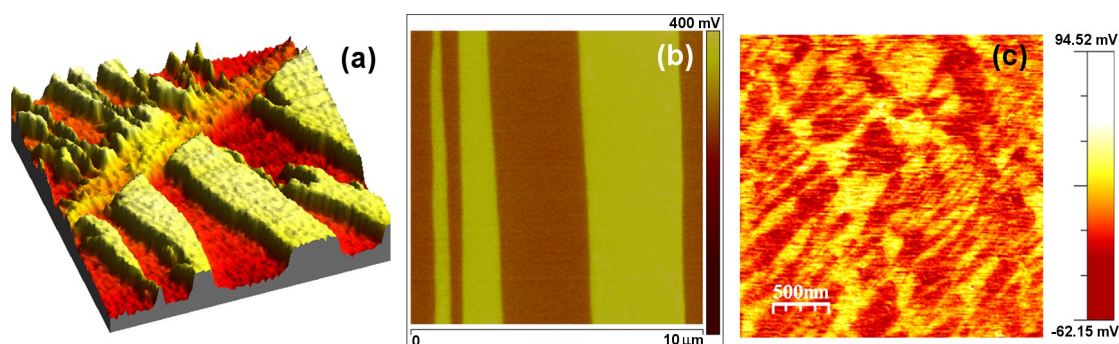

Figure 5.1.3. a) 3D, and b) 2D 10 μm x 10 μm dual-pass KPFM images of the surface potential of micrometres long brucite-like and TOT stripes on a clinochlore surface. c) 2D single pass Kelvin probe image showing the surface potential of clinochlore with details less than 25 nm in size.

The potential measurements were performed with the probe at 30 nm above the mineral surface. This operational method avoids topographical effects on the potential measurement, however limiting the spatial resolution. Figure 5.1.3c presents, as an example, a surface potential image acquired by using single-pass AM-KPFM (see section 4.4 for details about the method).

In single-pass AM-KPFM the mineral surface potential can be measured simultaneously to the topographic image of chlorite thanks to a multifrequency approach which minimises the cross-talk between the topographic and potential signals. The image reveals highly resolved surface potential features < 25 nm in size in an area with extremely fragmented interlayer sheet. A further advantage of the single-pass mode resides in an intrinsic capability of reducing electrostatic effects on the topographic signal. The simultaneous potential measurements constantly nullify the potential difference between the oscillating probe and the mineral surface thus improving the reliability of the morphological investigation that otherwise could be affected by the surface charge of the mineral.
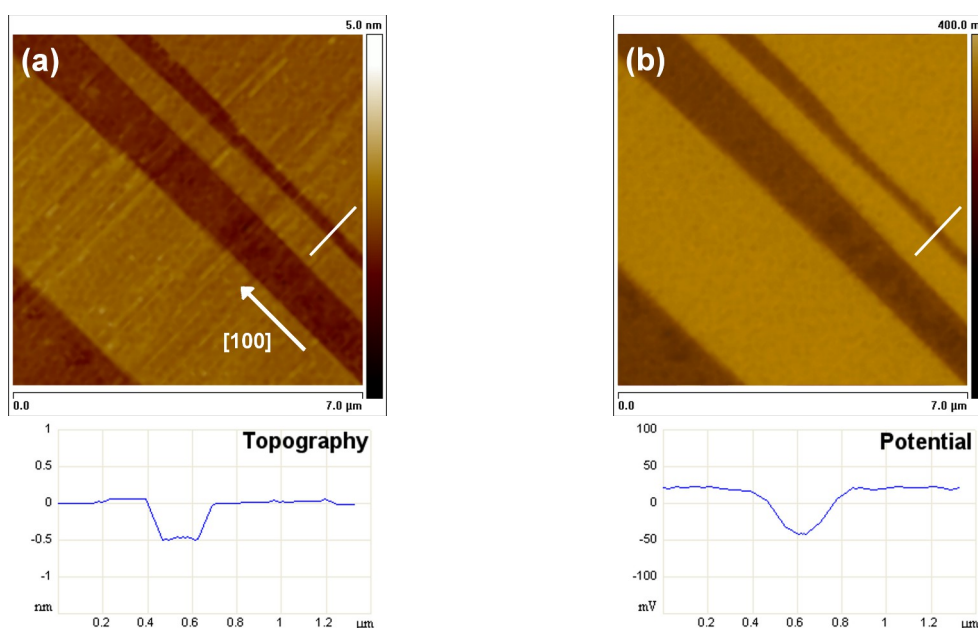

Figure 5.1.4 (a) Cleavage features of chlorite resolved by AFM. The topographic profile, along the white line in figure 5.1.4a, identifies two brucite-like sheets forming a channel about 0.5 nm in height and 200 nm wide. (b) Surface potential of the same area of figure 5.1.4a measured by Kelvin probe force microscopy.

Figure 5.1.4 shows another example where the surface potential difference between the octahedral sheet of the interlayer and the TOT surface was quantified by dual-pass AM-KPFM. The surface potential map (figure 5.1.4b) is compared with the corresponding topographic image (figure 5.1.4a).

An effective surface potential difference of about 50 mV was detected along the white line in figure 5.1.4b. Generally, for this kind of mineral the effective surface potential difference ranged from 50-100 to 400-500 mV depending on the crystal chemistry (cationic isomorphic substitutions) and relative humidity, which can form H_2O films shielding the surface potential (Sugimura *et al.* 2002).

5.1.3.   Chlorite nanolithography

Figure 5.1.5a shows a representative AFM topographic image of the (001) cleavage surface of chlorite. The brucite-like O_b sheet appears as irregular micrometer-long stripes over a darker background. A AFM profile section of some O_b sheets is recorded along the white line 1 in figure 5.1.5a and is shown in figure 5.1.5b. The O_b thickness is ~0.4 nm, in good agreement with single crystal X-Ray diffraction results (thickness = 0.3775(2) nm) (Valdrè *et al.* 2009). The direction of the stripes is along the [100] crystal direction and some parallel stripes are observed several micrometers long. The surface potential difference (ΔV) between the TOT basal plane and the O_b sheet upper surface was measured by Kelvin Probe Force Microscopy (KPFM) and Electrostatic Force Microscopy (EFM), which gave ΔV figures ranging from 50 to 500 mV (at room temperature, atmospheric pressure, and relative humidity of 30-70%) because of the variable surface crystal-chemistry and environmental conditions.

In this section it will be shown that SPM nano-lithography can be used to evaluated the strength of the single structural layers to failure and to produce custom nanopatterns.

5.1.3.1. Mechanical nanolithography

Mechanical nanolithography was carried out as shown in figure 5.1.5. The comparison of naturally occurring O_b sheet steps or terraces with the two artificially made lines (A, B) confirms the selective removal of the top O_b sheet. AFM imaging was performed in intermittent contact mode, whereas the nanolithography in contact mode was obtained with a vertical force of 0.4 nN and a speed of about 2 $\mu m \cdot s^{-1}$.
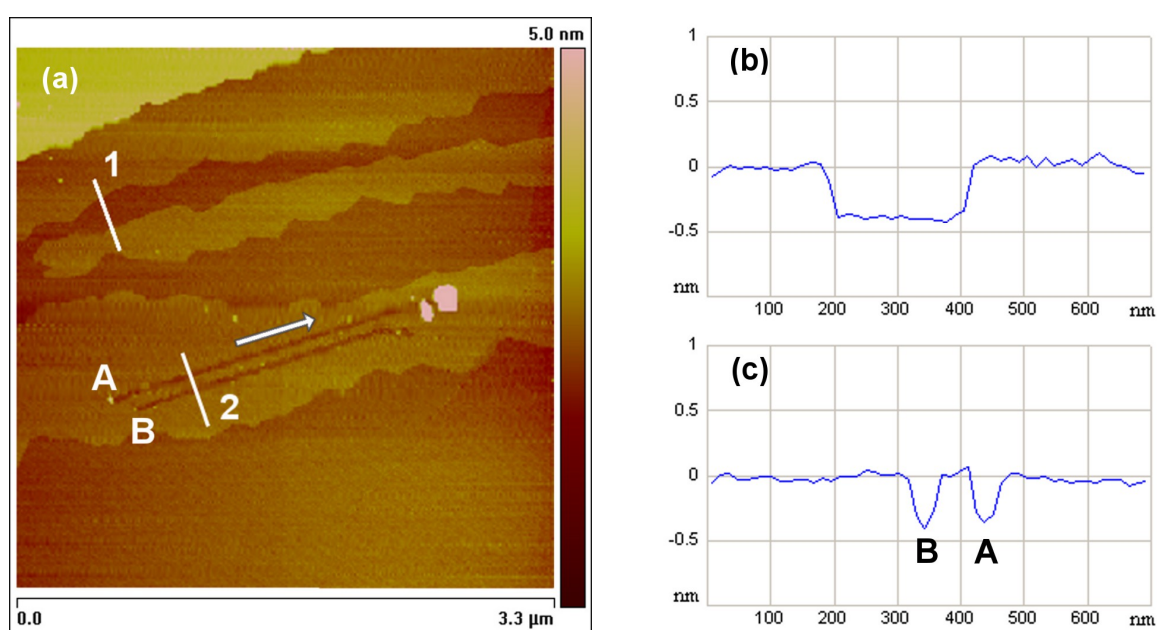

Figure 5.1.5. Mechanical nanolithography. (a) Comparison of the topography of naturally occurring $Mg_3(OH)_6$ terraces (O_b sheets) with those of two artificially nanoscratched lines A, B on the (001) cleavage surface of a chlorite. (b) Profile section of the naturally occurring terraces (O_b sheets) along the white line #1. The terraces are about 0.4 nm thick. (c) Profile section of the two nanoscratched lines A, B (white line section #2). The two scratched lines were performed in the direction indicated by the arrow. Nanolithography of the lines was performed by scratching in contact mode with the feedback on and with a force of about 0.4 nN. The width and depth of both lines are uniform. By the measure of the depths of the lines (about 0.4 nm) it results that only the O_b sheet is mechanically removed during the nanoscratching of lines.

Various SPM systems equipped with low noise electronics, closed-loop scanners and commercially available MPP-11100 cantilevers (Bruker, USA) were used for imaging and nanolithography. The depth was found not to be critically dependent on the applied force up to a few nN, whereas higher forces would produce the removal of more than 1 interlayer sheet or TOT layer. The width (30 nm) and depth (0.4 nm) of the nanolithographed features are constant within the resolution of the instrument. Some removed material was observed at the end of each line.

5.1.3.2. Voltage nanolithography

Voltage lithography was performed as shown in figure 5.1.6. In this case more complex geometries than mechanical ones can be obtained. Commercially available MESP probes (Bruker, USA) were used for voltage lithography.

Figure 5.1.6 shows images of two rhombohedra, one etched (1) and one oxidized (2) using contact mode at low force (below 0.1 nN) while applying +5V (1) and -5V (2) to the SPM tip, at a scanning speed of 10 $\mu m \cdot s^{-1}$. On the very left side of the image there are some naturally occurring steps and features due to the cleavage of the crystal.

Rhombohedron 1 has a depth of 0.4 nm, corresponding to the selective removal of the O_b sheet and a width (FWHM) of about 30 nm (see the profile section reported in figure 5.1.6b). In the case of the rhombohedron 2, the application of a negative voltage induced an anodic oxidation of the surface, creating a layer of 0.25 nm thick oxide (probably MgO and/or Al_2O_3) above the surface, with a width (FWHM) of about 40 nm, working at a relative humidity of about 40-50% (see the corresponding profile analysis of figure 5.1.6c). Depth and width were uniform and well reproducible in both patterns. Generally, voltage lithography produced less debris than mechanical lithography, making it a preferred method for etching lithography of complex geometries.
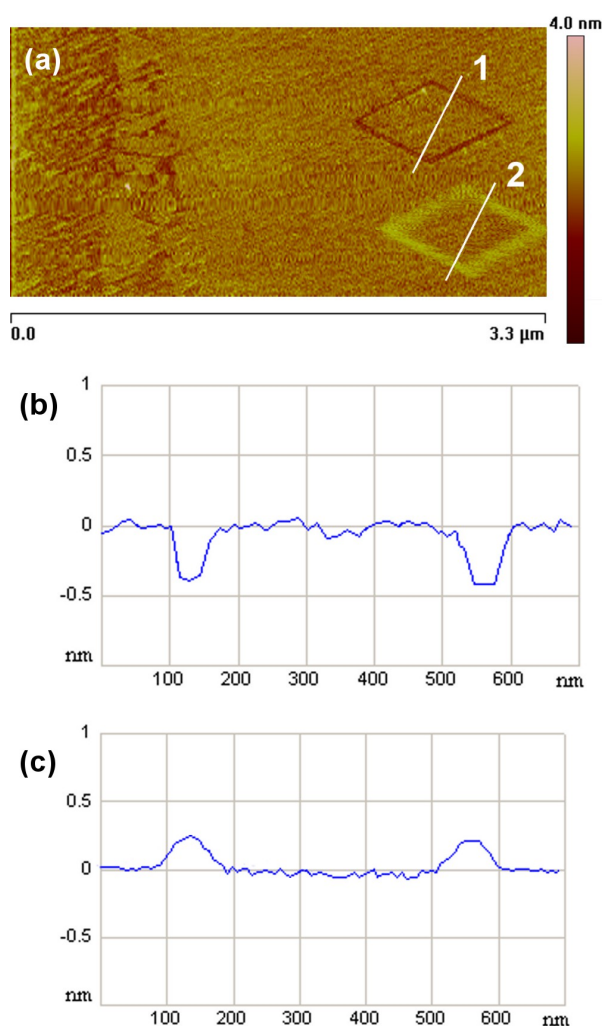
Figure 5.1.6. Voltage nanolithography. (a) Rhombohedra obtained in contact mode while applying a voltage to the SPM tip. The right-hand side of the surface is an atomic flat O_b sheet. On this surface, rhombohedron 1 was obtained applying +5 volts to the tip, whereas -5 volts were used for creating rhombohedron 2. (b) Profile section, along the white line #1, showing features of 0.4 nm in depth, corresponding to the selective removal of the O_b sheet. (c) For rhombohedron 2, the application of a negative voltage induces an oxidation (anodic oxidation) of the surface creating a layer 0.25 nm thick (profile section along the white line #2). On the left side of image (a) there are some naturally occurring steps and features due to the cleavage of the crystal.

As a summary, the suitability of this mineral for doing sub-nm depth lithography by SPM, and performing DNA nanopatterning (see section 5.2.5), resides in six important properties:

i) chlorite is easily cleavable, flat at atomic level and made-up of positive O_b sheets and negative TOT layers;

ii) the O_b sheet is only 0.4 nm thick so enabling shallow and very precise in-depth sub-nanometer lithography. The O_b sheet is weakly bonded to the strong siloxane TOT layer so that its removal can be controlled very easily without any disruption of the underneath layer;

iii) since the O_b sheet is positively charged it can be removed by application of a positive tip voltage (cathodic removal) without any mechanically applied force;

iv) the chemical composition of the O_b sheet, that is a Mg-Al-hydroxide, facilitates its oxidation by application of a negative tip voltage (anodic oxidation) enabling a controlled growth of a thin oxide layer, possibly made up of MgO and/or Al_2O_3;

v) the controlled removal of the O_b sheet on a negative siloxane TOT surface facilitates the creation of surface nanopatterning of atomic flat positive and negative areas on the same sample surface. It is possible also to remove in a controlled way several TOT-O_b units;

vi) commercial SPM tips can be used and chlorite is available in large amounts and can be prepared to have the O_b sheets or TOT layers in large areas of several mm^2.

5.2. Chlorite-biomolecules interaction studies

The present section deals with the results of the study of chlorite surface – biomolecules interaction conducted in the context of this research project. It concerns the investigation and comparison of patterned structures of single molecules of nucleotides, RNA, DNA and amino acids, created by exploiting the surface nanostructures and sub-nanometre physico-chemical properties of chlorite. The interaction between biomolecules and mineral surfaces is also of paramount importance in order to obtain information on how a biomolecule behaves at the interface with substrates and templates. The knowledge of this natural nano-technological material could also be useful in shedding some light inherently the origin of life research.

5.2.1.   Nucleotides

The simplest unit of the genetic material is the nucleotide, a molecule made up of sugars and phosphate groups joined by ester bonds. Each sugar binds one of four types of molecules called bases or nucleobases. The sequence of these bases is responsible for the main role of DNA, the long-term storage of information. These genetic instructions are used in the

development and functioning of all known living organisms, with the exception of some viruses.

Nucleotides were selected because they are the structural unit of fundamental polymers like RNA and DNA. They were deposited onto a freshly cleaved chlorite surface presenting the typical morphology of brucite-like stripes on TOT areas. The deposition was performed with a 10 µM solution (see section 4.2.1 for details). The nucleotides adsorption occurred preferentially on the positively charged brucite-like sheet (figures 5.2.1a and b). The figures show agglomerates, ordered structures and alignments of the adsorbed nucleotides. The surface nanomorphology controls the biomolecules adsorption generating complex patterns. Nucleotides preferentially adsorb on the boundary of the brucite-like sheet following its saw-toothed or triangular-shaped crystallographic profile (see for example arrow A in figure 5.2.1b). On the edges of the brucite-like sheet nucleotides line-up forming long filamentary structures (arrows B).
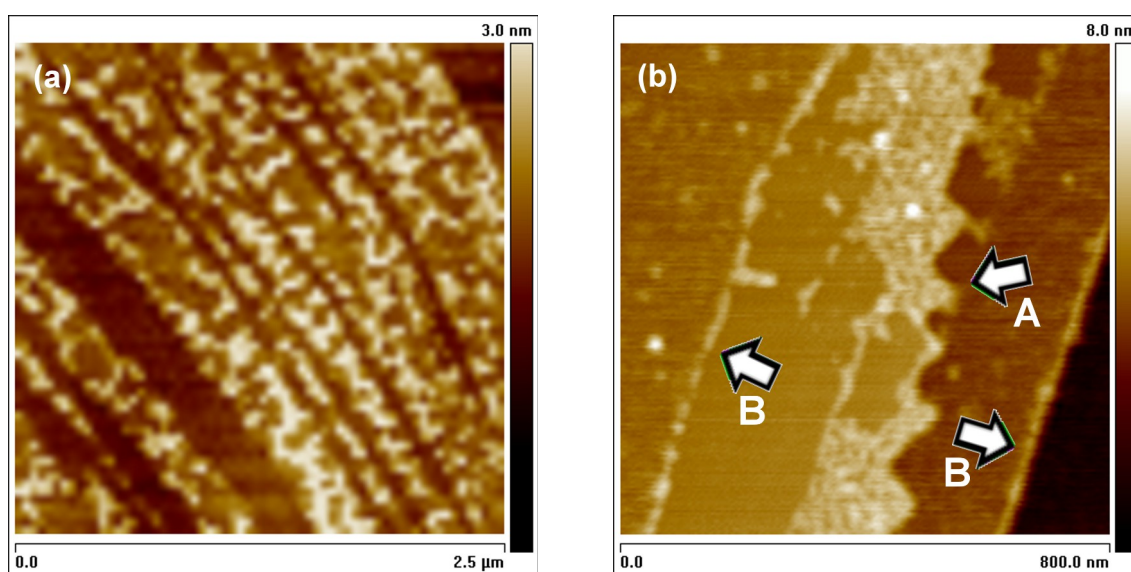

Figure 5.2.1. SPM topographic images showing the nanomorphology of a chlorite surface after cleavage and nucleotide deposition. (a) Low magnification AFM image showing nucleotides adsorption taking place only on the brucite-like surface. (b) High magnification AFM image showing that the adsorption may perfectly follow crystallographic boundaries (saw-tooth profile, arrow A). Details of single nucleotide alignments are visible at other edges (arrows B).

This result is important because in the context of catalysis it was recently shown that chlorite can lodge large amount of catalytic Brønsted-Lowry sites. These catalysts dramatically lower the activation barrier for polymerization reactions (Valdrè *et al.* 2011).

5.2.2. Ribonucleic acid

The RNA molecule is chemically similar to DNA, except for the substitution of deoxyribose (a type of ribose that lacks one oxygen atom) with the sugar ribose, and the presence of the nucleobase uracyl substituting for thymine (both have similar base-pairing properties). Also, unlike DNA, most RNA molecules are single-stranded.

The effect of the mineral surface properties on RNA adsorption are here reported. Figures 5.2.2a and b show the surface of chlorite as resolved by AFM after the deposition of RNA molecules from a 1 nM solution, at room temperature (25° C) and atmospheric pressure (see section 4.2.2 for details about the deposition method).
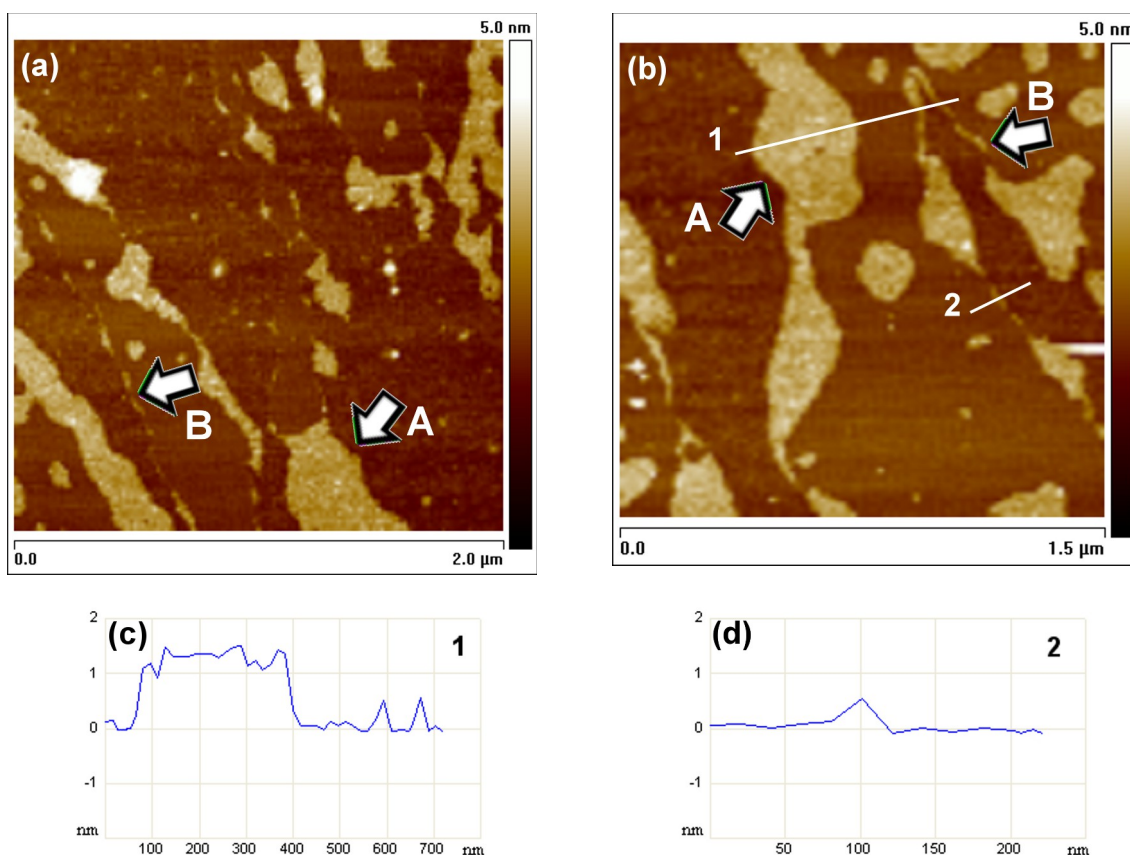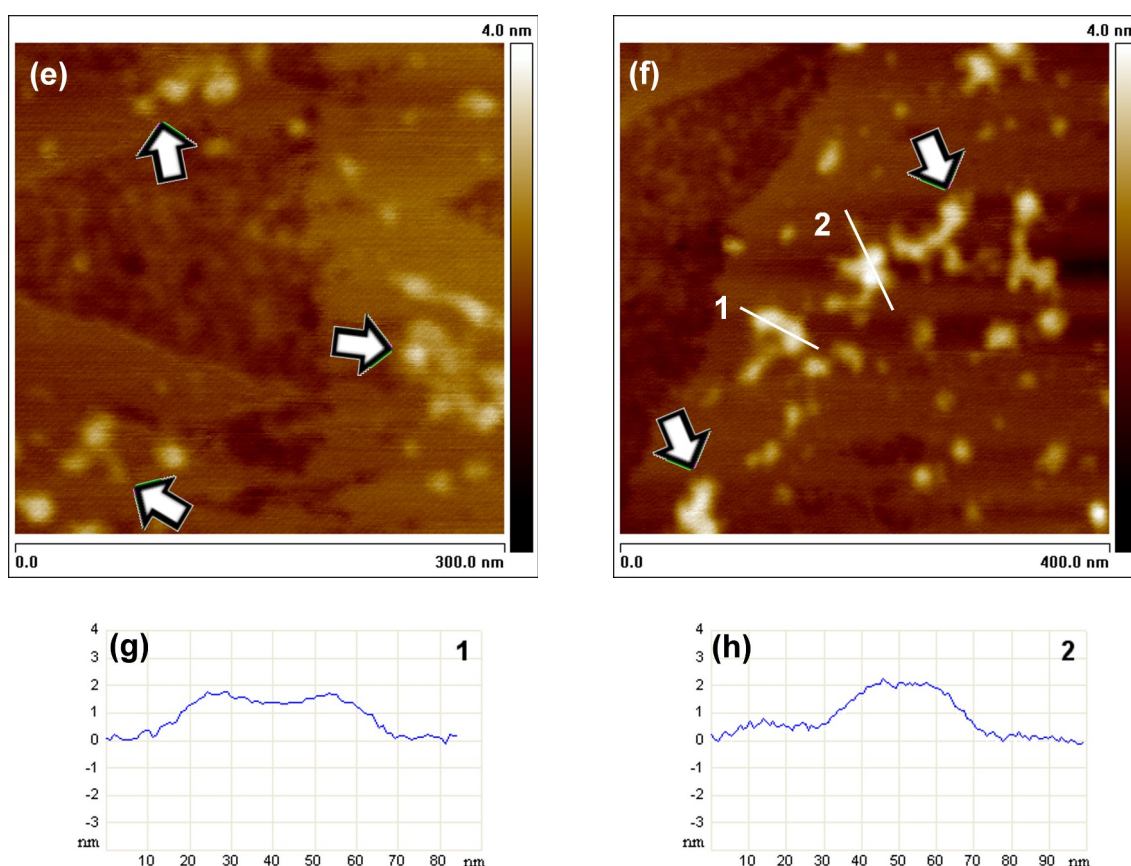
Figure 5.2.2. RNA molecules adsorbed at the surface of a chlorite. (a), (b) AFM topographic images of the deposition of RNA molecules from a 1 nM solution. Thin continuous films (bright areas, arrows A) selectively adsorb on the surface of brucite-like sheets. Aligned and linearised RNA single molecules and fragments are visible at the brucite-like sheet edges (arrows B). (c), (d) Height topographic profiles measured along the white lines 1 and 2 shown in figure 5.2.2b. (e), (f) AFM topographic images of the deposition of RNA molecules from a 0.1 nM solution. Molecules are adsorbed selectively on the brucite-like sheet and are arranged in globular domains (arrows), single or connected by linear tracts. (g), (h) Height topographic profiles measured along the white lines 1 and 2 shown in figure 5.2.2f.

Despite the inherent difficulty of dealing with an intrinsically fragile molecule that can adopt a lot of nearly isoenergetic conformations (Giro *et al.* 2004), this study shows the selective stable adsorption of RNA on the brucite-like sheet of the chlorite interlayer. The experimental evidence of the stable interlayer sheet - RNA interaction was shown by AFM. RNA molecules typically form continuous films (bright areas in the images), about 1.5 nm

thick, on the surface of the brucite-like sheet (see for example those indicated by the arrows A). In contrast, the TOT surface presents no RNA covering. Single RNA molecule alignment and linearisation were observed in correspondence with the brucite-like sheets edges, where a high electric potential gradient is present (arrows B). Figure 5.2.2c reports the height topographic profile measured along the white line 1 shown in figure 5.2.2b. The continuous film (arrow A) is about 1.5 nm thick, whereas RNA molecules aligned along an edge of a brucite-like sheet (arrow B) are about 0.5 nm thick and 20-30 nm wide.

Figure 5.2.2d reports the topographic profile measured along the white line 2 and shows the thickness of an RNA fragment of about 0.5 nm and width of 20 nm. Because of the difference in thickness between the continuous film and the single RNA filament (or fragment), I assume that the film is made up of agglomerated RNA molecules or globules (see below).

In fact, at lower RNA concentrations (0.1 nM solution) single stranded RNA molecules were observed only as agglomerates (globular domains) selectively adsorbed on the brucite-like surface.

Figure 5.2.2e and f are AFM images of the surface of chlorite after RNA deposition from the 0.1 nM solution (see section 4.2.2 for details about the deposition method). RNA molecules appear as single or multiple globules (probably corresponding to a complex of double-stranded RNA domains, not internally resolvable by SPM), sometimes separated by linear tracts of lower height (see arrows). Figures 5.2.2g and h report the topographic profile measured along the white lines 1 and 2, respectively. The RNA globules resulted of about 2 nm thick. Single globules as small as 10-20 nm in diameter were observed, furthermore some RNA molecules appear shorter than expected. The explanation of these observed features can be related to a fragmentation of the molecule occurring during the preparation procedure of the sample, or a very compact shaped configuration, as already observed to occur on another similar layer silicate (muscovite) (Giro *et al.* 2004). It is to be noted that different RNA structures can show a different compressibility to the interaction with the AFM probe.

At a low RNA solution concentration, 0.1 nM, isolated globular structures are mainly observed to be selectively adsorbed on brucite-like sheets. Increasing the concentration to 1 nM continuous films of agglomerated RNA molecules cover the brucite-like surface.

5.2.3.   Deoxyribonucleic acid

As expected, also the negatively charged long molecules of DNA develop a strong selective interaction with the chlorite surface. As previously observed, the nanoscale heterogeneity of the electrostatic layer structure of chlorite results in a mixed surface of positive and negative areas (see section 5.1.2). As shown in figures 5.2.3a and b the chlorite surface shows areas with high DNA-affinity with more than 50% coverage (only onto the positively charged brucite-like sheet) and areas where the DNA molecules are almost completely absent (negatively charged TOT surface). The brucite-like sheet forms atomically resolved edges with steps about 0.4-0.5 nm in height which give rise to high electric potential gradients. DNA molecules concentrate at the boundaries of the brucite-like zones both in network-like conformations and linear ones, following the sheet edges (see arrow A in figure 5.2.3b). Figure 5.2.3b shows also an about 2 µm wide area, of dark contrast, corresponding to a TOT surface placed between two brucite-like stripes (right and left side of the image). Several DNA molecules, bridged between the two parallel brucite-like stripes (see for example arrows B), appear in a linearised and stretched conformation. Filaments stretched for more than 2 µm long (corresponding to more than 6000 bp) were measured. In figure 5.2.3b it is possible to count at least 7 single DNA filaments in stretched conformations over an area of about 2 µm by 2 µm squared.

The DNA which is not bridged, but adsorbed on the brucite-like surfaces, is relaxed in an entangled and bundled conformation (figure 5.2.3a). As in the case of nucleotides, DNA tends to agglomerate and to order at the boundaries or edges of the brucite-like sheet (figure 5.2.3b).

DNA patterns does not show a dependence on the solution concentration probably due to the higher length of DNA single molecules in comparison to RNA ones. However, at low DNA concentration the probability to find DNA molecules in stretched configuration is reduced because of the lower amount of available molecules.
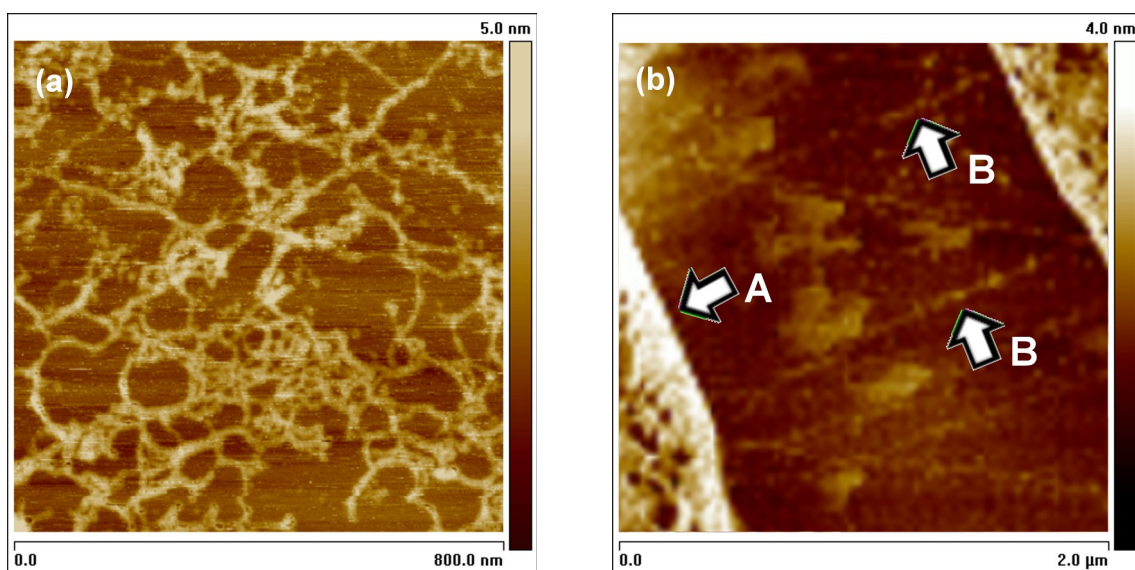
Figure 5.2.3. AFM observation of DNA molecules, about 16 μm in length, interacting with the surface of chlorite. (a) After deposition, a dense network of molecules adsorb on the brucite-like surfaces. (b) TOT surface (dark contrast area) between two brucite-like zones. High DNA surface density is observed at the edge of the brucite-like sheet (see arrow A). No relaxed DNA molecules are adsorbed onto the negatively charged TOT surface. Many DNA single filaments are instead observed above the TOT surface, bridging between the two brucite-like sheets, in a highly stretched conformation (arrows B). On the TOT surface some patches due to the salt of the solution are visible.

5.2.4.   Amino acids

The investigation on the interaction of single molecules of glycine with chlorite surface were performed by atomic force microscopy.

Topographical investigations on chlorite samples were performed to select a surface area presenting both brucite-like and siloxane zones in large amount (figure 5.2.4, left). The experiments were performed in air, at a room temperature of about 25°C, relative humidity between 45% and 55%, and standard pressure. Atomic force microscopy observations were conducted in amplitude modulated intermittent contact mode (see section 4.3.1 for details). A 150 μM solution of glycine was deposited on the selected chlorite surface (see section 4.2.4 for details about the deposition process). Figure 5.2.4 shows on the left a freshly cleaved

chlorite surface with brucite-like stripes from about 600 nm to 30 nm in width. On the right the same surface area was observed after the deposition of glycine molecules. A selective affinity with the brucite-like surface was observed, whereas no glycine molecules adsorbed onto the siloxane surface. Also brucite-like stripes < 30 nm in width were observed to stably adsorb glycine.

Figure 5.2.5 reports on the left an AFM topographic image of about 450 nm x 450 nm of an exposed siloxane surface between two brucite-like stripes. On the right the corresponding phase signal image acquired simultaneously to the topographic one (see section 4.3.1 for an explanation on the nature of the phase image). The phase image which is highly material-dependent clearly distinguishes the siloxane surface, the brucite-like one and glycine molecules by a different contrast. Furthermore, the phase image gives more details, resolving fine structures inside the glycine monolayer.
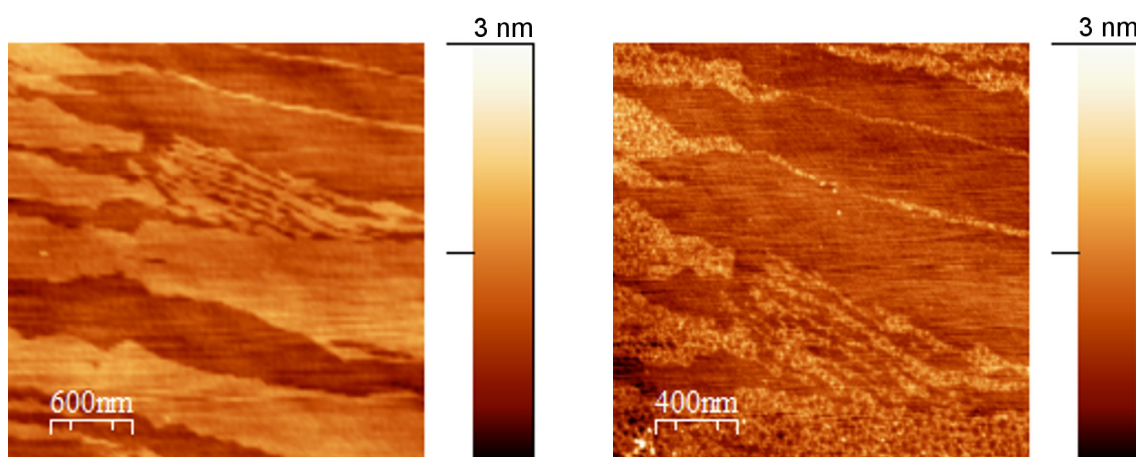

Figure 5.2.4. Left: AFM image of the morphology of a freshly cleaved chlorite surface area selected for the deposition of molecules of glycine. Right: AFM topographic image of the same surface area of the image at right side after the deposition of a 150 µM solution of glycine.
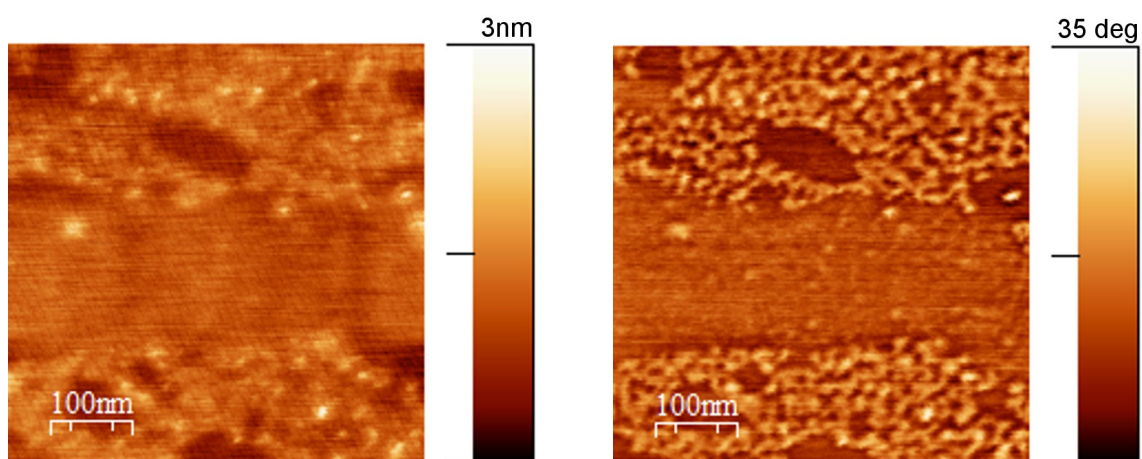
Figure 5.2.5. Left: AFM topographic image of glycine molecules adsorbed on a chlorite surface. Right: AFM phase image of the same area as in the left image, simultaneously acquired.

Figure 5.2.6 reports a highly detailed AFM topographic (left) and phase (right) image. Small dot-like conformations are resolved. These structures align along the edges of the brucite-like stripes, whereas a not uniform distribution is observed inside the brucite-like surface. Indeed, both areas with high concentration of molecules and areas without any adsorbed molecule are present on the brucite-like surfaces.
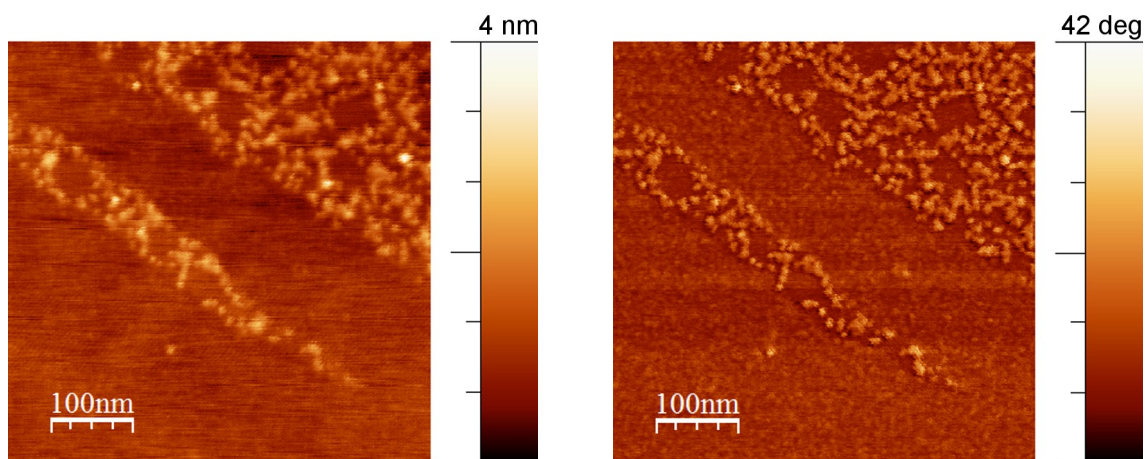

Figure 5.2.6. Left: AFM topographic image of glycine molecules adsorbed on the brucite-like interlayer sheet of a chlorite. Right: AFM phase image acquired simultaneously to the topographic one on the left.

Thanks to the high affinity with the brucite-like surface single molecules of glycine were isolated and measured (figure 5.2.7). Glycine molecules are stably bounded to the surface of the brucite-like sheet of the chlorite interlayer by van der Waals and weak electrostatic forces. Figure 5.2.7 reports high resolution images of a surface area of about 80 nm x 80 nm. In particular, in the phase image (in the middle) the brucite-like surface (dark contrast), the siloxane surface (middle tone contrast) and glycine molecules (bright contrast) are visible. Some molecules align along the edge of the brucite-like surface (on the upper left part). A profile section (on the right) performed along the line drawn on the topographic image allowed to verify the single molecule nature of the dot-like structure, that is about 1 nm in height and 9.6 nm wide. It is to be noted that the overestimated width of the molecule is due to the convolution with the high radius of curvature of the AFM tip (about 10 nm). This is a well known effect.
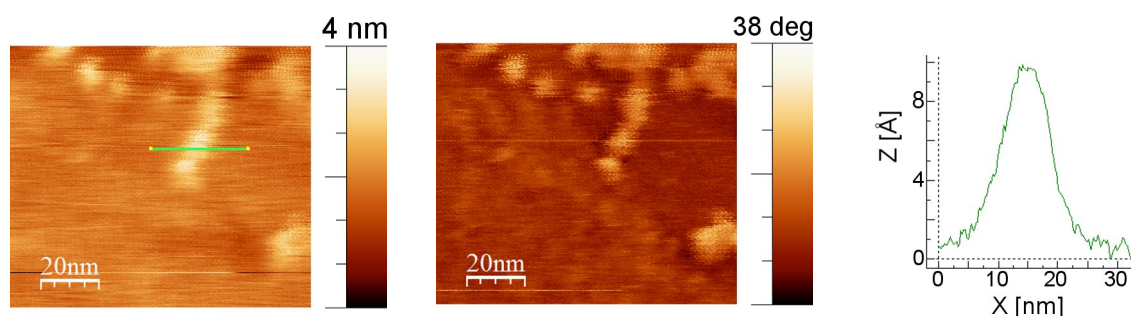
Figure 5.2.7. Left: AFM topographic image of single molecules of glycine adsorbed on the surface of the brucite-like interlayer sheet of chlorite. Middle: AFM phase image of the same zone as in the left image where single molecule of glycine, the TOT surface and the brucite-like surface can be distinguished. Right: topographic profile section, along the line shown in the left topographic image, of a single glycine molecule. The full width at half maximum is 9.6 nm.

5.2.5.   Bio-nanopatterning

Bio-nanopatterning of surfaces is becoming a crucial technique with applications ranging from molecular and cell biology to medicine. Scanning probe microscopy is one of the most useful tools for nanopatterning of flat surfaces. However, these patterns are usually built on homogeneous surfaces and require chemical functionalization to ensure specific affinity. It has been shown in section 5.2.3 of this thesis that chlorite surface have unique self-assembly properties on DNA molecules, due to its peculiar crystal chemistry based on alternating positive and negative crystal structures. However, patterns on these surfaces tend to be randomly organized. In the present section it will be shown the nanolithography of chlorite surface by means of a SPM tip to construct an atomically flat charged pattern, designed to guide DNA deposition along predetermined directions without need of any chemical functionalization of the surface.

Bio-nanopatterning of substrates has multiple applications in bio-chips, nano-arrays fabrication and bio-sensors technology (Mendes *et al.* 2007). In particular, the use of bio-chips for drug screening, DNA nano-arrays for gene expression and protein nano-arrays for medical applications is attracting more and more interest from the scientific and the technology communities.

One of the most stringent requirement in bio-nanopatterning is the ability to confine the deposition of the relevant biomolecules exclusively onto specific nano-areas of the substrate. These areas should be reasonably flat, homogeneous and chemically stable. The most common ways of patterning surfaces make use of self assembly of molecules combined with nanolithography (see section 5.1.3 for details about nanolithography). SPM can be used to perform nanolithography and also to characterize the bio-chip by imaging its surface. Bio-nanopatterning can be obtained by creating nano-areas with a specific chemical affinity onto an inert and uniform surface. In a second stage the required molecules will be deposited on the surfaces and will bind specifically on the patterned areas. A patterned surface, ready to accept biomolecules, is therefore a multifunctional surface. The stability and the accuracy of the geometrical and functional pattern are essential for the reliability of the bio-device.

It has been shown that chlorite surface potential anisotropy drives the local deposition of charged biomolecules. Freshly cleaved chlorite surfaces are stable multi-functional materials

presenting areas with two opposite potentials: the brucite-like positive O_b sheet and a TOT negative layer. In summary, DNA molecules were observed to deposit exclusively onto O_b sheets with nanometre accuracy (see section 5.2.3). It has also been shown that an exposed O_b sheet has a much higher affinity than TOT with respect to the adsorption and self-assembling of biomolecules such as, nucleotides (section 5.2.1), RNA (section 5.2.2), DNA (section 5.2.3) and amino acids (section 5.2.4). Furthermore, DNA molecules were observed in stretched conformation bridging O_b sheets above negative TOT regions. The deposition and stretching mechanisms are driven by differences in the surface potential between these two types of areas on the surface. This bi-functional behaviour of chlorite is highly stable as it is an intrinsic property of the crystal and does not require external chemical modification. Differently from conventional bio-patterning, chlorite surface bi-function is not limited to the local charge distribution, but it could encompass several other physical properties of the O_b sheets and TOT regions. For this reason chlorite is a very interesting surface for bio-patterning and it could simultaneously address charge, hydrophobicity, friction and roughness properties of biomolecules. In addition, the well characterized crystal structure of this layer mineral can be used as a sub-nanometre height calibration to quantify dimensions and conformation of the deposited molecules.

However, the O_b areas on the surface are randomly distributed and do not provide geometrically controlled and reproducible patterns as required by bio-nanopatterning applications. Here it will be shown that using SPM nanolithography it is possible to fabricate stable, reproducible and geometrically accurate multifunctional patterns on chlorite.

This novel method is shown through applicative examples of specific bio-nanopatterning and stretching of DNA molecules.

Figure 5.2.8a shows an O_b surface where a vertical stripe about 500 nm wide has been etched by a +5V voltage lithography revealing the underlying negative TOT layer (dark band). Figure 5.2.8d shows the height profile analysis along the white line shown in figure 5.2.8a, where steps of 0.4-0.5 nm are visible. The removal of the O_b sheet was obtained in about 5s by voltage lithography.

Figure 5.2.8b shows that the surface potential difference between the O_b and TOT surface is around 100 mV in agreement with previous measurements (see section 5.1.2). It is worth noticing that KPFM and morphology characterization can be performed with the same probe used for the voltage lithography simplifying the overall process. Figure 5.2.8e reports the surface potential profile along the white line of figure 5.2.8b.

A linear double-stranded λ-DNA of 48,502 base-pair length was deposited onto this patterned surface and the result is shown in figure 5.2.8c. The DNA deposition procedure is the following: first the DNA, diluted in a K-glutamate buffer, 10 mM Tris HCl, and 1 mM EDTA as is commonly used for type-III restriction endonuclease (Fermentas Life Sciences, USA), was brought to a 1 nM final DNA concentration, at pH 7.6, in an ultra-pure water solution (Gibco, USA; Ultra-pure water DNAse, RNAse free). Before nanolithography, the chlorite surfaces under investigation were sterilized by a quartz sterilizer apparatus. Then each surface was characterized morphologically, to the nano-scale level, by AFM and assessed to be free of contamination. After nanolithography a 20 μl drop of the DNA dilution was deposited on the surface. The samples were incubated for about 5 min in a water vapor-saturated environment, rinsed gently, washed for 30 s with ultra-pure water, and dried with an ultra-pure N_2 flow.

The negatively charged DNA molecules adsorbed onto the positive O_b areas rather than onto the negative TOT surface, confirming what was already observed on naturally occurring O_b channels. Figure 5.2.8c shows a DNA coverage of about 50% onto the O_b surfaces. Figure 5.2.8f shows the height profile analysis along the white line shown in figure 5.2.8c. Single DNA filaments were induced to "bridge" (see arrows) between the two positively charged surfaces with a linear density of more than five DNA parallel filaments per micron.

Differently from the previously reported stretched molecules, here the size of the channel is constant and the molecules arrange in an almost parallel fashion confirming the ability of this artificial pattern to manipulate DNA conformation. Previous measurements have shown that the interaction between these stretched molecules and the underlying TOT surface is weak. This aspect could be exploited for the study of DNA-enzyme interactions as it should allow the full access to the molecule.
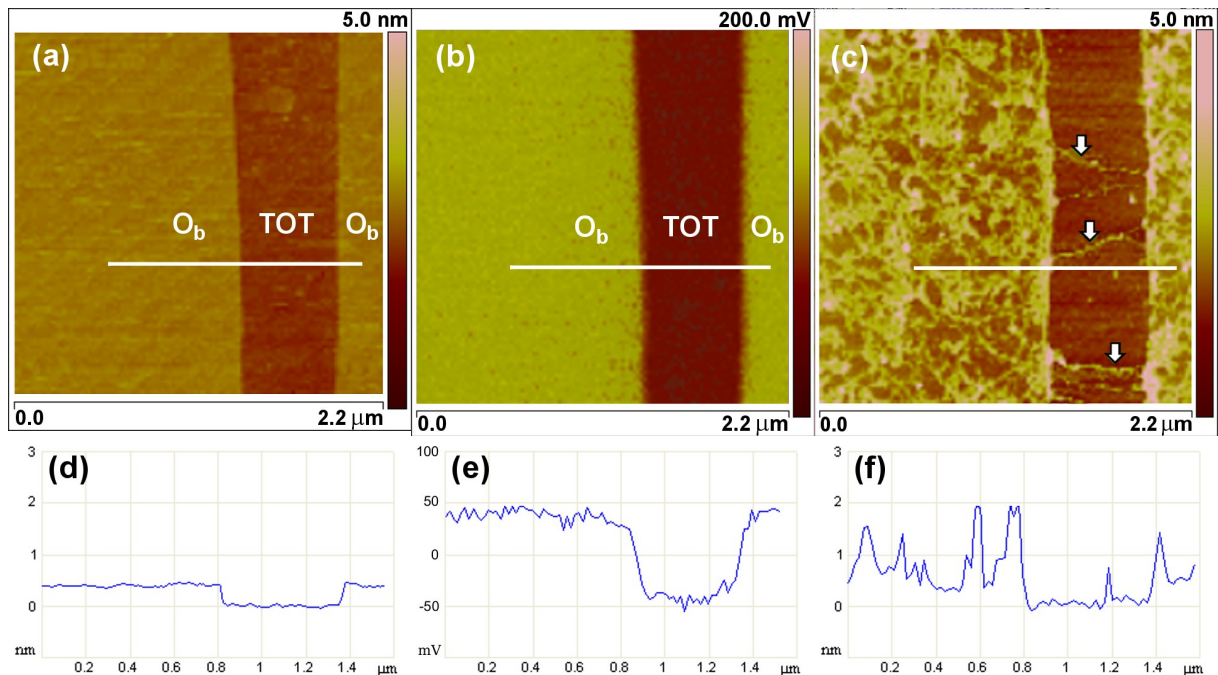
Figure 5.2.8. Example of DNA bio-nanopatterning method. DNA molecules selectively adsorbed and stretched on a nanolithographed chlorite surface. (a) AFM topography of the surface where a stripe about 500 nm in width and 0.4 nm in depth has been obtained by controlled removal of the O_b sheet by SPM voltage lithography by applying +5V to the tip. The underneath TOT surface appears as a vertical dark band. (b) Surface potential image (KPFM) of the same area as in (a) confirming that the TOT surface is negative, whereas the O_b sheet surface is positive. (c) DNA molecules deposited onto the SPM nanopatterned surface. The negatively charged long molecules of DNA deposit preferentially onto the positive O_b sheet rather than onto the negative TOT surface. DNA "bridging" (see arrows) between the two O_b sheets (about 0.5 μm distance apart) is induced. (d) Height profile analysis along the white line shown in figure 5.2.8a. (e) Surface potential profile along the white line of figure 5.2.8b. (f) Height profile analysis along the white line shown in figure 5.2.8c. The ΔV voltage difference between the O_b sheet and TOT surface is about 100 mV.

In figure 5.2.8c the stretched DNA molecules are randomly anchored along the step edge but a specific pattern of the step edge could determine the anchoring points. In particular, edges forming corners are preferential binding points for DNA molecules. Figure 5.2.9 shows

that, it is possible to pattern the O_b sheet to produce artificial corners and, in this way, guide the DNA molecules to stretch between specific points on the surface. In figure 5.2.9 naturally occurring and horizontally oriented O_b sheets were orthogonally nanolithographied (removed) creating gaps and corners between the remaining parts of the O_b sheet. One can in fact observe in figure 5.2.9 that stretched DNA molecules are preferentially anchored in the vicinity of the fabricated step corners. This technological development is a milestone towards single molecule manipulation that does not require any external intervention, but it is only surface driven.
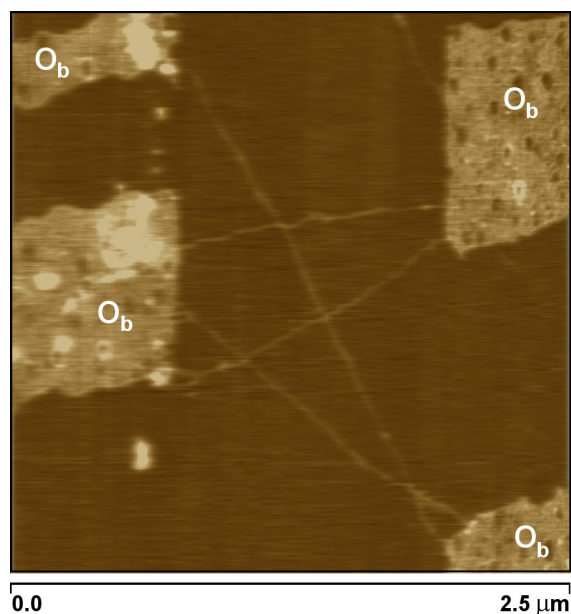

Figure 5.2.9. Stretched DNA molecules between corners of nanolithographed chlorite surface. The stretched DNA molecules are preferentially anchored at the corners of the brucite-like O_b regions. Some DNA molecules (brighter areas) are agglomerated and adsorbed on the top of the brucite-like O_b surface. Overall height of the image is 5 nm.

5.3. Phlogopite surface properties

5.3.1.   Nanomorphology, crystal-chemistry and surface potential

The structure and crystal-chemistry of six phlogopite crystals were initially explored by electron probe microanalysis and single crystal X-ray diffraction from the research group of Prof. Scordari at the Earth and Geoenvironmental Sciences Department of the University of Bari (Lacalamita *et al.* 2012). All the crystals were coexisting in the same rock sample.

Two samples occurred as $1M$ polytypes, whereas the remaining fourth as $2M_1$ polytypes.

Table 5.3.1 reports the structural formulae derived for the six analysed samples, showing the occupancies of the interlayer site, the octahedral site, the tetrahedral site and the anionic site.

Table 5.3.1. Structural formulae of phlogopite samples.

	Interlayer site	Octahedral site	Tetrahedral site	Anionic site
$1M$ Polytype				
BU1_2	$(K_{0.91}Na_{0.04}Ba_{0.01})_{\Sigma=0.96}$	$(Mg_{2.36}Al_{0.03}Fe^{2+}_{0.20}Fe^{3+}_{0.08}Ti_{0.26}Cr_{0.06}Ni_{0.01})_{\Sigma=3.00}$	$(Si_{2.86}Al_{1.07}Fe^{3+}_{0.07})_{\Sigma=4.00}$	$O_{10.51}F_{0.12}OH_{1.37}$
BU1_7	$(K_{0.90}Na_{0.05}Ba_{0.01})_{\Sigma=0.96}$	$(Mg_{2.34}Al_{0.08}Fe^{2+}_{0.20}Fe^{3+}_{0.08}Ti_{0.26}Cr_{0.05})_{\Sigma=3.01}$	$(Si_{2.87}Al_{1.07}Fe^{3+}_{0.06})_{\Sigma=4.00}$	$O_{10.58}F_{0.10}OH_{1.32}$
$2M_1$ Polytype				
BU1_8	$(K_{0.96}Na_{0.03}Ba_{0.01})_{\Sigma=1.00}$	$(Mg_{2.27}Al_{0.08}Fe^{2+}_{0.21}Fe^{3+}_{0.08}Ti_{0.29}Cr_{0.06}Ni_{0.01})_{\Sigma=3.00}$	$(Si_{2.90}Al_{1.03}Fe^{3+}_{0.07})_{\Sigma=4.00}$	$O_{10.71}F_{0.04}OH_{1.25}$
BU1_14	$(K_{0.96}Na_{0.04}Ba_{0.01})_{\Sigma=1.01}$	$(Mg_{2.29}Al_{0.09}Fe^{2+}_{0.21}Fe^{3+}_{0.08}Ti_{0.28}Cr_{0.04}Ni_{0.01})_{\Sigma=3.00}$	$(Si_{2.87}Al_{1.06}Fe^{3+}_{0.07})_{\Sigma=4.00}$	$O_{10.65}F_{0.05}OH_{1.30}$
BU1_15	$(K_{0.95}Na_{0.04}Ba_{0.01})_{\Sigma=1.00}$	$(Mg_{2.29}Al_{0.10}Fe^{2+}_{0.21}Fe^{3+}_{0.08}Ti_{0.27}Cr_{0.04}Ni_{0.01})_{\Sigma=3.00}$	$(Si_{2.90}Al_{1.03}Fe^{3+}_{0.07})_{\Sigma=4.00}$	$O_{10.66}F_{0.05}OH_{1.29}$
BU1_17	$(K_{0.96}Na_{0.04}Ba_{0.01})_{\Sigma=1.01}$	$(Mg_{2.29}Al_{0.09}Fe^{2+}_{0.21}Fe^{3+}_{0.08}Ti_{0.28}Cr_{0.04}Ni_{0.01})_{\Sigma=3.00}$	$(Si_{2.87}Al_{1.06}Fe^{3+}_{0.07})_{\Sigma=4.00}$	$O_{10.65}F_{0.05}OH_{1.30}$

The crystals BU1_7, BU1_15 and BU1_17 were selected as representative of the samples population to investigate the surface nanomorphology, electric potential and chemistry.

The surface nanomorphology was investigated by atomic force microscopy. NP-type AFM probes (Bruker) were selected to be used for contact-mode measurements. This type of probe is made of silicon nitride. A single chip brings four triangular shaped cantilevers with different force constants, from 0.58 N/m to 0.06 N/m. The tip has a radius of curvature of

about 20 nm. EFM-type (Nanoworld) and MPP-11100 (Bruker Co., Camarillo, CA, USA) probes were used for intermittent contact-mode. EFM-type of probe has a nominal radius of curvature of about 25 nm. The Pt-Ir coated rectangular cantilever has a nominal working frequency 75 kHz, k = 2.8 N·m^{-1}, cantilever length 225 μm. MPP-11100 probe has a nominal radius of curvature of about 10 nm. The uncoated rectangular cantilever has a nominal working frequency 300 kHz, k=40 N·m^{-1}, cantilever length 125 μm.

All the experiments were performed in air, at room temperature between 19°C and 24°C, relative humidity between 36% and 47%, and standard pressure.

The selected phlogopite samples were prepared for the atomic force microscopy investigations. The crystals were fixed onto AFM specimen discs with double-sided tape and cleaved. Only the unequivocally cleaved portion of the crystals were investigated.
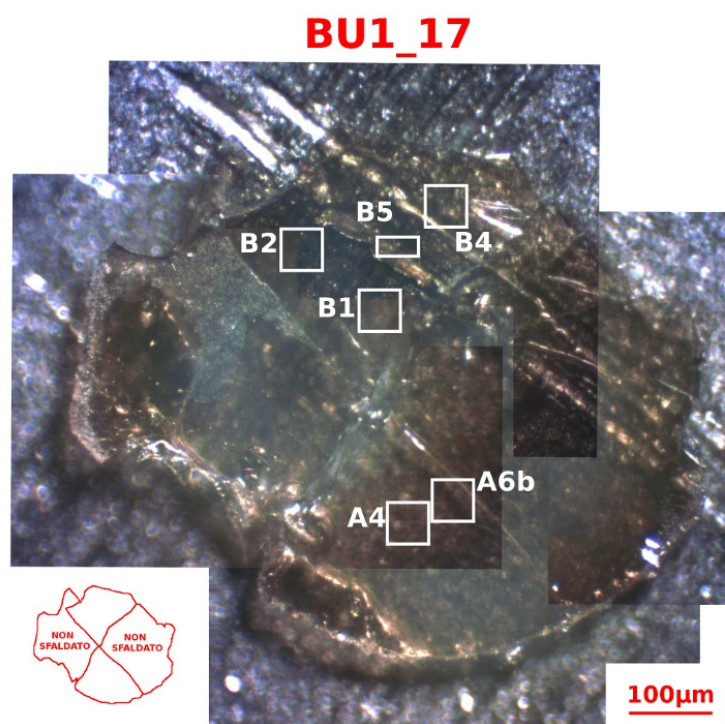

Figure 5.3.1. Composite photograph of the BU1_17 phlogopite sample. Square frames indicate the investigated areas. The inset shows the cleaved areas that were analysed by AFM, KPFM, micro-Raman spectroscopy and XPS.

Figure 5.3.1 shows a composite photograph of the crystal BU1_17. The crystal has lateral dimensions of about 700 μm x 600 μm. White square frames indicate the investigated areas.

Optical images of the crystals BU1_7 and BU1_15, together with the indications of the areas investigated, are available in figure 5.3.10 and 5.3.11, respectively.

Phlogopite (001) surface was observed to present atomically flat areas extended for more than 50 μm x 50 μm. RMS roughness analysis gave values under the z position noise of the piezoelectric scanner (0.1 nm).

Cleavage edges were observed at the (001) surface, with steps height minor than 380 nm. The typical height of cleavage steps was minor than 50 nm. Sometimes steps of 1 nm were also measured corresponding to a single TOT layer. The left image of figure 5.3.2 shows an atomic force microscopy (AFM) topographic image of curved nanometric cleavage features at the (001) phlogopite surface. In the right image of figure 5.3.2 a profile section along the line drawn in the AFM topographic left image shows a height for each of the three top steps of about 1 nm, corresponding to single TOT layers.
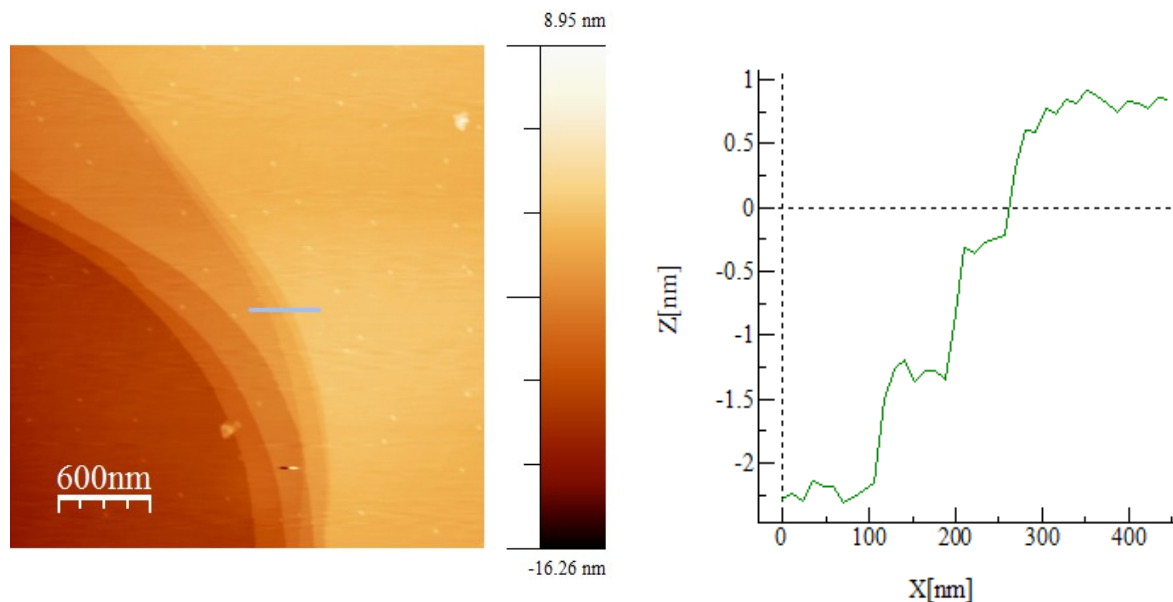

Figure 5.3.2. Left: AFM topographic image of a phlogopite surface showing single TOT layer cleavage planes presenting a high radius of curvature. Right: profile section along the line drawn in the topographic image where single TOT layers of about 1 nm are measured.

In general, the profile of the edges was never observed jagged, but mainly as perfectly straight lines extending for tens of micrometers or slightly curved ones. Furthermore, highly curved edges were also observed (with radius of curvature of less than 2 μm; see figure 5.3.2).

Figure 5.3.3 shows a cleavage feature that suggests a conchoidal form of cleavage not related to a crystallographic direction.

Together with the morphological analysis, the phase signal was investigated while imaging in intermittent contact mode. The phase signal may be qualitatively related to various material-based properties such as, composition, adhesion, friction, visco-elasticity and also the surface potential. Phase signal analysis didn't revealed inhomogeneities.

705.05 nm

-292.07 nm
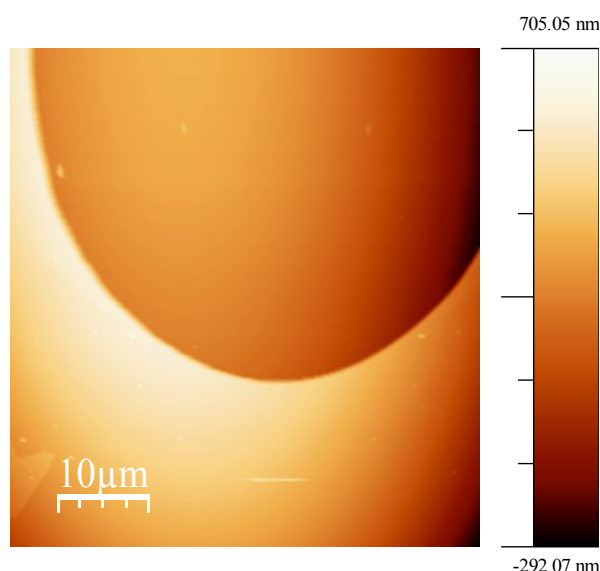
Figure 5.3.3. AFM topographic image of a freshly cleaved phlogopite surface revealing a conchoidal cleavage.

The steps composed of multiple layers were observed both appearing at the AFM measurement as a perfect single-step ledge or as a stepped ledge.

Figure 5.3.4 reports on the left an AFM topographic image of a linear cleavage feature. At the profile section shown in the right image, the step appears as a single-step ledge of about 55 nm.

Figure 5.3.5 shows on the left an AFM topographic image of a typical stepped ledge. The image in the middle is a map of the amplitude signal. It is related to the error of the feedback control system in maintaining an imposed constant oscillation amplitude. Therefore, it highlights the edges of the surface structures and in this case the surface steps. The image on

the right of figure 5.3.5 reports the profile of the stepped ledge. On the top four steps of about 7 nm are resolved, whereas at the bottom the AFM tip can not resolve the single steps.
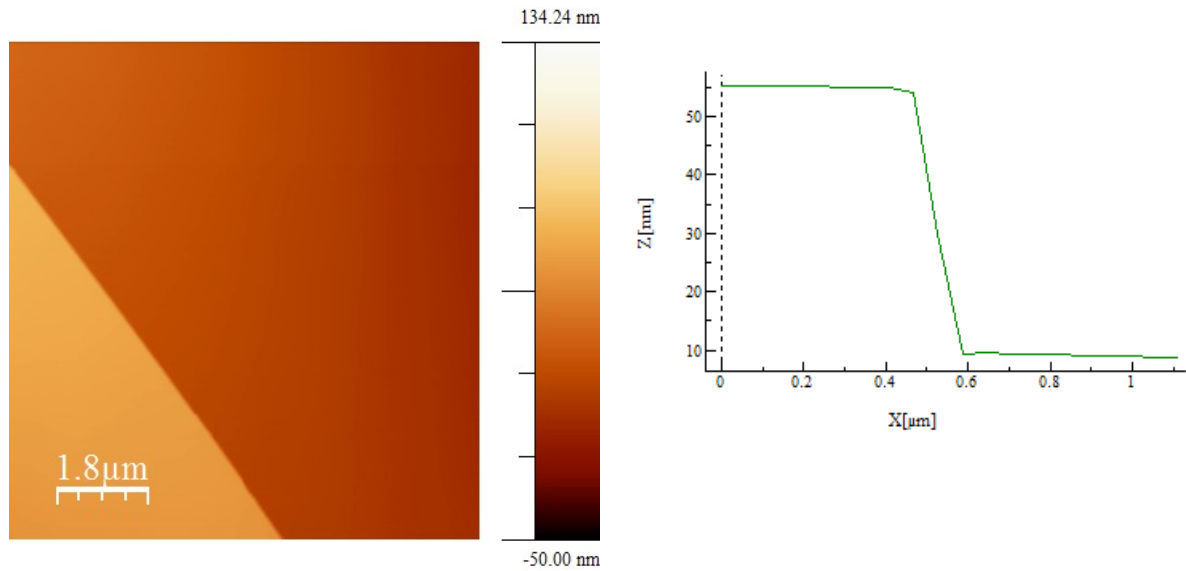
Figure 5.3.4. Left: single-step ledge. Right: Profile section of the single-step ledge.
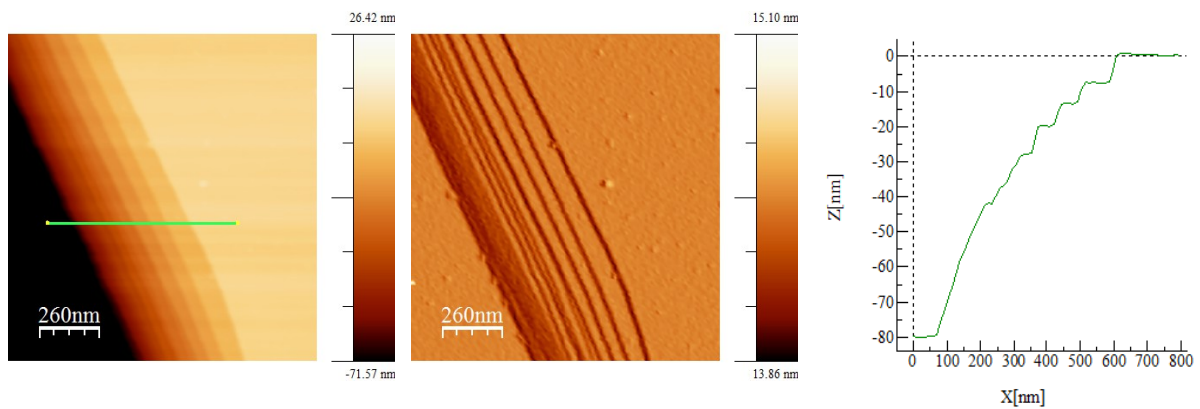
Figure 5.3.5. Stepped ledge. (a) Height. (b) Amplitude. (c) Profile section.

A negative electric surface potential of the order of hundreds of mV was measured on phlogopite surfaces by Kelvin probe force microscopy (see section 4.4 for an explanation of the method), featuring no significant variations on the surface of the same crystal.

Mechanical nanolithography (see sections 4.5 and 5.1.3.1 for details about the method) was employed in order to evaluate the force necessary to remove a single TOT layer. The experiments were performed in contact mode and with commercially available MPP-11100

cantilevers (Bruker, USA). Single layer removal was successfully obtained applying a vertical force of tens of nanonewtons with a scanning speed of about 1 μm·s⁻¹.

As a sake of example, figure 5.3.6 shows a topographic AFM image of a nanolithographed phlogopite surface. The first structural TOT layer, whose surface is visible in bright contrast in the image, was partially removed exposing the surface of the second structural TOT layer, that is visible in dark contrast. It was possible to remove the structural layer in a controlled manner such as to design a specific pattern. The topographic profile (bottom image), measured along the white line in the top image, reveals the dimension of two litographed nanochannels about 80 nm in width and only 1 nm depth, corresponding to the removal of a single TOT.
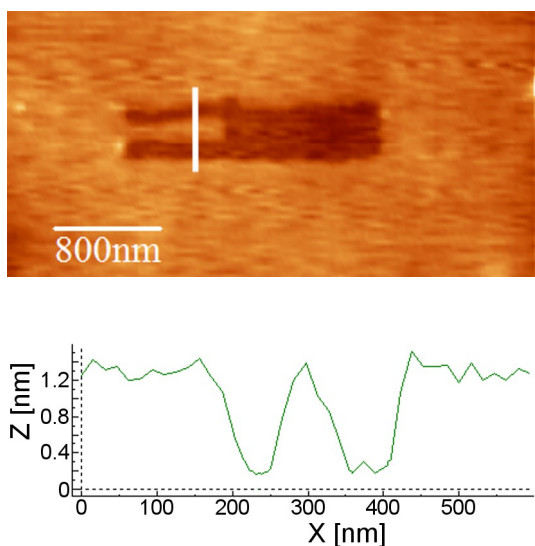
Figure 5.3.6. Single layer removal by mechanical nanolithography. Top: AFM topographic image of a nanometric pit on a phlogopite surface obtained by controlled removal of part of the first exposed structural layer. Bottom: topographic profile of two litographed nanochannels measured along the white line shown in the top image.

Unexpected cambers were observed at the surface of two phlogopite samples, BU1_7 and BU1_15, whereas no curvature features were observed on the BU1_17 crystal. These surface cambers will be here called "nanobubbles".

The general geometrical features of the nanobubbles are here reported: the lateral extension was typically of the order of hundreds of nanometres to several micrometres, the height from some nanometres to tens of nanometres, the aspect ratio from 0.01 to 0.09 and the shape of the projection on the (001) crystallographic plane of phlogopite was mostly circular or ellipsoidal.

76

On the surface of BU1_15 the nanobubbles presented mostly (>70%) a circular shape of the projection on the (001) plane, the others having an ellipsoidal shape. Circular shaped nanobubbles had a diameter between 240 nm and 1880 nm, whereas the ellipsoidal nanobubbles featured higher lateral dimensions, between about 1 μm and 4 μm. The height typically ranged between about 2 nm and 40 nm, reaching even 100 nm for the ellipsoidal nanobubbles.

BU1_7 featured a higher variability in the shape of the nanobubbles. Circular and ellipsoidal shapes of the (001) projection were observed as for the sample BU1_15; furthermore, complexes of combined nanobubbles and highly elongated structures were present.

As a sake of example, figure 5.3.7 shows some examples of the above cited shapes. In the upper left image it is shown an AFM topographic image of a camber (nanobubble) of the phlogopite surface. It presents a circular contrast with a diameter of about 500 nm and a height of about 10 nm. This geometrical features make this structure morphologically detectable only by atomic force microscopy. The upper right image shows another observed geometry. It reports an ellipsoidal nanobubble with a long axis of about 5.5 μm and a height of about 30 nm. The lower images show more complex geometric evidences. To better highlight the geometrical edges the images obtained from the amplitude signal are reported. The amplitude signal is related to the error of the feedback control system in maintaining an imposed constant oscillation amplitude during the scan. On the left, some structural features that can be described from a geometrical point of view as intersections of the circular nanobubbles previously observed; on the right, a group of cylindrical-type formations that follows a cleavage edge (not shown).
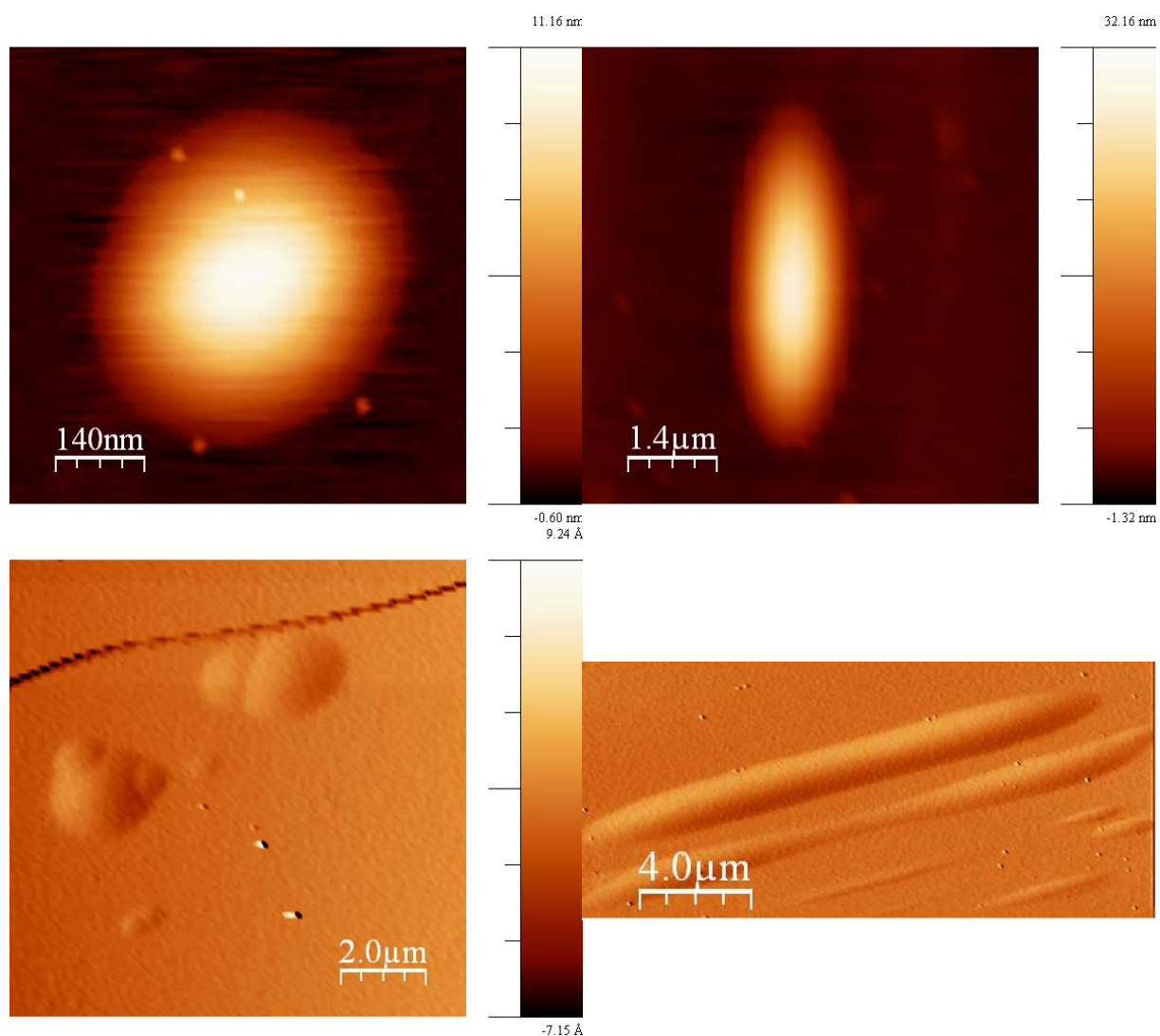
Figure 5.3.7. Top-left: circular-type nanobubbles; Top-right: ellipsoidal-type nanobubble; Bottom-left: complexes of combined nanobubbles; Bottom-right: cylindrical-type structures.

The circular-type nanobubbles were also observed to present an alignment following cleavage edges. This case is presented in figure 5.3.8 that reports an AFM topographic image where a sequence of approximatively circular nanobubbles with a roughly linear increment of their diameter is observed. However, this sequence of nanobubbles with an approximatively linear increment of their diameter was also observed not following a cleavage edge (not shown).
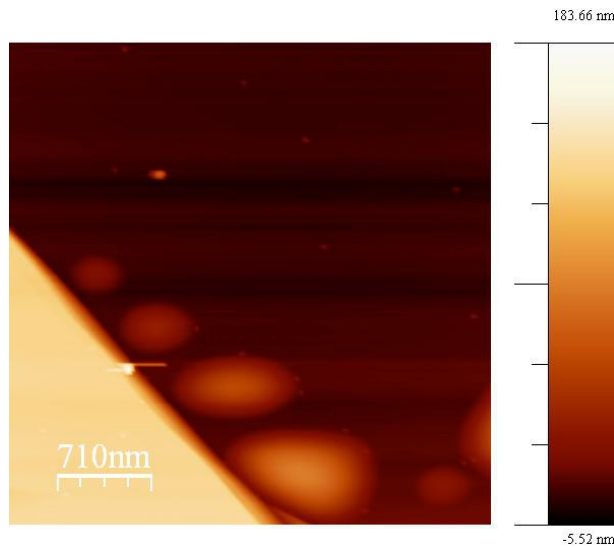
Figure 5.3.8. AFM topographic image of a sequence of nanobubbles with a diameter linearly increasing from about 350 nm to 850 nm, following a cleavage edge.

A visual example of the profile of a nanobubble with an aspect ratio of 0.04 (blue solid line) and one with an aspect ratio of 0.01 (green dash-dot line) is reported in figure 5.3.9.
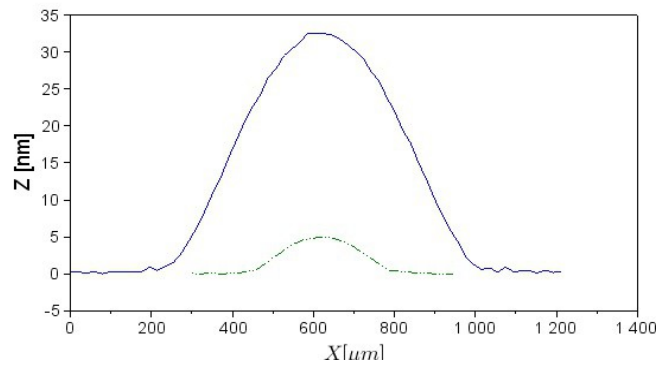
Figure 5.3.9. Height profiles of two nanobubbles with different aspect ratios (maximum height/maximum width).

The analysis of the phase signal contrast didn't provide qualitative evidence of a variation of the surface viscoelastic properties on the nanobubbles with respect to the flat areas.

Nanolithographic tests were also performed in order to help in evaluating the in depth position of the nanobubbles. The controlled removal of a single TOT layer was demonstrated,

and it was verified that the nanobubbles can be located even more than 160 nm below the cleavage plane.

In the following some working hypothesis on the chemico-physical nature of the nanobubbles will be presented and discussed.

The first working hypothesis suggests the presence of locally intercalated hydrated sodium or barium cations.

It is known from experiments and observations that during weathering potassium micas undergo both chemical and structural transformations. The interlayer potassium is replaced by hydrated cations and the original mineral structure changes to that of a vermiculite-like mineral (Krauss 1974). The exchange reaction is a diffusion process occurring between the mica and the aqueous solution of the exchanging cation. The exchange of the interlayer potassium with a cation is accompanied by the diffusion of water and an expansion of the basal spacing of the crystal structure. Furthermore, the diffusion of ions in minerals is evidently an important part of mineral-forming reactions.

In a recent study on K^+-Na^+ exchange in phlogopite on the scale of a single layer, Sánchez-Pastor and co-workers (2010) found that the replacement of K^+ by hydrated Na^+ causes the interlayer distance to swell by approximately 5 Å. The exchange reaction revealed some irreversible features, local irreversible structural irregularities attributed to trapped hydrated Na^+.

Furthermore, other studies on K^+-Ba^{2+} exchange in phlogopite (Krauss 1974) revealed a partial expansion during the ion exchange of the 10 Å basal spacing by 1 Å at 40°C and by 2.3 Å at 60°C and 80°C, and only a partial collapse of the expanded phase when heated to 500°C in air for two hours.

The second working hypothesis, that results from the X-ray photoelectron spectroscopy analysis (see section 5.3.2.2), is the presence of hydrocarbons or organic molecules trapped in the interlayer region.

The third working hypothesis is related to the presence of localized structural defects, such as stacking faults or dislocation loops. Specifically, for instance, (i) the local insertion of one unit cell of the $2M_1$ polytype into the 1M structure, or vice versa; (ii) the local presence of a different type of layer, e.g. a tetrahedral-octahedral TO layer.

The last working hypothesis suggests a crystal lattice mismatch that causes a local bending of the structural layer.

To assess the nature of these nanobubbles two highly resolved analytical approaches were employed (see the next section).

5.3.2.   Spectroscopic investigations

Micro-Raman and X-ray photoelectron spectroscopy were used in order to assess the chemical nature of the nanobubbles observed by atomic force microscopy morphological measurements at the surface of the three phlogopite samples and to investigate the phlogopite surface chemistry.

Figure 5.3.10. Composite optical map of the phlogopite sample BU1_7 with the indication of the main areas investigated by atomic force microscopy. The zones with a high concentration of nanobubbles where correlated with the corresponding atomic force microscopy images in order to help in the positioning of the analysing spot of the spectroscopic techniques.

These two analytical methods probe different sampling volumes: in the used experimental set-up, micro-Raman spectroscopy achieved a lateral spatial resolution of about 1 μm, sampling about 2 μm in depth, whereas X-ray photoelectron spectroscopy 50 μm of lateral spatial resolution and an in depth sampling < 10 nm.

In order to identify the position of the nanobubbles within the sample surface by means of the integrated optical microscopes of Micro-Raman and X-ray photoelectron spectrometer, given that the nanobubbles can be resolved only by the height sensitivity of atomic force microscopy, optical maps were created using a trinocular optical microscope equipped with a CMOS colour camera. Figure 5.3.10, 5.3.11 and 5.3.12 shows the optical maps created for the samples BU1_7, BU1_15 and BU1_17, respectively. Atomic force microscopy morphology images, showing the precise position of the nanobubbles, were superimposed to the optical maps for a better identification of the sample areas selected for the spectroscopic analyses.
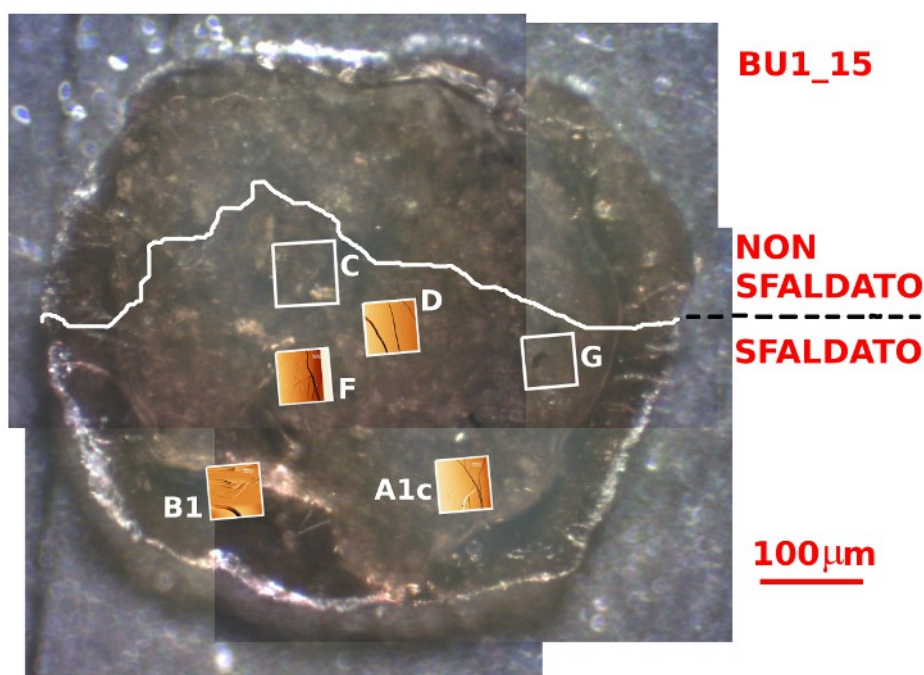
Figure 5.3.11. Composite optical map of the phlogopite sample BU1_15 with the indication of the main areas investigated by atomic force microscopy. The zones with a high concentration of nanobubbles where correlated with the corresponding atomic force microscopy images in order to help in the positioning of the analysing spot of the spectroscopic techniques. The white line defines the cleaved and not cleaved areas.
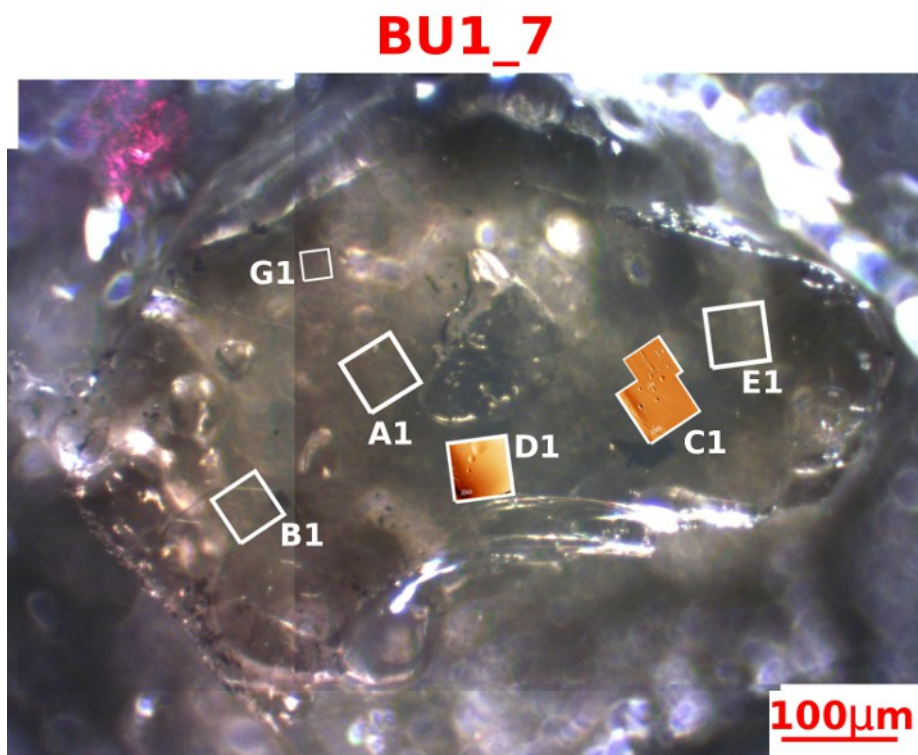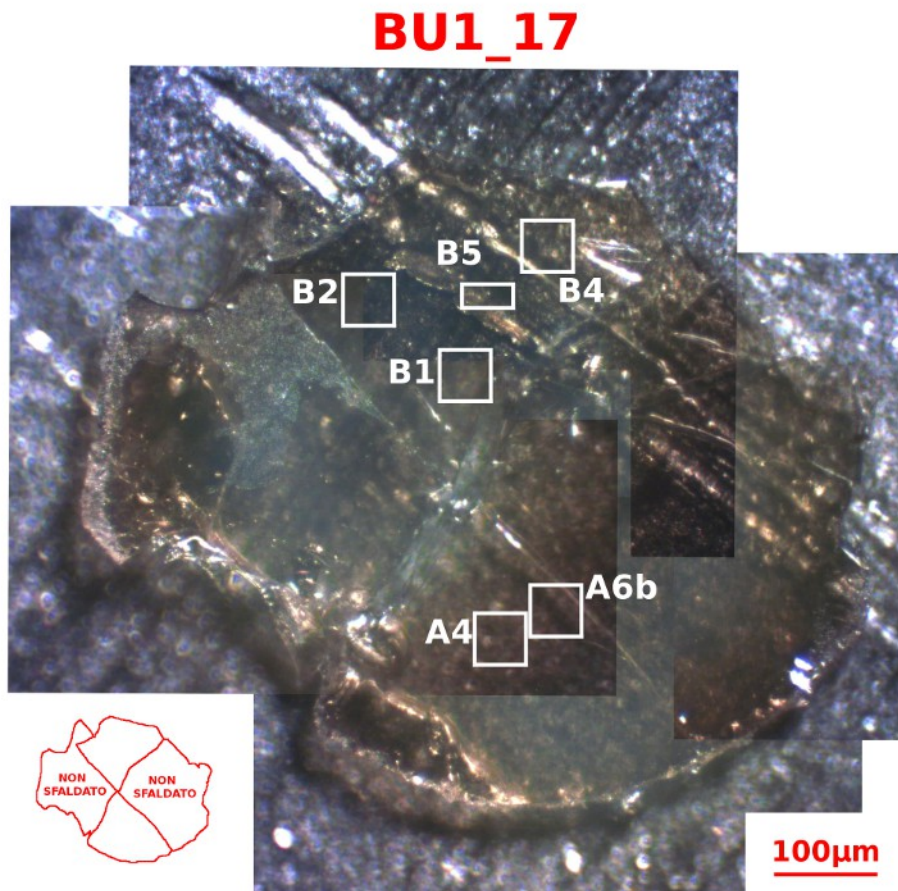
Figure 5.3.12. Composite optical map of the phlogopite sample BU1_17 with the indication of the main areas investigated by atomic force microscopy. No nanobubbles were observed in the investigated zones. The sketch in the lower-right part of the figure shows the cleaved and not cleaved areas of the sample.

5.3.2.1. Micro-Raman spectroscopy investigations

Micro-Raman spectroscopy experiments were conducted in order to investigate the chemical nature of the nanobubbles. Raman scattering measurements were performed on the phlogopite sample with higher concentration of nanobubbles, BU1_7, in the same zones previously characterized by atomic force microscopy and Kelvin probe force microscopy. The experimental set-up is described in section 4.6.

83

The experiments were conducted in air, at room temperature and standard pressure. The 100X objective was used for all the measurements, resulting in a probing volume of about 1 μm on phlogopite (001) crystallographic plane and about 2 μm in depth. The low dimension of the focal spot allowed a fine selection of the area to be analysed.

Raman spectra were acquired in the range 150 cm^{-1} to 3800 cm^{-1}, with integration times of 30 s and 3 accumulations to enhance the signal-to-noise ratio. Spectra were processed using the software CrystalSleuth version May 19, 2008 (Laetsch and Downs 2006).

A strong fluorescence effect was observed in all the measurements. Raman scattering and fluorescence emission are two competing phenomena, the last one tending to decrease the signal-to-noise ratio. Raman spectra are often affected by intense fluorescence backgrounds resulting from impurities or from the population of the excited states of the sample. Many transparent solid samples contains impurities that fluoresce under the laser beam excitation. The shape of fluorescence interference can result in a descending or ascending background, single broad peak, or even multiple sharp peaks. The background is generally a wide band signal that adds up to the Raman spectrum and is often of sufficient intensity to completely mask the weaker Raman scattering.

The raw data were treated with the background signal (baseline) extraction and elimination algorithm built-in CrystalSleuth.

Figure 5.3.13 shows, as an example, the raw spectrum acquired on an area where nanobubbles formations were observed by atomic force microscopy. The spectrum reports the trend of the intensity of the Raman signal as a function of the Raman shift in the range 150 cm^{-1} to 3800 cm^{-1}. A high background component was observed increasing towards higher wavenumbers.

Figure 5.3.14 shows a raw Raman spectrum acquired on an area with high concentration of nanobubbles of the phlogopite sample BU1_7 in the range of interest for phlogopite characteristic lattice vibrational modes, from 150 cm^{-1} to 1200 cm^{-1}. The same spectrum was processed to extract and eliminate the background component (figure 5.3.15).
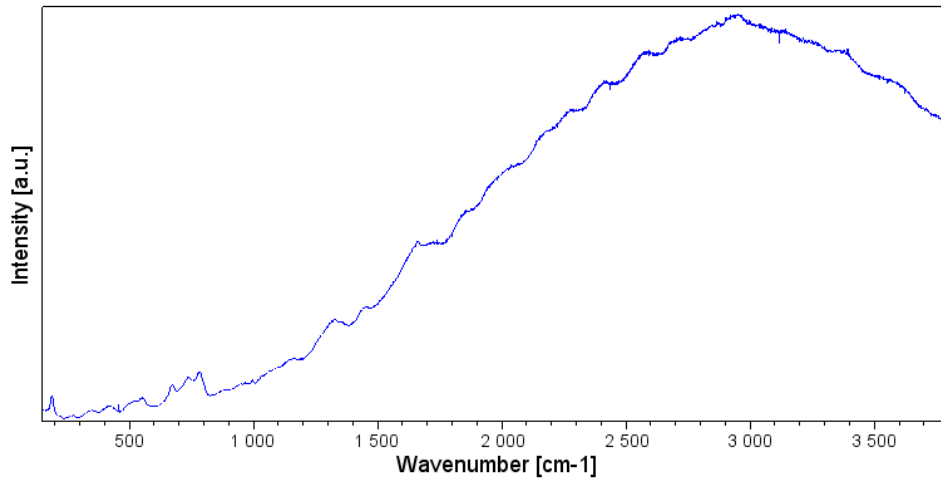
Figure 5.3.13. Raw Raman spectrum acquired on an area with high concentration of nanobubbles of the phlogopite sample BU1_7.
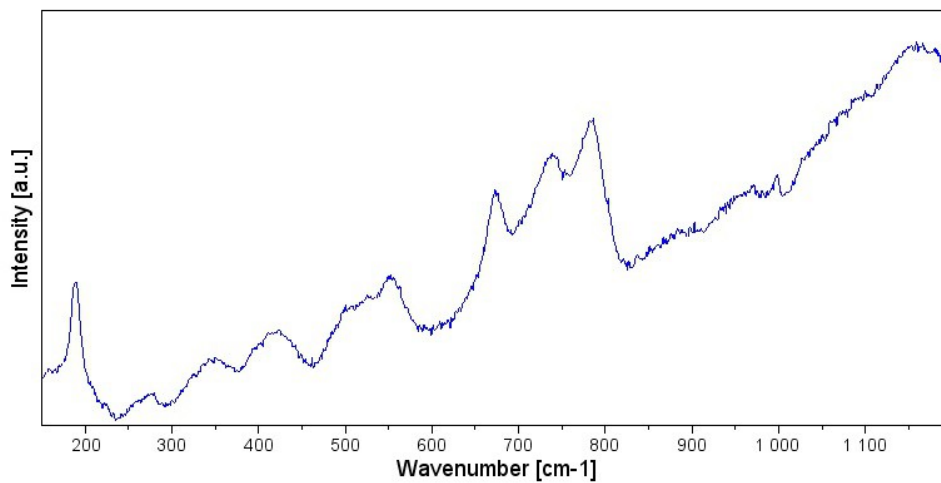
Figure 5.3.14. Raw Raman spectrum acquired on an area with high concentration of nanobubbles of the phlogopite sample BU1_7.
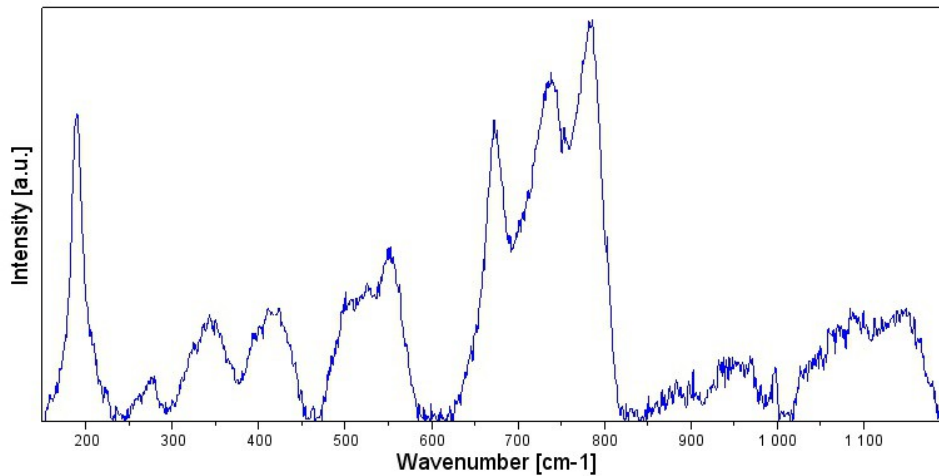
Figure 5.3.15. Raman spectrum of an area with high concentration of nanobubbles of the phlogopite sample BU1_7. The spectrum was obtained after background removing of the spectrum of figure 5.3.14.

From a profile comparison of the spectra acquired on the zone with expected presence of nanobubbles and zone without nanobubbles, no significative differences were observed. Several factors can contribute to explain this experimental evidence: the high fluorescence background may completely mask a weak Raman signal arising from the nanobubbles region; or the quantity of material involved in the nanobubbles formation is under the sensitivity of the technique; or a failure in the not trivial positioning of the small laser spot on the extended, flat and semi-transparent surface of the crystal; or a combination of the previous causes.

The identification of the detected Raman peaks was based on the comparison with the RRUFF Project Raman spectra database (Downs 2006) and with other Raman scattering studies from literature (McKeown *et al.* 1999, Šontevska *et al.* 2008, Tlili *et al.* 1989).

From the comparison of micro-Raman spectra profiles the sampled volume (lateral resolution of 1 μm and in depth sampling of 2 μm) was identified as a phlogopite. Good agreement was found with the phlogopite spectra of RRUFF Project database nr. 50485. Taking into account phlogopite spectra analysis from literature, the peak at 189 cm^{-1} may be assigned to tetrahedral sheets *xz* translatory motions and (F, OH) *z* translatory motions, the peak at 276 cm^{-1} to octahedra *y* translatory motions, the peak at 552 cm^{-1} to octahedra *xz*

86

translatory motions, the peak at 673 cm^{-1} to O-T-O bend motions (T: tetrahedral sites) and the peak at 784 cm^{-1} to the T-O stretch (McKeown *et al.* 1999).

5.3.2.2. X-ray photoelectron spectroscopy investigations

In order to investigate the composition of the nanobubbles and the crystal chemical modifications of the most superficial (< 10 nm) layers of phlogopites X-ray photoelectron spectroscopy analyses were performed (see section 4.7 for details on the experimental set-up). XPS is highly surface sensitive because of the inelastic mean free path of photoelectrons.

To obtain a precise positioning of the X-ray spot on the nanobubbles nanolithographic square and rectangular markers were created on the phlogopite surface in close proximity to the nanobubbles (figure 5.3.16). The dimensions of the markers were chosen such as to be visible through the trinocular optical microscope of the atomic force microscopy system and ranged from 5 μm to 10 μm in the lateral extension and about 200 nm in depth.
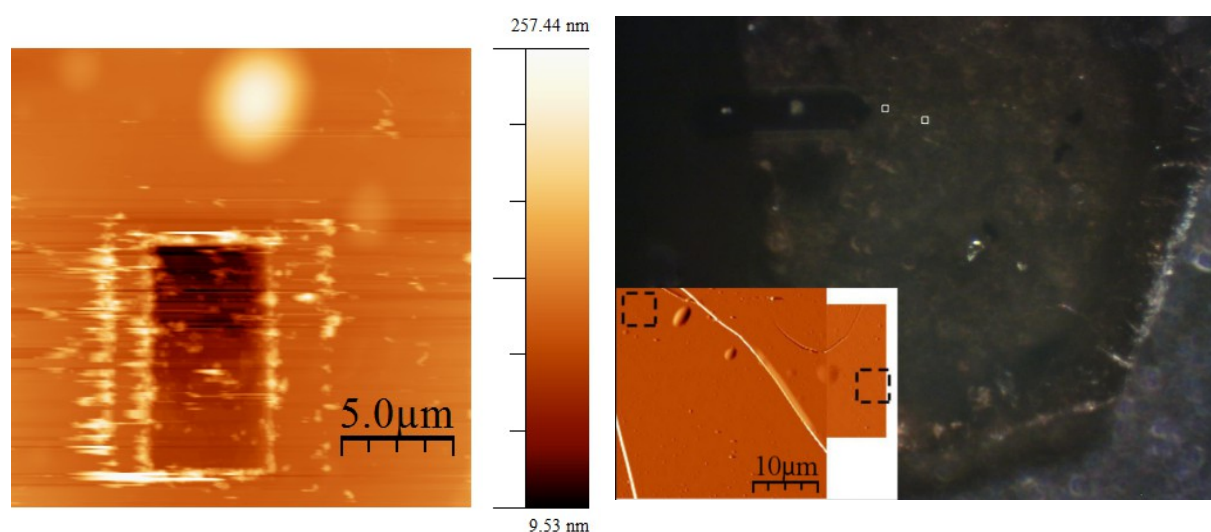
Figure 5.3.16. (a) Atomic force microscopy topographic image of a micrometric area of a phlogopite sample. A nanobubble of about 5 μm in diameter is visible in the upper part of the image. A nanolithographic rectangular shaped marker was created very close to the nanobubble and is visible underneath the nanobubble. (b) Example of optical map where it is indicated the position of the nanolithographic markers. The inset shows the position of the markers with respect to the nanobulles (AFM deflection image).

Figure 5.3.16a shows, as an example, a rectangular nanolithographic marker of 5 μm x 10 μm and about 200 nm in depth, created in close proximity to a nanobubble about 5 μm in diameter.

Figure 5.3.16b shows an example of optical map for the sample BU1_15, zone D1, where two white square frames clearly indicate the position on the crystal surface of the markers.

The inset in figure 5.3.16b shows an atomic force microscope image of the area of the sample surface where the markers were created. Two black square frames indicate the relative position of the markers with regard to the nanobubbles.

Among successive investigations the samples were stored in housings to minimize surface contamination.

Survey (binding energy range 0-1200 eV) and high resolution (C 1s, O 1s, Si 2p, Al 2p, Si 2s, Mg 2s, K 2p, Ba 3d, Na 1s core levels, and 0-100 eV) spectra were recorded at a pass energy of 200 eV and 100 eV, respectively, and 10 to 20 scans per measurement such as to obtain a good counting statistic (high peak to background intensity). Survey scans were performed for a qualitative elemental analysis, whereas higher resolution scans were taken for a quantitative analysis. Detailed scans allowed to determine the exact peaks position. The acquired spectra, emitted electrons number versus characteristic binding energy, were energy referenced to the aliphatic component of C 1s (binding energy = 284.8 eV). C 1s, Na 1s and Ba 3d high resolution spectra were collected to assess the chemical nature of the nanobubbles.

XPS analysis was performed on selected areas of the phlogopite samples BU1_7, BU1_15 and BU1_17. Both areas with high concentration of nanobubbles and areas with absence of nanobubbles were taken into account: zones C1, D1, E1 in BU1_7, zones A1c, D, F, C in BU1_15 and zones A4, B1 in BU1_17.

High resolution spectra were processed in order to quantify the atomic percentages. Background subtraction was performed with the Shirley algorithm (Shirley 1972). Selected peaks were analysed by curve fitting, deconvolved where possible, and the areas were measured. Hence, the atomic percentages were calculated with the relative atomic sensitivity factors.

The most intense peaks are the photoelectron peaks; some broader peaks are due to the emission of Auger electrons. The lower binding energy region contains the "valence band",

typically consisting of electrons shared in chemical bonds between atoms. The peaks are revealed upon a background that consists of Bremsstrahlung-excited photoelectrons to the right of the first photoelectron peak and is dominated by photoelectrons that underwent inelastic scattering to the left.

A spot of 50 μm in diameter was used to enhance the spatial resolution when analysing regions with presence of nanobubbles, whereas a spot of 200 μm in diameter was used to maximize the photoelectron signal.

X-ray photoelectron spectra of the survey wide-scans (figures 5.3.17, 5.3.19, 5.3.21) gave the qualitative identification of the elements present in the surface (depth sampling minus than about 10 nm). In accordance with electron probe microanalysis, K, Si, Ti, O, Fe, Na, Al and Mg were detected for the 200 μm spot measurements, and the peaks relevant to the principal mica components (Si, O, Al, Mg and K) were clearly observed also with the 50 μm spot. The narrow scans were used to derive accurate peak binding energies (figures 5.3.18, 5.3.20, 5.3.22).

XPS spectra show Si $2p3/2$ orbitals sharp peaks at a binding energy of 101.93 eV to 102.65 eV and full width at half maximum (FWHM) between 1.30 eV and 1.68 eV according to typical values for silicates (see figures 5.3.18, 5.3.20, 5.3.22). Where it was possible to deconvolve the Al $2p$ peak, Al $2p3/2$ binding energy was calculated between 72.56 eV and 74.20 eV, with FWHM from 1.14 eV to 1.72 eV. Mg $2s$ binding energy was between 88.47 eV and 88.88 eV, with FWHM from 1.69 eV to 2.24 eV. K $2p3/2$ binding energy was calculated between 293.37 eV and 293.70 eV, with FWHM from 1.24 eV to 1.62 eV. Ti $2p3/2$ and Fe $2p3/2$ were revealed only for the sample BU1_17 were a 200 μm spot was used. Ti $2p3/2$ binding energy was calculated between 459.05 eV and 459.37 eV, with FWHM from 1.87 eV to 1.89 eV. Fe $2p3/2$ binding energy was calculated between 710.16 eV and 710.45 eV, with FWHM from 3.66 eV to 4.46 eV.

These values were observed to be close to those reported in the literature for phlogopite (Schingaro *et al.* 2013) and in agreement with those expected in silicate minerals.

The survey wide-scans revealed the presence of carbon at the surface (figures 5.3.17, 5.3.19, 5.3.21). A carbon atomic percentage between about 18% and 50% was quantified, but with the used experimental set-up (type of beam, take-off angle, etc.) no correlation was

found with the presence of the nanobubbles. Curve fitting of the C 1*s* signal after Shirley background subtraction allowed to discriminate between the presence of C-H, C-O and C=O (see the specific narrow scan in figures 5.3.18, 5.3.20, 5.3.22). Carbon is not a component of phlogopite, therefore it was assigned as adventitious carbon contamination, that always occurs in XPS analyses, and/or the presence *a priori* of organic molecules or hydrocarbons occurring in the interlayer.

Barium was not detected at the experimental conditions of the present study, as clearly verifiable from the specific spectra of figures 5.3.18, 5.3.20, 5.3.22 that show a flat background signal at the binding energy of the expected Ba 3*d* peak. Sodium was not detected in sample BU1_7 (see the specific Na 1*s* spectrum of figure 5.3.20). Furthermore, although Na 1*s* peak was revealed in samples BU1_15 and BU1_17 (see the specific spectra of figures 5.3.18 and 5.3.22) with atomic percentages < 1.5%, no correlation was found with the areas with high concentration of nanobubbles.

These results don't exclude the hypothesis that the nanobubbles are the effect of locally intercalated hydrated sodium or barium cations. Indeed, the nanobubbles could be generated by interlayer cations located below the first 10 nm of investigated surface, and in addition the amount of atoms involved could be below the sensitivity of the analytical method.

Figure 5.3.17. XPS survey scan of sample BU1_17, zone A. Counts/s versus binding energy.

Figure 5.3.18. XPS high resolution spectra of sample BU1_17, zone A. From the left to the right and from the upper spectrum to the lower one: Si 2*s*, Si 2*p, Al 2p*, O 1*s*, Mg 2*s*, K 2*p*, Fe 3*p*, Ti 2*p*, Na 1*s*, Ba 3*d*, C 1*s*.
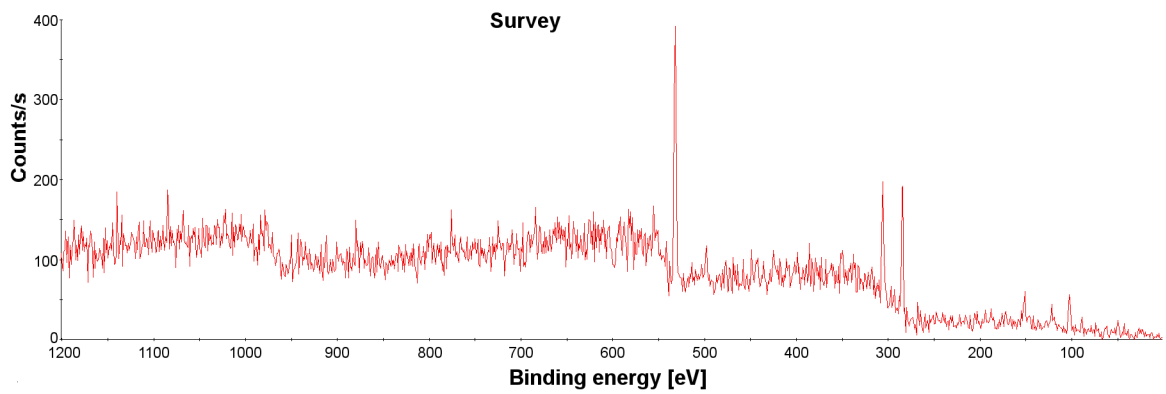
Figure 5.3.19. XPS survey scan of sample BU1_7, zone D1. Counts/s versus binding energy.
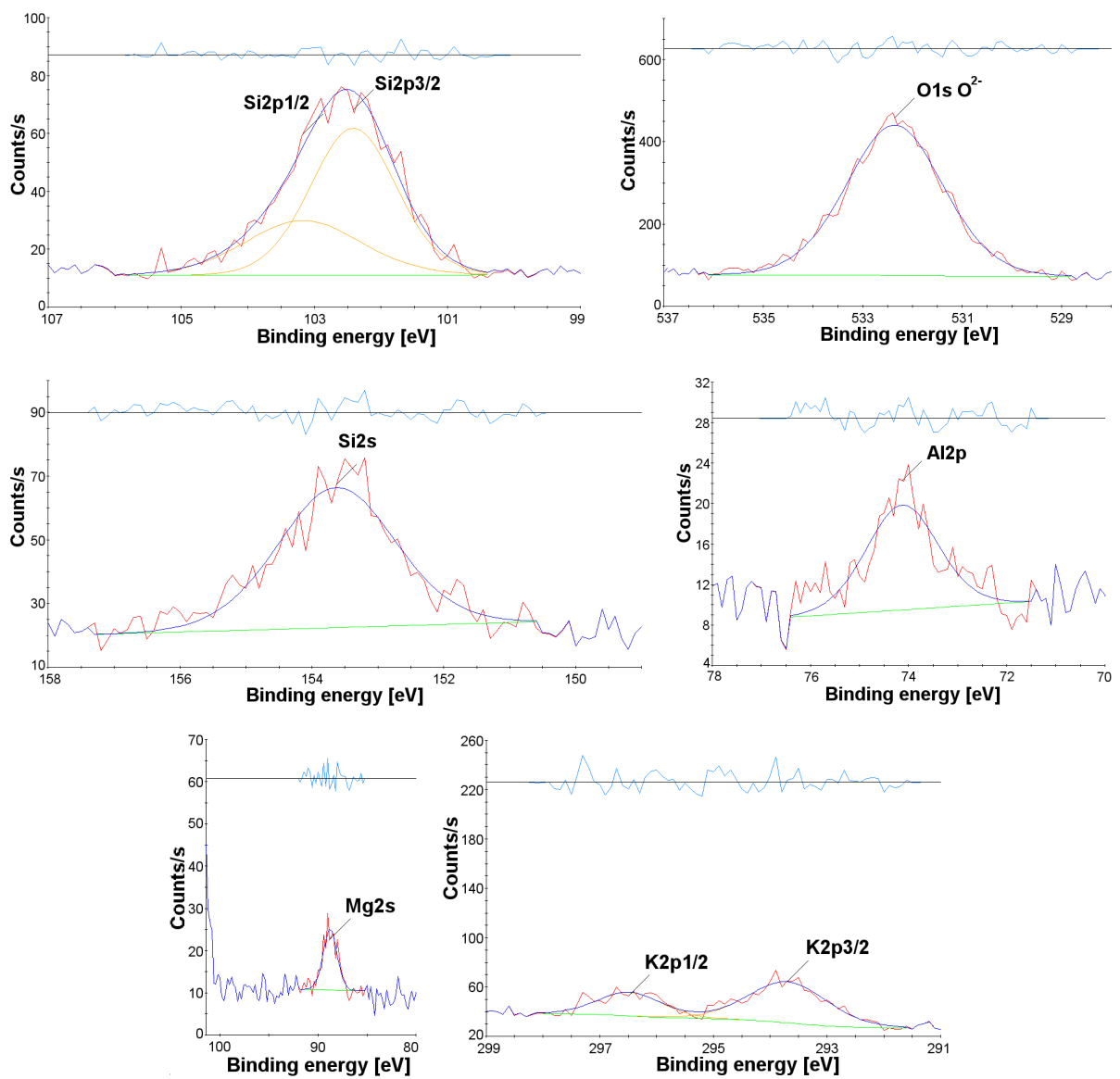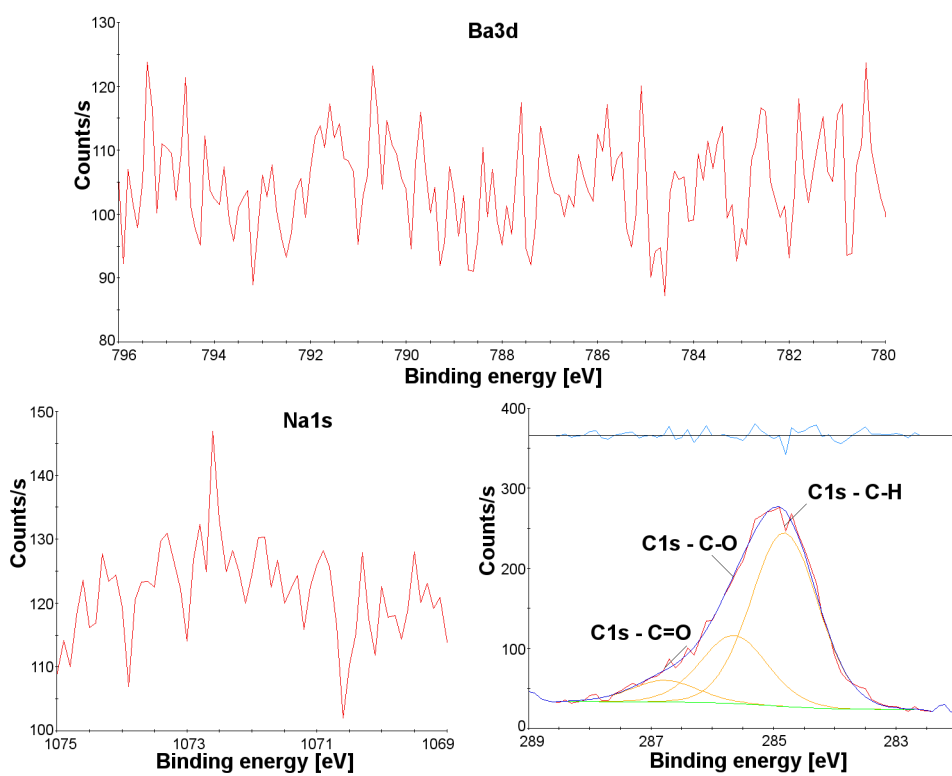
Figure 5.3.20. XPS high resolution narrow spectra of sample BU1_7, zone D1. From the left to the right and from the upper spectrum to the lower one: Si 2*p*, O 1*s*, Si 2*s*, Al 2*p*, Mg 2*s*, K 2*p*, Ba 3*d*, Na 1*s*, C 1*s*.
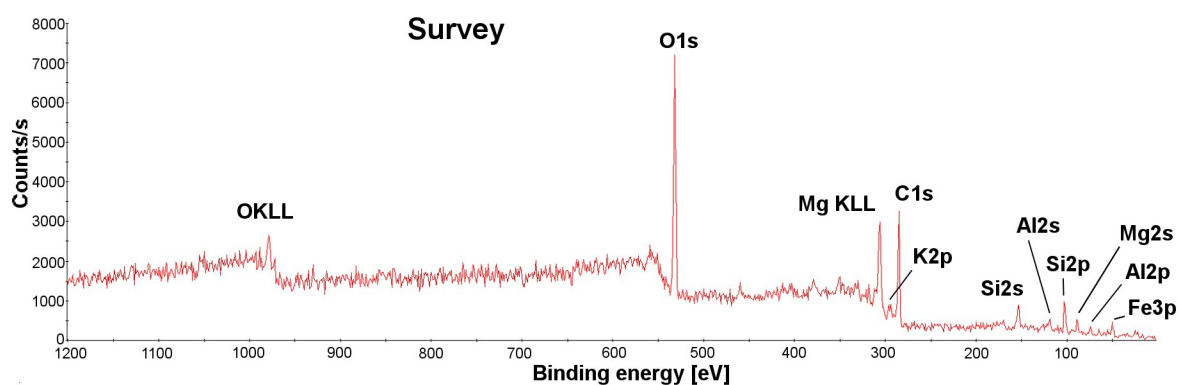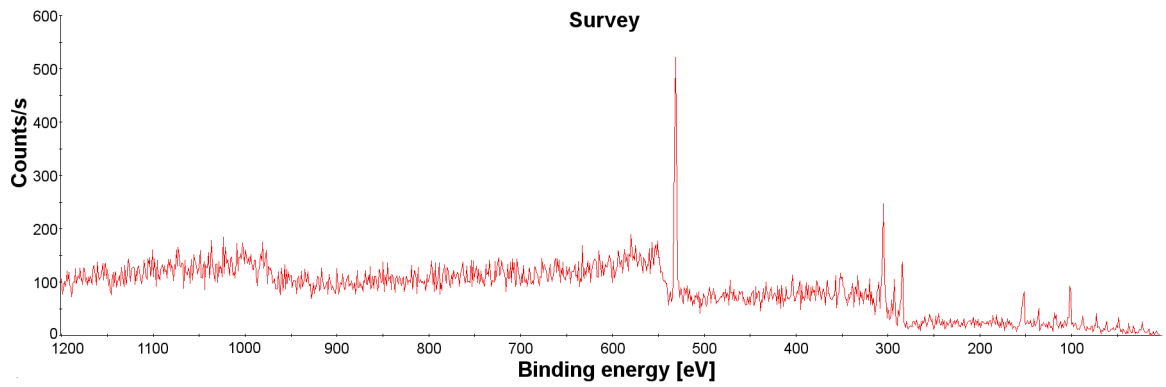
Figure 5.3.21. XPS survey scan of sample BU1_15, zone D. Counts/s versus binding enery.
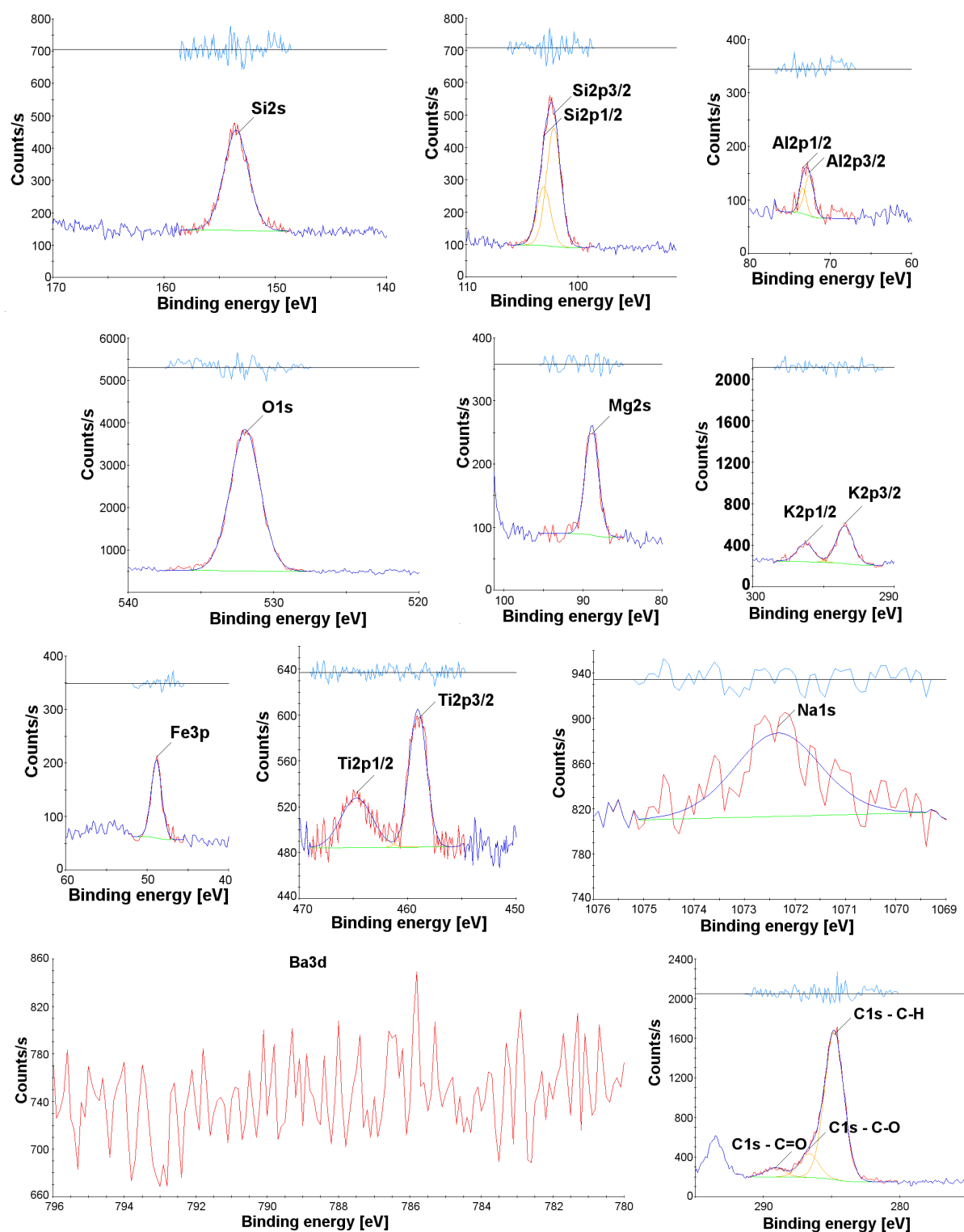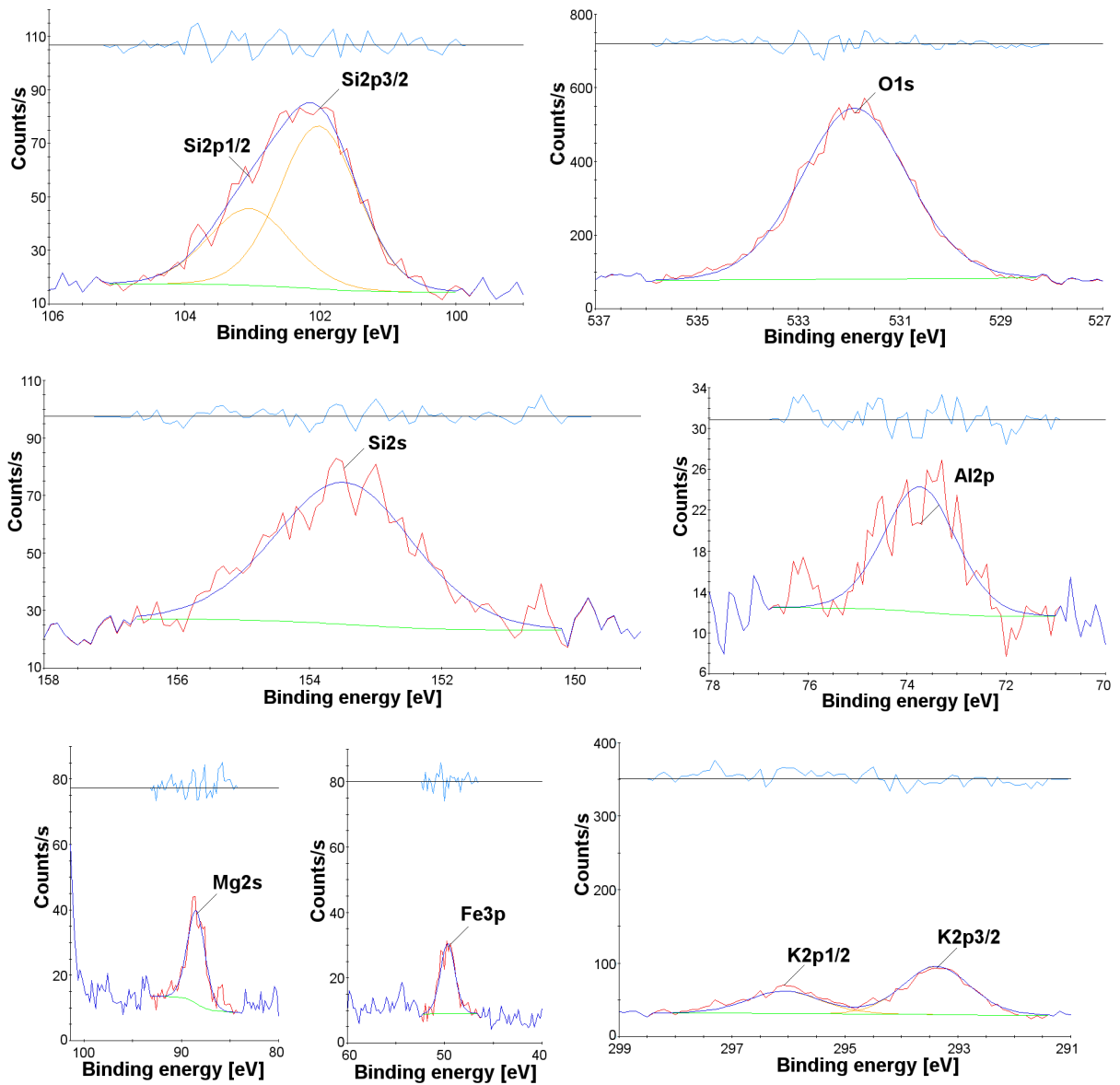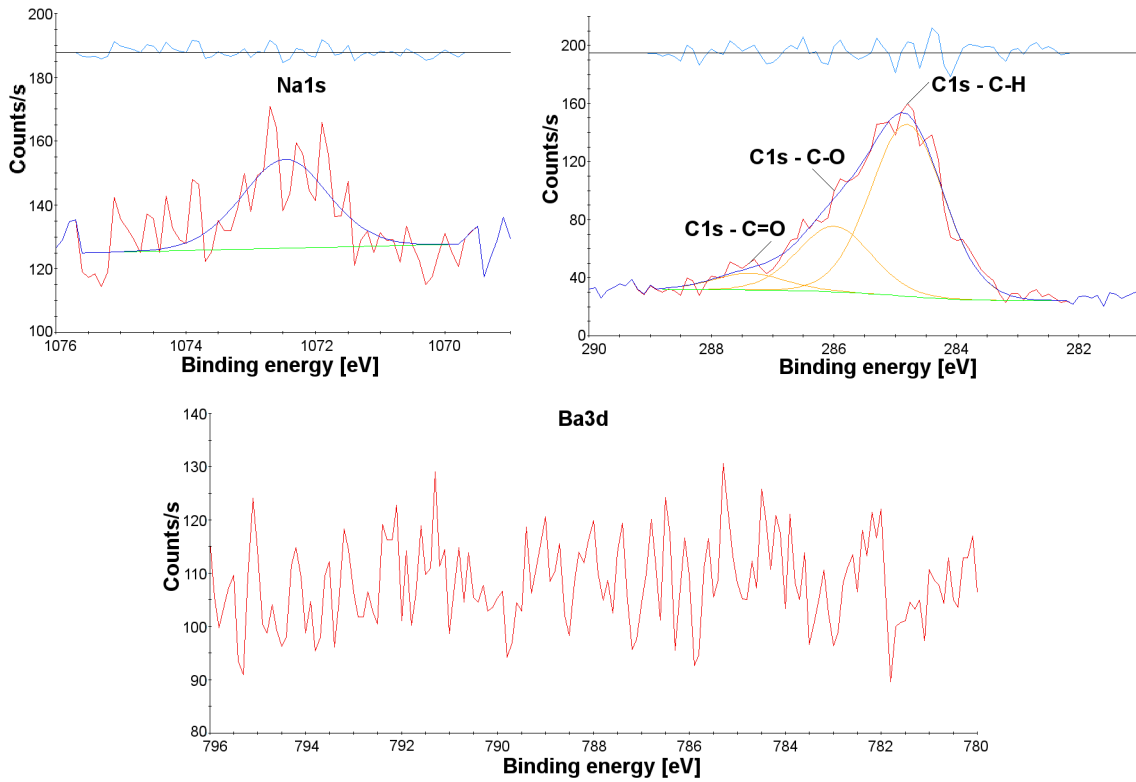
Figure 5.3.22. XPS high resolution narrow spectra of sample BU1_15, zone D. From the left to the right and from the upper spectrum to the lower one: Si 2*p*, *O 1s*, Si 2*s*, Al 2*p*, Mg 2*s*, Fe 3*p*, K 2*p*, Na 1*s*, C 1*s*, *Ba 3d*.

5.4.   Phlogopite-biomolecules interaction studies

In the present section the experimental results of SPM-based investigations on the interaction at the singe-molecule level of nucleotides and amino acids (glycine) with phlogopite (001) surface are reported and discussed. All the experiments were performed in air, at atmospheric pressure, room temperature (about 20°C) and relative humidity of about 55%.

5.4.1.   Nucleotides

Homogeneous mixtures of deoxyadenosine triphosphate, deoxythymidine triphosphate, deoxyguanosine triphosphate and deoxycytidine triphosphate were prepared to a final concentration of 10 μM at pH 7.5 and deposited onto (001) cleaved phlogopite surfaces following the procedure described in section 4.2.1.

Before the deposition, the phlogopite crystals were observed by atomic force microscopy to check for the presence of atomically flat and clean surfaces. After the deposition, the potential of phlogopite surface to concentrate and adsorb single molecules of nucleotides was evaluated by AFM observations performed in intermittent contact mode in order to minimize the probe-to-sample interaction, the probe-induced molecule deformation and the molecule dislodging.

Figure 5.4.1 shows, as an example, two AFM topographical images of a phlogopite (001) surface after nucleotides deposition. In figure 5.4.1a an area of 1.1 μm x 1.1 μm presents both single molecules of nucleotides and small agglomerated molecules adsorbed to the mineral surface. Figure 5.4.1b shows an area of 900 nm x 900 nm with prevalence of single molecules of nucleotides and some small multi-molecular agglomerates. The biomolecules were observed to be steadily bounded to the mineral surface, presenting no dragging effects during the scans. Analyses of the surface coverage were performed with ImageJ 1.47v, a scientific image-analysis program developed by Wayne Rasband at the National Institutes of Health, USA. A surface coverage from about 3% to 12% was calculated for the investigated surfaces.
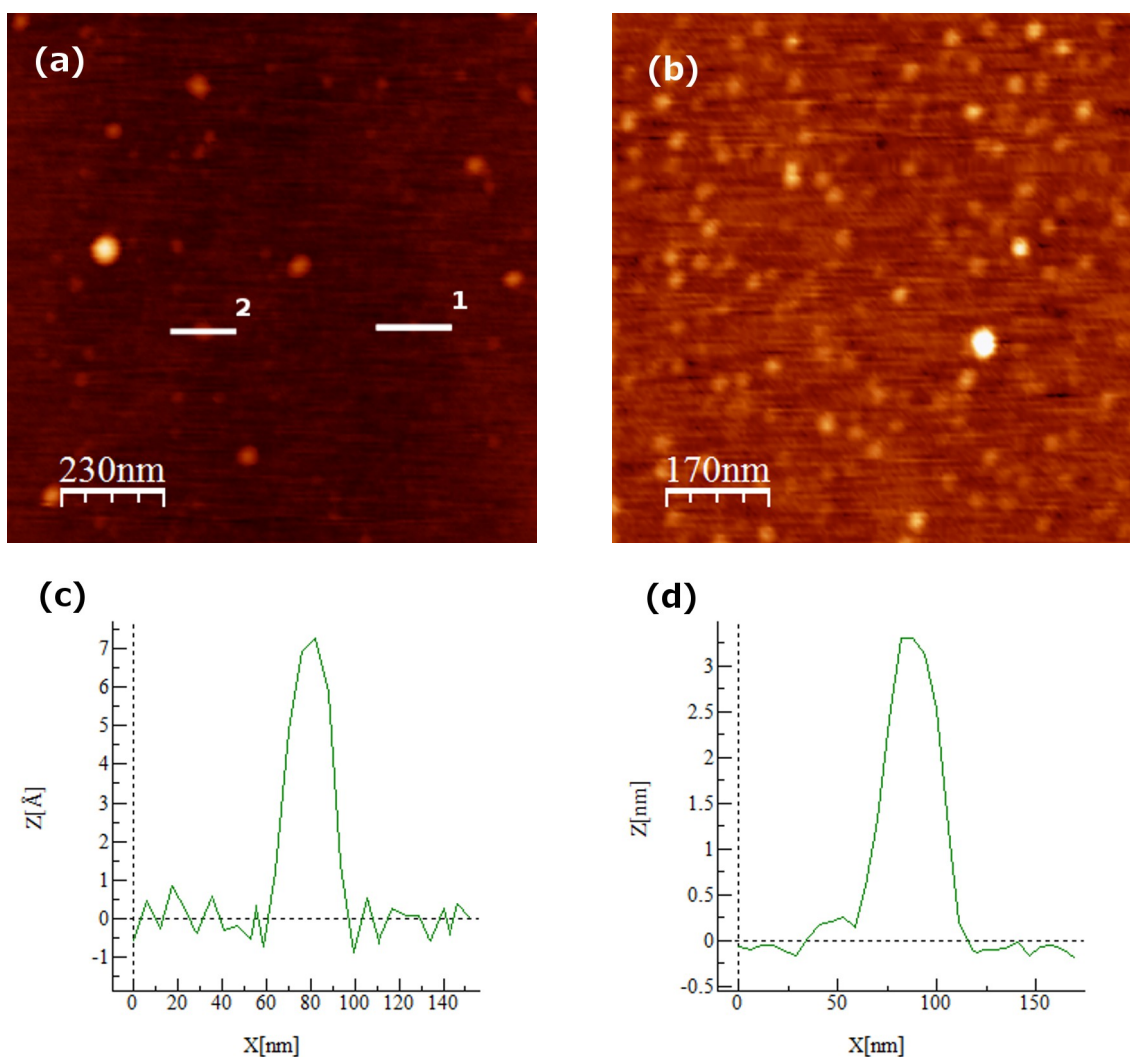
Figure 5.4.1. Molecules of nucleotides adsorbed on the surface of a phlogopite. (a), (b) AFM topographic images of the deposition of nucleotides from a 10 μM solution. Single molecules and agglomerates of nucleotides are visible. (c) Height topographic profile of a single nucleotide measured along the white line 1 shown in (a). (d) Height topographic profile of an agglomerate of nucleotides measured along the white line 2 shown in (a).

Figure 5.4.1c reports the topographic profile measured along the white line 1 of figure 5.4.1a and shows the measured thickness of a single nucleotide of about 0.8 nm and width of 22 nm. Figure 5.4.1d reports the topographic profile measured along the white line 2 of figure 5.4.1a and shows the measured thickness of an agglomerate of nucleotides of about 3.3 nm and width of 34 nm.

The phlogopite surface presents a higher coverage in comparison to the surface of the TOT layer of chlorite where no adsorbed nucleotides molecules were observed. However, it has to be considered that the surface of chlorite TOT layer was observed to be always associated to the presence of remaining parts of the brucite-like sheet of the interlayer. In principle, during the deposition process, the chlorite surface potential distribution concentrates and drives the nucleotides to adsorb at the brucite-like surface. Therefore, no molecules remain available to interact with the siloxane surface of the TOT.

5.4.2.   Amino acids

Molecules of glycine were deposited from a 150 μM solution onto freshly cleaved (001) phlogopite surfaces and nano-morphologically characterized in air by SPM.

At these experimental conditions glycine was observed to adsorb mainly as isolated single molecules and sometimes as agglomerates of several molecules. Figures 5.4.2a and b show the topographic and phase AFM images, respectively, of an area of 1 μm x 1 μm where single glycine molecules (bright spots) are visible, adsorbed on a (001) phlogopite surface (dark background).
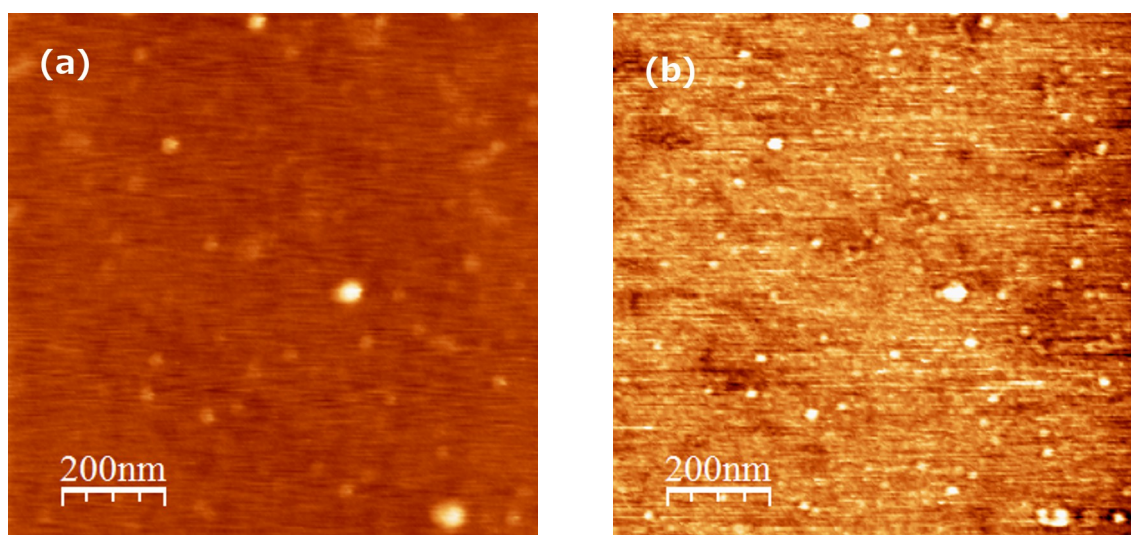
Figure 5.4.2. AFM topographic (a) and phase (b) images of glycine adsorbed on a phlogopite (001) surface.

The AFM phase signal is related to the phase lag between the exciting signal of the dither piezoelectric element and the cantilever oscillatory response, and is qualitatively related to the viscoelastic properties of the sample material. Indeed the AFM phase image of figure 5.4.2b clearly resolves the soft glycine molecules on the stiff mineral background. The surface coverage analysis gives figures of about 3%.

Figure 5.4.3 shows, on the left, a phlogopite crystal step imaged after glycine deposition. A high concentration of agglomerates of glycine molecules was observed at the edge, whereas mainly isolated single molecules were present on the terraces. The higher agglomeration at the edges could be explained in term of residual charges that develop where bonds are broken.
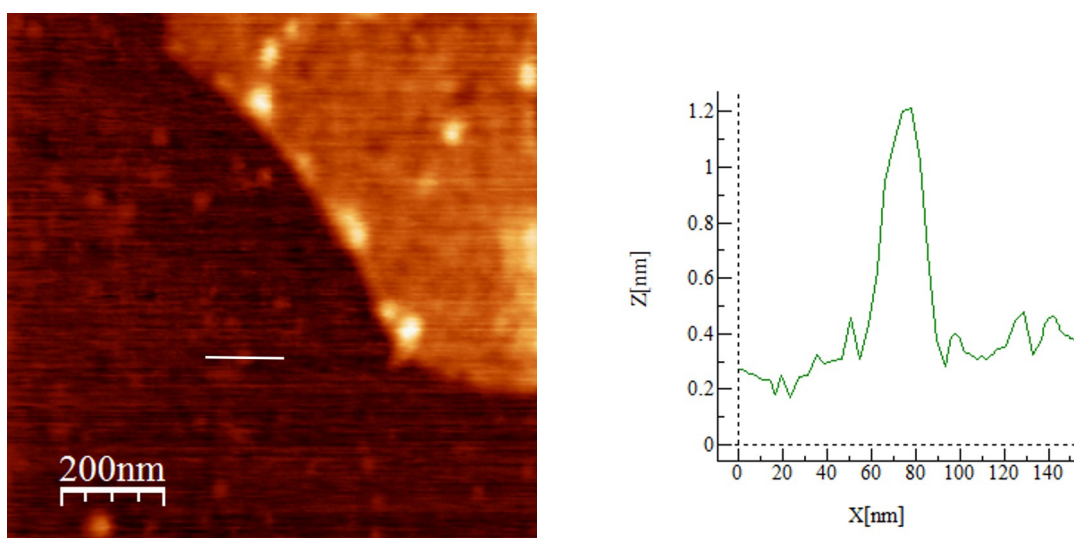
Figure 5.4.3. Left image: AFM topography of a phlogopite crystal step with several agglomerates of glycine molecules adsorbed at the edge. Right image: topographic profile of a single molecule of glycine measured along the white line in the image on the left side.

The right image of figure 5.4.3 shows a height topographic profile of a single glycine molecule measured along the white line in the image on the left side. The single molecule of glycine presents a height of about 0.9 nm and full width at half maximum of 21 nm.

6. CONCLUDING REMARKS AND FUTURE RESEARCH

The main objective of this research project was to study the surface properties of chlorite and phlogopite by using and, in some cases, developing and optimizing advanced experimental approaches at the nanoscale, and to investigate the effect of the sub-nm physico-chemical properties of chlorite and phlogopite surfaces on the interaction with fundamental biomolecules. The surface properties of minerals at the nanoscale and their interaction with biomolecules are not known. Furthermore, the few data available in literature are sometimes controversial because they are derived from bulk measurements of nanostructured surfaces. In particular, nanomorphology, the electrostatic surface potential nanodistribution, single layer detachment, surface chemistry and affinity with single fundamental biomolecules were investigated. Chlorite revealed extended atomically flat surfaces mainly presenting fragmented interlayer octahedral sheets, about 0.5 nm thick, over a continuous 2:1 layer, about 1 nm thick. This mineral presents at the surface nano-confined electric potential gradients because of its peculiar crystal-chemistry (e.g., Al isomorphous substitution for Si in the tetrahedral sheets of the 2:1 layer). In order to characterize the effective surface potential, scanning probe microscopy based methods were developed and optimized for the investigation of mineral surfaces (e.g., static electric force microscopy, single pass amplitude-modulation Kelvin probe force microscopy). Variations of the effective surface potential difference ranging between 50-100 mV and 400-500 mV, when measured in air, between the TOT surface and the interlayer sheet, were measured by Kelvin probe force microscopy and confirmed by the static-EFM method developed in the context of this thesis and described in section 4.4. These surface potential values, that are variable at the nanoscale, explain the controversial data of chlorite isoelectric point bulk measurements reported in literature. Atomic force microscopy was used to investigate and compare the surface affinity, self-assembly and nanopatterning of nucleotides, RNA, DNA and amino acids (glycine). All the molecules are selectively adsorbed on the surface of the interlayer octahedral sheet, with a higher concentration at the edge. No adsorption on the siloxane surface of the 2:1 layer was instead observed for all biomolecules. Nano-confined electric potential gradients were ascribed to be the driving force that aligns nucleotides at the edges of the interlayer sheets to form long filamentary structures. After the deposition, the typical RNA observed

morphologies were the following: (i) stable linearised conformations (fragments and single molecules at the edges of the interlayer sheet), (ii) single agglomerates and (iii) multiple agglomerates (e.g., globular domains separated by linear tracts). The surface potential of chlorite was also able to drive the DNA deposition. Linearised and stretched DNA single molecules, between the edges of two brucite-like stripes were observed. The extension of the stretching was more than 2 μm, corresponding to more than 6000 bp. The experiments conducted on the interaction of single molecules of glycine with the chlorite surface, using a deposition solution at pH 7.6, revealed at those experimental conditions a high affinity with the brucite-like surface. Glycine stably adsorbs, assembles in patterns and concentrates on the brucite-like surface. Single molecules of glycine align along the crystallographic edges of brucite-like sheets. These observations suggest a role of chlorite surface in the concentration, adsorption, alignment and probably polymerization process of amino acids, a question that will be the subject of future researches. The stable adsorption of glycine driven by van der Waals and weak electrostatic forces allowed to resolve a single molecule measured about 1 nm in height and 9.6 nm wide.

The discovered forms of self-assembly, patterning and selective interaction of single molecules of nucleotides, RNA, DNA and amino acids on the chlorite peculiar surface are useful in several areas of environmental sciences and nano-biotechnology when it is necessary to dispose of sub-nanometer features or nanopatterned positive and negative templates, for instance, in nanolithography, self-assembly, dissections or alignment of bio/organic molecules for life science and polymer research and technology.

I found that the anisotropic surface properties of atomic-flat chlorite concentrate, adsorb at the surface, nano-confine and align single molecules of nucleotides, RNA, DNA and amino acids (glycine). These findings can give a contribution to the development of the theories on prebiotic synthesis of biomolecules and the origin of life on earth.

Etching and oxidation at the nanometer scale of chlorite surface using the same SPM probe for the creation of organized nanopatterns was demonstrated. In particular, it is possible to produce three-dimensional nanostructures in a reproducible way, with a depth resolution of 0.4 nm (due to crystal-chemistry), lateral resolution of tens of nm, and a speed of about 10 $\mu m \cdot s^{-1}$. It was demonstrated, for instance, the construction of an atomically flat charged

pattern, designed to guide DNA deposition along predetermined directions without need of any chemical functionalization of the surface.

The presented nanolithographic method offers unique applications in several areas of bio-nanopatterning and particularly for surface driven deposition of bio-molecules. The etching of chlorite offers the unique benefit of producing nanometre-size features with negative charge surrounded by an atomically flat positive layer. The fabrication of edge charged corners and the relative high electric field gradient can be used to orient molecules and, more generally, nanoscale objects. It was shown how this property can be applied very effectively to manipulate single DNA molecules to stretch between predetermined positions. Similar procedures can be readily extended to other charged organic molecules for life science and polymer research where the exploitation of self-assembled mechanisms on large scale is in high demand.

Investigations on phlogopite revealed atomically flat surfaces (RMS roughness analysis gave values under the piezoelectric scanner z position noise, 0.1 nm) extending for more than 50 µm x 50 µm and generally featuring surface steps from the single layer, about 1 nm thick, to about 400 nm. Highly curved edges were observed with a radius of curvature of less than 2 µm. Single layer removal was also demonstrated. A negative surface potential of the order of hundred of mV was measured by Kelvin probe force microscopy, featuring no significant variations on the surface of the same crystal. Unexpected cambers were occasionally observed at the surface of two phlogopite crystals which were called "nanobubbles". The lateral extension was typically of the order of hundreds of nanometres to several micrometres, the height from some nanometres to tens of nanometres, the aspect ratio ranged from 0.01 to 0.09 and the shape of the projection on the (001) crystallographic plane of phlogopite was mostly circular or ellipsoidal. Hypothesis on the chemico-physical nature of the nanobubbles included intercalated hydrated barium or sodium cations, hydrocarbons or organic molecules, or the presence of a crystal lattice mismatch or structural defects, such as dislocation loops or stacking faults. Attempts to determine the chemical nature of theses features by micro-Raman spectroscopy and X-ray photoelectron spectroscopy failed. Possible explanations are: limitations of the experimental set-ups (e.g., reduced sensitivity when using small spots of the incident beam); extremely low amount of material to be detected; or bulk location of the

intercalated material or of the mixed layers. The surface composition was found comparable with the bulk one.

A low affinity of nucleotides and glycine molecules with phlogopite in respect of the brucite-like surface of chlorite was observed. However, the adsorbed molecules revealed a bond strength enough to allow an easy AFM imaging without biomolecules dislodging. At the specific experimental conditions of this research both nucleotides and glycine molecules arranged onto the phlogopite surface mainly as isolated single molecules and sometimes as agglomerates.

Future researches are suggested on the basis of the results of this work.

The observation of the chlorite ability to align nucleotides and amino acids suggests the use of specific mass spectrometry experiments to investigate the catalytic potential of chlorite surface to promote polymerization.

As for the nanobubbles identity question, an extremely new techniques that combines atomic force microscopy and infrared spectroscopy for nanoscale chemical characterization could help in addressing the problem and is envisaged to be used.

A method to investigate the surface potential of a mineral in liquid using the AFM signal phase shift was designed and is under development. The phase lag between the excitation signal and the response of the cantilever during a scan can be related to the surface potential (Baumann & Stark, 2010). By monitoring the phase contrast on a mineral surface in a liquid environment, information on the surface potential variation can be obtained. The liquid environment can be controlled by means of a fluid cell, therefore the pH of the solution can be changed while measuring the phase lag induced by the surface potential variation. These experiments can give important contributions for the determination of the point of zero charge or pH-related variation of surface potential at nanometre scale resolution.

7. APPENDIX

7.1. Definitions

Isoelectric point: the pH at which the zeta potential is zero.

Point of zero charge: the pH at which the surface charge (at the particle surface) is zero. For most minerals, the isoelectric point matches the point of zero charge if no specific adsorption occurs.

Quality factor: an intrinsic parameter of a mechanical resonator which clarify the resonator dissipation. It is defined as $Q = f/\Delta f$, where f is the resonant frequency of the resonator and Δf is the bandwidth.

Zeta (or electrokinetic) potential: the potential measured at the slipping plane as the mineral particle moves relative to the liquid (aqueous solution). It can be assumed equal to the potential at the outer Helmholtz plane.

7.2. Supplementary material

XPS data

BU1_7, blank, spot 50μm

Name	Start BE	Peak BE	End BE	Height [CPS]	FWHM [eV]	Area (P) [CPS·eV]	At. %	SF
C1s - CH	287.86	284.76	282.67	435.55	1.06	497.83	32.46	0.919
C1s - C-O	287.86	285.33	282.67	204.04	1.06	233.21	15.21	0.919
C1s - C=O	287.86	286.59	282.67	42	1.06	48.01	3.13	0.919
O1s - O^{2-}	537	532.51	529.4	333.43	2.15	774.87	20.91	2.449
Si2p3/2	105.1	102.41	100.3	50.8	1.31	72.23	7.58	0.539
Si2p1/2	105.1	103.21	100.3	21.69	1.54	36.11	7.43	0.275
Si2s	156.99	153.64	150.76	41.46	2.26	101.17	5.97	0.974
Al2p3/2	76.4	74.2	72.2	6.51	1.47	10.29	1.89	0.306
Al2p1/2	76.4	74.74	72.2	3.28	1.45	5.15	1.89	0.153
Mg2s	91.6	88.8	85.63	18.16	1.69	33.12	3.51	0.532

BU1_7, zone C1, spot 50μm

Name	Start BE	Peak BE	End BE	Height [CPS]	FWHM [eV]	Area (P) [CPS·eV]	At. %	SF
Al2*p*	76.1	74.2	71.4	10.46	1.79	20.28	3.08	0.458
C1*s* - C-H	287.8	284.81	282.8	162.54	1.17	213.26	17.24	0.919
C1*s* - C-O	287.8	285.2	282.8	116.09	1.17	152.31	12.31	0.919
C1*s* - C=O	287.8	286.28	282.8	23.82	1.17	31.26	2.53	0.919
K2*p*1/2	297.6	296.31	292	21.59	1.17	27.43	1.5	1.367
K2*p*3/2	297.6	293.54	292	40.94	1.24	55.03	1.55	2.649
Mg2*s*	92.2	88.5	84.8	18.16	2.14	42.05	5.53	0.532
O1*s* - O²⁻	536.1	532.18	528.7	365.52	2.16	903.15	30.19	2.449
Si2*p*1/2	104.6	102.99	100.3	32.97	1.01	36.23	9.24	0.275
Si2*p*3/2	104.6	102.19	100.3	51.65	1.3	72.46	9.43	0.539
Si2*s*	157.71	153.45	149.38	41.02	2.3	101.35	7.41	0.974

BU1_7, zone D1, spot 50μm

Name	Start BE	Peak BE	End BE	Height [CPS]	FWHM [eV]	Area (P) [CPS·eV]	At. %	SF
C1*s* - C-H	288.5	284.82	282.7	217.2	1.29	303.79	22.98	0.919
C1*s* - C-O	288.5	285.65	282.7	85.22	1.29	119.2	9.02	0.919
C1*s* - C=O	288.5	286.77	282.7	27.05	1.29	37.83	2.86	0.919
O1*s* - O²⁻	536.1	532.36	528.8	365.77	2.29	905.05	28.32	2.449
Si2*p*3/2	105.8	102.42	100.4	50.83	1.52	83.6	10.18	0.539
Si2*p*1/2	105.8	103.17	100.4	18.87	2.06	41.8	9.98	0.275
Si2*s*	157.3	153.63	150.6	44	2.1	99.99	6.84	0.974
Mg2*s*	91.8	88.75	85.2	14.35	1.66	25.85	3.18	0.532
Al2*p*3/2	76.4	74.13	71.5	10.38	1.72	19.33	2.75	0.458
Al2*p*1/2	76.4	74.85	71.5	2.06	3.02	6.56	0.93	0.458
K2*p*3/2	298	293.69	291.6	33.4	1.62	58.78	1.55	2.649
K2*p*1/2	298	296.48	291.6	19.28	1.33	27.68	1.41	1.367

BU1_15, blank, spot 50μm

Name	Start BE	Peak BE	End BE	Height [CPS]	FWHM [eV]	Area (P) [CPS·eV]	At. %	SF
Al2p3/2	76.8	73.5	71.5	14.79	1.14	18.31	2.53	0.458
Al2p1/2	76.8	74.55	71.5	6.51	1.29	9.14	1.26	0.458
C1s - C-H	288.8	284.8	282.6	114.68	1.27	157.65	11.59	0.919
C1s - C-O	288.8	285.8	282.6	48.87	1.27	67.18	4.94	0.919
C1s - C=O	288.8	287	282.6	19.18	1.27	26.36	1.94	0.919
Fe3p	53.06	49.75	48.02	26.61	1.21	34.75	1.79	1.221
K2p1/2	298.9	296.11	291.4	29.78	1.52	49.02	2.43	1.367
K2p3/2	298.9	293.4	291.4	61.83	1.46	97.76	2.5	2.649
Mg2s	92.8	88.48	84.6	24.63	2.24	59.78	7.15	0.532
Na1s	1074.8	1072.29	1069.7	37.77	1.92	77.75	1.3	6.631
O1s - O²⁻	535.9	531.9	528.6	444.97	2.46	1162.89	35.34	2.449
Si2p1/2	105.4	103	99.7	25.84	1.54	43.12	10	0.275
Si2p3/2	105.4	102.1	99.7	54.94	1.45	86.24	10.2	0.539
Si2s	156.1	153.42	151	47.79	2.07	105.77	7.03	0.974

BU1_15, zone A1c, spot 50μm

Name	Start BE	Peak BE	End BE	Height [CPS]	FWHM [eV]	Area (P) [CPS·eV]	At. %	SF
C1s - C-H	291	284.77	281.7	203.25	1.62	356.81	34	0.919
C1s - C-O	291	286.5	281.7	59.04	1.62	103.65	9.88	0.919
C1s - C=O	291	288.82	281.7	20.04	1.62	35.19	3.36	0.919
Al2p	75.4	73.85	72.5	5.12	1	5.52	0.99	0.458
O1s - O²⁻	536.2	532.21	528.7	245.32	2.81	741.81	29.24	2.449
Si2p3/2	105.4	101.93	100	28.71	1.37	42.45	6.51	0.539
Si2p1/2	105.4	102.99	100	11.34	1.73	21.23	6.39	0.275
Si2s	156.2	153.32	149.53	24.3	2.85	74.32	6.41	0.974
Mg2s	92.8	88.54	84.2	9.1	2.11	20.75	3.22	0.532

BU1_15, zone D, spot 50μm

Name	Start BE	Peak BE	End BE	Height [CPS]	FWHM [eV]	Area (P) [CPS·eV]	At. %	SF
Al2*p*	76.73	73.74	71	12.26	1.71	22.76	2.96	0.458
C1*s* - C-H	288.8	284.81	282.2	118.63	1.41	180.66	12.53	0.919
C1*s* - C-O	288.8	285.99	282.2	45.4	1.41	69.13	4.8	0.919
C1*s* - C=O	288.8	287.39	282.2	11.29	1.41	17.2	1.19	0.919
Fe3*p*	52.2	49.69	46.68	21.44	1.76	40.73	1.98	1.221
K2*p*1/2	298.4	296.07	291.4	30.51	1.51	49.81	2.33	1.367
K2*p*3/2	298.4	293.37	291.4	65.8	1.39	99.38	2.4	2.649
Mg2*s*	93	88.47	84.4	28.39	2.15	65.98	7.44	0.532
Na1*s*	1075.6	1072.47	1069.8	27.86	1.56	47.03	0.74	6.631
O1*s*	535.8	531.89	528.3	464.81	2.47	1239.33	35.54	2.449
Si2*p*1/2	105.1	103.04	100	28.66	1.45	44.97	9.84	0.275
Si2*p*3/2	105.1	102.02	100	60.85	1.36	89.94	10.04	0.539
Si2*s*	156.6	153.48	150.17	49.37	2.47	130.92	8.21	0.974

BU1_15, zone F, spot 50μm

Name	Start BE	Peak BE	End BE	Height [CPS]	FWHM [eV]	Area (P) [CPS·eV]	At. %	SF
Al2*p*	76	73.98	72	14.17	1.32	20.14	2.57	0.458
C1*s* - C-H	288.7	284.83	282	123.99	1.23	165.25	11.21	0.919
C1*s* - C-O	288.7	285.71	282	56.86	1.23	75.78	5.14	0.919
C1*s* - C=O	288.7	286.91	282	19.5	1.23	25.99	1.76	0.919
Fe3*p*	52.35	49.84	46.94	20.47	1.86	41.01	1.95	1.221
K2*p*1/2	299.3	296.39	291.7	25.96	1.78	50.09	2.29	1.367
K2*p*3/2	299.3	293.58	291.7	62.9	1.47	100.14	2.36	2.649
Mg2*s*	92	88.6	85.31	30.76	2.11	70.2	7.74	0.532
O1*s*	535.8	532.04	528.2	477.26	2.46	1267.14	35.54	2.449
Si2*p*1/2	105.3	103.19	100.1	34.5	1.28	47.91	10.26	0.275
Si2*p*3/2	105.3	102.19	100.1	65.58	1.35	95.83	10.46	0.539
Si2*s*	157.2	153.57	149.8	49.71	2.65	142.09	8.72	0.974

BU1_17, zone A, spot 200μm

Name	Start BE	Peak BE	End BE	Height [CPS]	FWHM [eV]	Area [CPS·eV]	At.%	SF
K2p3/2	298.4	293.49	290.9	367.37	1.37	544.83	1.66	2.649
K2p1/2	298.4	296.25	290.9	176.52	1.36	259.65	1.53	1.367
Ti2p3/2	468.85	459.05	454.77	120.01	1.89	241.66	0.53	3.936
Ti2p1/2	468.85	464.68	454.77	43.23	3.39	156.06	0.66	2.033
Si2p3/2	106.3	102.65	98.6	319.06	1.68	580.42	8.16	0.539
Si2p1/2	106.3	101.99	98.6	177.9	1.45	278.6	7.68	0.275
O1s	537.4	531.95	527.5	3337.52	2.4	8688.17	31.36	2.449
Fe2p3/2	731.6	710.16	705.18	102.78	3.66	488.52	0.51	9.218
Fe2p1/2	731.6	723.57	705.18	36.44	3.3	161.48	0.33	4.755
C1s - C-H	290.96	284.81	280.2	1500.65	1.65	2685.44	23.44	0.919
C1s - C-O	290.96	286.64	280.2	240.38	1.65	430.16	3.76	0.919
C1s - C=O	290.96	289.15	280.2	92.18	1.65	164.96	1.44	0.919
Si2s	158.5	153.5	148.69	310.3	2.57	863.37	6.82	0.974
Na1s	1075.1	1072.34	1069.4	73.81	2	159.49	0.32	6.631
Al2p3/2	76.6	72.56	67	75.07	1.34	108.55	2.68	0.306
Al2p1/2	76.6	73.36	67	47.46	1.02	52.11	2.56	0.153
Fe3p	51.84	48.85	45.58	146.95	1.48	235	1.44	1.221
Mg2s	95.32	88.88	85	175.06	1.91	361.76	5.13	0.532

BU1_17, zone B, spot 200μm

Name	Start BE	Peak BE	End BE	Height [CPS]	FWHM [eV]	Area [CPS·eV]	At.%	SF
C1s - C-H	290.4	284.84	281.5	1092.19	1.4	1658.24	14.18	0.919
C1s - C-O	290.4	285.92	281.5	310.2	1.4	470.96	4.03	0.919
C1s - C=O	290.4	287.24	281.5	69.51	1.4	105.54	0.9	0.919
Si2s	159.9	153.71	145.9	401.07	2.74	1190.38	9.21	0.974
Fe2p3/2	735.2	710.45	703.7	139.61	4.46	843.32	0.87	9.218
Fe2p1/2	735.2	724.08	703.7	65.28	4.63	404.74	0.82	4.755
O1s	535.9	532.11	527.9	3801.7	2.31	9502.77	33.6	2.449
Si2p3/2	105.7	102.45	99.5	451.08	1.5	731.26	10.07	0.539
Si2p1/2	105.7	103.17	99.5	205.13	1.58	351	9.47	0.275
Ti2p3/2	468.56	459.37	454.75	143.2	1.87	289.57	0.62	3.936
Ti2p1/2	468.56	465.11	454.75	46.16	2.81	140.77	0.58	2.033
K2p3/2	298.4	293.7	291.2	394.65	1.42	607.25	1.81	2.649
K2p1/2	298.4	296.54	291.2	238.87	1.21	312.65	1.8	1.367
Mg2s	93	88.88	83	236.61	2	510.49	7.1	0.532
Fe3p	53.18	50.15	46.66	170.37	1.64	301.89	1.81	1.221
Al2p3/2	78.4	73.87	69.2	107.43	1.14	131.9	2.12	0.458
Al2p1/2	78.4	74.83	69.2	62.28	0.95	63.31	1.02	0.458

8. REFERENCES

Alvarez-Silva M., Uribe-Salas A., Mirnezami M. and Finch J. A. (2010) The point of zero charge of phyllosilicate minerals using the Mular–Roberts titration technique. *Minerals Engineering* **23**, 383.

Avouris P., Hertel T. and Martel R. (1997) Atomic force microscope tip-induced local oxidation of silicon: kinetics, mechanisms, and nanofabrications. *Applied Physics Letters* **71**, 285.

Bailey S.W. (1988) *Chlorites: structures and crystal chemistry*. In *Hydrous Phyllosilicates (exclusive of micas)*, S.W. Bailey Ed.. Reviews in Mineralogy, vol. 19, p. 347 Mineralogical Society of America, Washington, D.C., U.S.A..

Baumann M. and Stark R. W. (2010) Dual frequency atomic force microscopy on charged surfaces. *Ultramicroscopy* **110**, 578.

Bayliss P. (1975) Nomenclature of the trioctahedral chlorites. *The Canadian Mineralogist* **13**, 178.

Bergaya F., Theng B. K. G. and Lagaly G. Eds. (2006) *Handbook of Clay Science*, 1st edition, Elsavier, Amsterdam, The Netherlands.

Brigatti M. F. and Guggenheim S. (2002) *Mica crystal chemistry and the influence of pressure, temperature, and solid solution on atomistic models*. In *Micas: Crystal Chemistry and Metamorphic Petrology*, Mottana A., Sassi F. P., Thompson J. B. and Guggenheim S. Eds.. Reviews in Mineralogy and Geo-chemistry, vol. 46, p. 1, Mineralogical Society of America, Washington, D.C., U.S.A..

Chien F. S.-S., Chou Y. C., Chen T. T., Hsieh W.-F., Chao T.-S., Gwo S. (2001) Nano-oxidation of silicon nitride films with an atomic force microscope: chemical mapping, kinetics, and applications. *Journal of Applied Physics* **89**, 2465.

Chi P. Y., Lin H. Y., Liu, C. H. and Chen C. D. (2006) Generation of nano-scaled DNA patterns through electro-beam induced charge trapping. *Nanotechnology* **17**, 1.

Comodi P., Fumagalli P., Montagnoli M. and Zanazzi P. F. (2004) A single-crystal study on the pressure behaviour of phlogopite and petrological implications. *American Mineralogist* **89**, 647.

Cooper J. B., Abdelkader M. and Wise K. L. (2013) Sequentially Shifted Excitation Raman Spectroscopy: Novel Algorithm and Instrumentation for Fluorescence-Free Raman Spectroscopy in Spectral Space. *Applied Spectroscopy* **67**, 973.

Deer W. A., Howie R. A. and Zussman J. (2013) An introduction to the rock-forming minerals, 3rd ed., The Mineralogical Society, London, UK.

Demange M. (2012) *Systematic mineralogy*. In *Mineralogy for Petrologists: optics, chemistry and occurrence of rock-forming minerals*, chap. 3, CRC Press, Taylor & Francis Group, London, UK.

de Caritat P., Hutcheon I. and Walshe J. L. (1993) Chlorite geothermometry: a review. *Clays and Clay Minerals* **41**, 219.

Dinelli F., Menozzi C., Baschieri P., Facci P. and Pingue P. (2010) Scanning probe nanoimprinting lithography. *Nanotechnology* **21**, 75305.

Downs R. T. (2006) The RRUFF Project: an integrated study of the chemistry, crystallography, Raman and infrared spectroscopy of minerals. Program and Abstracts of the *19th General Meeting of the International Mineralogical Association* in Kobe, Japan. O03-13.

Erdmann M., David R., Fornof A. and Gaub H. E. (2010) Electrically controlled DNA adhesion. *Nature Nanotechnology* **2010**, 154.

Elings V. B. and Gurley J. A. (1994) Scanning probe microscope using stored data for vertical probe positioning. U.S. Patent 5,308,974, May 3.

Evans B. W. and Guggenheim S. (1998) *Talc, pyrophyllite, and related minerals*. In *Hydrous Phyllosilicates (Exclusive of micas)*, Bailey S. W. Ed.. Reviews in Mineralogy, vol. 19, p. 225, Mineralogical Society of America, Washington, D.C., U.S.A..

Evans S. and Hiorns A.G. (1996) Angle-resolved X-ray photoelectron studies of cleavage in chlorites. *Clays and Clay Minerals* **44**, 398.

Fadley C. S. (2010) X-ray photoelectron spectroscopy: Progress and perspectives. *Journal of Electron Spectroscopy and Related Phenomena* **178–179**, 2.

Farkas N., Zhang G., Evans E. A., Ramsier R. D. and Dagata J. A. (2003) Nanoscale oxidation of zirconium surface: kinetics and mechanisms. *Journal of Vacuum Science and Technology A* **21**, 1188.

Fleet M. E. Ed. (2003) *Rock-forming Minerals: Micas*, vol. 3A, 2nd edition. The Geological Society Publishing House, Bath, UK.

Fenwick O., Bozec L., Credgington D., Hammiche A., Lazzerini G. M., Silberberg Y. R. and Cacialli F. (2009) Thermochemical nanopatterning of organic semiconductors. *Nature Nanotechnology* **4**, 664.

Fornasiero D. and Ralston J. (2005) Cu(II) and Ni(II) activation in the flotation of quartz, lizardite and chlorite. *International Journal of Mineral Processing* **76**, 75.

Frentrup H. and Allen M. S. (2011) Error in dynamic spring constant calibration of atomic force microscope probes due to nonuniform cantilevers. *Nanotechnology* **22**, 295703.

Friedbacher G. and Fuchs H. (1999) Classification of scanning probe microscopies. *Pure and Applied Chemistry* **71**, 1337.

Fuerstenau D. W. and Pradip (2005) Zeta potentials in the flotation of oxide and silicate minerals. *Advances in Colloid and Interface Science* **114–115**, 9.

Fukuma T. (2009) Subnanometer-resolution frequency modulation atomic force microscopy in liquid for biological applications. *Japanese Journal of Applied Physics* **48**, 08JA01.

Garcia R., Martinez R. V. and Martinez J. (2006) Nano-chemistry and scanning probe nanolithographies. *Chemical Society Reviews* **35**, 29.

Gates R. S., Reitsma M. G., Kramar J. A. and Pratt J. R. (2011) Atomic Force Microscope Cantilever Flexural Stiffness Calibration: Toward a Standard Traceable Method. *Journal of Research of the National Institute of Standards and Technology* **116**, 703.

Giessibl F. J. (2003) Advances in atomic force microscopy. *Reviews of Modern Physics* **75**, 494.

Giessibl F. J., Hembacher S., Bielefeldt H. and Mannhart J. (2000) Subatomic features on the silicon (111)-(737) surface observed by atomic force microscopy. *Science* **289**, 422.

Girard P. (2001) Electrostatic force microscopy: principles and some applications to semiconductors. *Nanotechnology* **12**, 485.

Giro A., Bergia A., Zuccheri G., Bink H. H. J., Pleij C. W. A. and Samorì B. (2004) Single molecule studies of RNA secondary structure: AFM of TYMV viral RNA. *Microscopy Research and Technique* **65**, 235.

Gozen B. A. and Ozdoganlar O. B. (2010) A rotating-tip-based mechanical nano-manufacturing process: nanomilling. *Nanoscale Research Letters* **5**, 1403.

Guggenheim S., Adams J. M., Bain D. C., Bergaya F., Brigatti M. F., Drits V. A., Formoso M. L. L., Galan E., Kogure T. and Stanjek H. (2006) Summary of recommendations of nomenclature committees relevant to clay mineralogy: report of the association internationale pour l'etude des argiles (aipea) nomenclature committee for 2006. *Clays and Clay Minerals* **54**, 761.

Hanczyc M. M., Mansy S. S. and Szostak J. W. (2006) Mineral surface directed membrane assembly. *Origins of Life and Evolution of the Biosphere* **37**, 67.

Hazen R. M. and Finger L. W. (1978) The crystal structures and compressibilities of layer minerals at high pressure. II. Phlogopite and chlorite. *American Mineralogist* **63**, 293.

Hazen R. M. (2006) Mineral surfaces and the prebiotic selection and organization of biomolecules. *American Mineralogist* **91**, 1715.

Hazen R. M., Papineau D., Bleeker W., Downs R. T., Ferry J. M., McCoy T. J., Sverjensky D. A. and Yang H. (2008) Mineral evolution. *American Mineralogist* **93**, 1693.

Hermosilla I. (2012) Raman spectra processing algorithms and database for RLS-ExoMars, Abstracts of the *European Planetary Science Congress* 2012, vol. 7.

Hnilova M., Khatayevich D., Carlson A., Oren E. E., Gresswell C., Zheng S., Ohuchi F., Sarikaya M. and Tamerler C. (2012) Single-step fabrication of patterned gold film array by an engineered multi-functional peptide. *Journal of Colloid and Interface Science* **365**, 97.

Hufner S. Ed. (2003) *Photoelectron spectroscopy: principles and applications*. Springer-Verlag Berlin Heidelberg.

Huo F., Zheng G., Liao X., Giam L. R., Chai J., Chen X., Shim W. and Mirkin C. A. (2010) Beam pen lithography. *Nature Nanotechnology* **5**, 637.

Kendall T. A., Na C., Jun Y. S. and Martin S. T. (2008) Electrical properties of mineral surfaces for increasing water sorption. *Langmuir* **24**, 2519.

Kershner R. J., Bozano L. D., Micheel C. M., Hung A. M., Fornof A. R., Cha J. N., Rettner C. T., Bersani M., Frommer J., Rothemund P. W. K. and Wallraff G. M. (2009) Placement and orientation of individual DNA shapes on lithographically patterned surfaces. *Nature Nanotechnology* **4**, 557.

Kim H. J., Roh Y. and Hong B. (2010) Selective Formation of a Latticed Nanostructure with the Precise Alignment of DNA-Templated Gold Nanowires. *Langmuir* **2010**, 18315.

Kodama H. (2011) *Phyllosilicates*. In *Handbook of Soil Science: Properties and Processes*, 2nd edition, Huang P. M., Li Y. and Sumner M. E. Eds., CRC Press.

Krauss K. (1974) Potassium-barium exchange in phlogopite. *Canadian Mineralogist* **12**, 394.

Kwon K. D., Vadillo-Rodriguez V., Logan B.E. and Kubicki J.D. (2006) Interactions of biopolymers with silica surfaces: Force measurements and electronic structure calculation studies. *Geochimica et Cosmo-chimica Acta* **70**, 3803.

Inoue S., Chu S.-Z., Wada K., Li D. and Haneda H. (2003) New roots to the formation of nanostructures on glass surface through anodic oxidation of sputtered aluminium. *Science and Technology of Advanced Materials* **4**, 269.

Inoue A., Meunier A., Patrier-Mas P., Rigault C., Beaufort D. and Vieillard P. (2009) Application of chemical geothermometry to low-temperature trioctahedral chlorites. *Clays and Clay Minerals* **57**, 371.

Lacalamita M., Mesto E., Scordari F. and Schingaro E. (2012) Chemical and structural study of 1M- and 2M$_1$-phlogopites coexisting in the same Kasenyi kamafugitic rock (SW Uganda). *Physics and Chemistry of Minerals* **39**, 601.

Laird J. (1988) *Chlorites: Metamorphic petrology*. In *Hydrous Phyllosilicates (Exclusive of micas)*, Bailey S. W. Ed.. Reviews in Mineralogy, vol. 19, p. 405, Mineralogical Society of America, Washington, D.C., U.S.A..

Laetsch T. and Downs R. (2006) Software for identification and refinement of cell parameters from powder diffraction data of minerals using the RRUFF project and american mineralogist crystal structure databases. Abstracts from the *19th General Meeting of the International Mineralogical Association*, Kobe, Japan, 23-28 July 2006.

Lee M. and Jhe W. (2006) General theory of amplitude-modulation atomic force microscopy. *Physical Review Letters* **97**, 036104.

Lemeshko S. L., Gavrilov S., Shevyakov V., Roschin V. and Solomatenko R. (2001) Investigation of tip-induced ultrathin Ti film oxidation kinetics. *Nanotechnology* **12**, 273.

Lewis I. R. and Edwards H. Eds. (2001) *Handbook of Raman spectroscopy: from the research laboratory to the process line*. Maecel Dekker Inc, NY, USA.

Lin H. Y., Tsai L. C., Chi P. Y. and Chen C. D. (2005) Positioning of extended individual DNA molecules on electrodes by non-uniform AC electric fields. *Nanotechnology* **16**, 2738.

Lin H. Y., Tsai L. C. and Chen C. D. (2007) Assembly of nanoparticle patterns with single-particle resolution using DNA-mediated charge trapping technique: method and applications. *Advanced Functional Materials* **17**, 3182.

Lindgren I. (2004) Chemical shifts in X-ray and photo-electron spectroscopy: a historical review. *Journal of Electron Spectroscopy and Related Phenomena* **137–140**, 59.

Lyuksyutov S. F., Vaia R. A., Paramonov P. B., Juhl S., Waterhouse L., Ralich R. M., Sigalov G. and Sancaktar E. (2003) Electrostatic nanolithography in polymers using atomic force microscopy. *Nature Materials* **2**, 468.

112

McKeown D. A., Bell M. I. and Etz E. S. (1999) Raman spectra and vibrational analysis of the trioctahedral mica phlogopite. *American Mineralogist* **84**, 970.

Megouda N., Piret G., Galopin E., Coffinier Y., Hadjersi T., Elkechai O. and Boukherroub R. (2012) Lithographically patterned silicon nanostructures on silicon substrates. *Applied Surface Science* **258**, 6007.

Mendes P. M., Yeung C. L. and Preece J. A. (2007) Bio-nanopatterning of surfaces. *Nanoscale Research Letters* **2**, 373.

Mironov V. L. Ed. (2004) *Fundamentals of scanning probe microscopy*. The Russian Academy of Sciences, Nizhniy Novgorod, Russia.

Montes S., Atenas G. M. and Valero E. (2007) How fine particles on haematite mineral ultimately define the mineral surface charge and the overall floatability behaviour. *Journal of the South African Institute of Mining and Metallurgy* **107**, 689.

Nanonis operation manual for oscillator controller 4, Nanonis GmbH, Zurich, pp. 52-54, 2010 (see also http://www.specs-zurich.com/upload/cms/user/AN-Lille-Kelvin.pdf)

Nyffenegger R. M., Penner R. M. and Schierle R. (1997) Electrostatic force microscopy of silver nanocrystals with nanometer-scale resolution. *Applied Physics Letters* **71**, 1878.

Nonnenmacher M., O'Boyle M. P. and Wickramasinghe H. K. (1991) Kelvin probe force microscopy. *Applied Physics Letters* **58**, 2921.

Ogaki R., Alexander M. and Kingshott P. (2010) Chemical patterning in biointerface science. *Materials Today* **13**, 22.

Onuki T., Tokizaki T., Watanabe Y., Tsuchiya T. and Tani T. (2002) Nanometer-sized optical waveguides fabricated by anodic oxidation using a scanning near-field optical microscope. *Applied Physics Letters* **80**, 4629.

Pavese A., Levy D., Curetti N., Diella V., Fumagalli P. and Sani A. (2003) Equation of state and compressibility of phlogopite by in-situ high-pressure X-ray powder diffraction. *European Journal of Mineralogy* **5**, 455.

Pires D., Hedrick J. L., Silva A. D., Frommer J., Gotsmann B., Wolf H., Despont M., Duerig U. and Knoll A. W. (2010) Nanoscale three-dimensional patterning of molecular resists by scanning probes. *Science* **328**, 732.

Poggi M. A., Gadsby E. D. and Bottomley L. A. (2004) Scanning probe microscopy. *Analytical Chemistry* **76**, 3429.

Poli S. and Schmidt M. W. (2002) Petrology of subducted slabs. *Annual Review of Earth and Planetary Sciences* **30**, 207-235.

Ramsier R. D., Ralich R. M. and Lyuksyutov S. F. (2001) Nanolithography of silicon: an approach for investigating tip-surface interactions during writing. *Applied Physics Letters* **79**, 2820.

Rosa L. G. and Liang J (2009) Atomic force microscope nanolithography: dip-pen, nanoshaving, nanografting, tapping mode, electrochemical and thermal nanolithography. *Journal of Physics: Condensed Matter* **21**, 483001.

Russell R. L. and Guggenheim S. (1999) Crystal structures of near end-member phlogopite at high temperature and heat treated Fe-rich phlogopite: the influence of the O,OH,F site. *The Canadian Mineralogist* **37**, 711.

Saavedra H. M., Mullen T. J., Zhang P., Dewey D. C., Claridge S. A. and Weiss P. S. (2010) Hybrid strategies in nanolithography. *Reports on Progress in Physics* **73**, 03650.

Sader J. E., Chon J. W. M. and Mulvaney P. (1999) Calibration of rectangular atomic force microscope cantilevers. *Review of Scientific Instruments* **70**, 3967.

Sader J. E., Sanelli J. A., Adamson B. D., Monty J. P., Wei X., Crawford S. A., Friend J. R., Marusic I., Mulvaney P. and Bieske E. J. (2012) Spring constant calibration of atomic force microscope cantilevers of arbitrary shape. *Review of Scientific Instruments* **83**, 103705.

Saint Jean M., Hudlet S., Guthmann C. and Berger J. (1999) Van der Waals and capacitive forces in atomic force microscopies. *Journal of Applied Physics* **86**, 5245.

Sánchez-Pastor N., Aldushin K., Jordan G. and Schmahl W. W. (2010) K^+–Na^+ exchange in phlogopite on the scale of a single layer. *Geochimica et Cosmochimica Acta* **74**, 1954.

Sauer J. (1989) Molecular models in *ab initio* studies of solids and surfaces: from ionic crystals and semiconductors to catalysts. *Chemical Reviews* **89**, 199.

Schingaro E., Lacalamita M., Scordari F. and Mesto E. (2013) 3*T*-phlogopite from Kasenyi kamafugite (SW Uganda): EPMA, XPS, FTIR, and SCXRD study. *American Mineralogist* **98**, 709.

Seyama H. and Soma M. (1985) Bonding-state characterization of the constituent elements of silicate minerals by X-ray photoelectron spectroscopy. *Journal of the Chemical Society, Faraday Transactions* **1**, 485.

Seyama H. and Soma M. (1987) Fe 2*p* spectra of silicate minerals. *Journal of Electron Spectroscopy and Related Phenomena* **42**, 97.

Seyama H. and Soma M. (1988) Application of X-ray Photoelectron spectroscopy to the study of silicate minerals. Research Report from the National Institute for Environmental Studies, Japan, No. 111.

Seyama H., Soma M. and Theng B. K. G. (2006) *X-ray photoelectron spectroscopy*. In *Handbook of Clay Science*, 1st edition, Bergaya F., Theng B. K. G. and Lagaly G. Eds., Elsavier, Amsterdam, The Netherlands.

Shirley D. A. (1972) Effect of atomic and extra-atomic relaxation on atomic binding energies. *Chemical Physics Letters* **16**, 220.

Siegbahn K. (1981) Electron spectroscopy for atoms, molecules and condensed matter. Nobel lecture.

Šontevska V., Jovanovski G., Makreski P., Raškovska A. and Šoptrajanov B. (2008) Minerals from macedonia. XXI. Vibrational spectroscopy as identificational tool for some phyllosilicate minerals. *Acta Chimica Slovenica* **55**, 757.

Stark R. W., Naujoks N. and Stemmer A. (2007) Multifrequency electrostatic force microscopy in the repulsive regime. *Nanotechnology* **17**, 065502.

Sugimoto Y., Pou P., Abe M., Jelinek P., Perez R., Morita S. and Custance O. (2007) Chemical identification of individual surface atoms by atomic force microscopy. *Nature* **446**, 64.

Sugimura H., Ishida Y., Hayashi K., Takai O. and Nakagiri N. (2002) Potential shielding by the surface water layer in Kelvin probe force microscopy. *Applied Physics Letters* **80**, 1459.

Tang Q., Shi S. and Zhou L. (2006) Polymer nanostructures constructed via atomic force microscopy and their applications. In *Polymeric Nanostructures and Their Applications*, chap. 15, Nalwa H. S. Ed., American Scientific Publishers, Stevenson Ranch, CA, U.S.A..

Tlili A., Smith D. C., Beny J.-M. And Boyer H. (1989) A Raman microprobe study of natural micas. *Mineralogical Magazine* **53**, 165.

Tutti F., Dubrovinsky L. S. and Nygren M. (2000) High-temperature study and thermal expansion of phlogopite. *Physics and Chemistry of Minerals* **27**, 599.

Valdrè G. (2007) Natural nanoscale surface potential of clinochlore and its ability to align nucleotides and drive DNA conformational change. *European Journal of Mineralogy* **19**, 309.

Valdrè G. and Moro D. (2008a) 3D finite element analysis of electrostatic deflection of commercial and FIB-modified cantilevers for electric and Kelvin force microscopy: I. Triangular shaped cantilevers with symmetric pyramidal tips. *Nanotechnology* **19**, 405501.

Valdrè G. and Moro D. (2008b) 3D finite element analysis of electrostatic deflection and shielding of commercial and FIB-modified cantilevers for electric and Kelvin force microscopy: II. Rectangular shaped cantilevers with asymmetric pyramidal tips. *Nanotechnology* **19**, 405502.

Valdrè G., Malferrari D. and Brigatti M. F. (2009) Crystallographic features and cleavage nanomorphology of clinochlore: specific applications. *Clays and Clay Minerals* **57**, 183.

Valdrè G., Tosoni S. and Moro D. (2011) Zeolitic-type Brønsted-Lowry sites distribution imaged on clinochlore. *American Mineralogist* **96**, 1461.

Verbeek C. J. R. (2002) Highly filled polyethylene/phlogopite composites. *Materials Letters* **52**, 453.

Verschuuren M. A., Gerlach P., van Sprang H. A. and Polman A. (2012) Improved performance of polarization-stable VCSELs by monolithic sub-wavelength gratings produced by soft nano-imprint lithography. *Nanotechnology* **22**, 505201.

Xie X. N., Chung H. J., Sow C. H. and Wee A. T. S. (2006) Nanoscale materials patterning and engineering by atomic force microscopy nanolithography. *Materials Science and Engineering R* **54**, 1.

Yanina S. V. and Rosso K. M. (2008) Linked reactivity at mineral-water interfaces through bulk crystal conduction. *Science* **320**, 218.

Wang Y., Hong X., Zeng J., Liu B., Guo B. and Yan H. (2009) AFM tip hammering nanolithography. *Small* **5**, 477.

Wiewióra A. and Weiss Z. (1990) Crystallochemical classifications of phyllosilicates based on the unified system of projection of chemical composition: II. The chlorite group. *Clay Minerals* **25**, 83.

Zanazzi P. F., Montagnoli M., Nazzareni S. and Comodi P. (2006) Structural effects of pressure on triclinic chlorite: A single-crystal study. *American Mineralogist* **91**, 1871.

Zanazzi P. F., Montagnoli M, Nazzareni S. and Comodi P. (2007) Structural effects of pressure on monoclinic chlorite: A single-crystal study. *American Mineralogist* **92**, 655.

Zane A. and Weiss Z. (1996) A procedure for classifying rock-forming chlorites based on microprobe data. *Rendiconti Lincei* **9**, 51.

Zheng Z., Yang M. and Zhang B. (2008) Reversible nanopatterning on self-assembled monolayers on gold. *J. Physics and Chemistry C* **112**, 6597.

Ziegler D., Rychen J., Naujoks N. and Stemmer, A. (2007) Compensating electrostatic forces by single-scan Kelvin probe force microscopy. *Nanotechnology* **18**, 225505.